

COSMOGLOBE I. Improved Wilkinson Microwave Anisotropy Probe frequency maps through Bayesian end-to-end analysis

D. J. Watts^{1*} et al.

Institute of Theoretical Astrophysics, University of Oslo, Blindern, Oslo, Norway

February 21, 2023

ABSTRACT

We present the first joint analysis of *WMAP* and *Planck* LFI time-ordered data, processed within the Bayesian end-to-end COSMOGLOBE framework. This framework builds directly on a similar analysis of the LFI measurements by the BEYONDPLANCK collaboration, and approaches the CMB analysis challenge through Gibbs sampling of a global posterior distribution. The computational cost of producing one complete *WMAP*+LFI Gibbs sample is 581 CPU-hr, including calibration, map-making, and component separation, of which 389 CPU-hr is spent on *WMAP* low-level processing; this demonstrates that end-to-end Bayesian analysis of the *WMAP* We find that our *WMAP* posterior mean temperature sky maps are largely consistent with the official maps. The most notable differences are associated with the gain model; for example, our *K*-band calibration is on average 0.6% lower and it exhibits weaker bi-annual variations. Our polarization maps exhibits significantly weaker transmission imbalance residuals than the official maps, and it is particularly noteworthy that our *W*-band sky maps appear for the first time statistically consistent with the *V*-band maps. At a higher level, *WMAP*-minus-LFI frequency map differences appear for the first time visually consistent with white noise over most of the sky. However, although these new products clearly represent an important step forward in understanding both the *WMAP* and LFI measurements, we do identify three specific issues that require further work, namely 1) noise mismodelling at high temporal frequencies, 2) a quadrupolar *V*-band temperature residual at the 2 μK level; and 3) a strong degeneracy between the absolute *K*-band calibration and the dipole of the anomalous microwave emission component. Nevertheless, the reprocessed *WMAP* maps presented here are significantly cleaner in terms of systematic uncertainties than the official *WMAP* maps, and we believe that they should be preferable for most scientific analyses that require *WMAP* data. Both sky maps and the associated code are made publicly available through the COSMOGLOBE web page.

Key words. ISM: general – Cosmology: observations, polarization, cosmic microwave background, diffuse radiation – Galaxy: general

Contents

1	Introduction	2	5	Data	8
2	End-to-end Bayesian <i>WMAP</i> analysis	2	5.1	Publicly available <i>WMAP</i> products	8
2.1	Official <i>WMAP</i> pipeline	2	5.2	TOD pre-processing and data selection	8
2.2	Instrument model	3	5.3	Inspection of time-ordered <i>WMAP</i> data	8
2.3	Sky model	3	6	Markov chains and parameter correlations	12
2.4	Posterior distribution and Gibbs sampling	3	7	Low-level posterior distributions	13
2.5	Sampling algorithms	4	7.1	Gain and baselines	13
2.5.1	Differential mapmaking	4	7.2	Transmission imbalance	13
2.5.2	Gain estimation	4	7.3	Instrumental noise and goodness-of-fit	13
2.5.3	Transmission imbalance estimation	4	8	High-level posterior distributions	17
2.5.4	Baseline sampling	5	8.1	Astrophysical sky model	17
3	Data	5	8.2	Frequency maps	18
3.1	Time-ordered data	5	8.3	Comparison with 9-year <i>WMAP</i> maps	30
3.2	Survey of fixed <i>WMAP</i> data products	5	8.4	Consistency within <i>WMAP</i> channels	30
4	Data selection, Markov chains and resources	5	8.5	Consistency between <i>WMAP</i> and LFI	30
4.1	Data selection	5	8.6	Preliminary CMB results	30
4.2	Trace plots	5	8.6.1	CMB Solar dipole	30
4.3	Parameter correlations	6	8.6.2	Temperature power spectrum	30
4.3.1	<i>K</i> -band calibration and AME	6	8.6.3	Preliminary large-scale CMB polarization results	30
4.4	Computational resources	6	8.7	Signal-to-noise ratio comparison between <i>WMAP</i> and LFI	30

* Corresponding author: D. J. Watts; duncanwa@astro.uio.no

9 Systematic error corrections and uncertainties	34
9.1 Sky map corrections	34
9.2 Power spectrum residuals	34
10 Outstanding issues	36
10.1 Noise modelling	36
10.2 V -band quadrupole residual	36
10.3 Degeneracy between K -band calibration and AME dipole	36
10.4 Other minor effects	36
10.4.1 Time-variable bandpass modelling	36
10.4.2 Polarized sidelobe modelling	36
11 Conclusions	36
A Survey of instrumental parameters	38
A.1 Gain, baselines, noise and χ^2	38
A.2 Transmission imbalance	38
B WMAP frequency map survey	38
C Comparison with BEYONDPLANCK LFI results	38

1. Introduction

The discovery of the Cosmic Microwave Background (CMB) by Penzias & Wilson (1965) marked a genuine paradigm shift in the field of cosmology, giving direct evidence that the Universe was once much hotter than it is today, effectively ruling out the steady-state theory of the universe (Dicke et al. 1965). Aside from a fundamental shift in the astrophysical history of the universe, this discovery spurred a series of cosmological experiments, which culminated in the Nobel Prize-winning measurements by COBE’s FIRAS and DMR experiments that confirmed the blackbody nature of the CMB and measured temperature variations from the primordial gravitational field (Smoot et al. 1992; Mather et al. 1994).

The Wilkinson Microwave Anisotropy Probe (WMAP) mission directly superseded the DMR, with the goal of making maps of the CMB that were 45 times more sensitive and 33 times higher angular resolution, all with the goal of measuring the physics of the universe at recombination (Bennett et al. 2003a). It can be argued that WMAP’s measurements of the CMB heralded a paradigm shift of similar magnitude to the 1965 discovery of the CMB. As quantified in Bennett et al. (2013), the volume of parameter space in standard Λ CDM allowed before WMAP was 68,000 times larger than after, with 99.9985 % of six-parameter Λ CDM ruled out. As a concrete example, the best determination of the age of the CMB before WMAP came from Boomerang (Lange et al. 2001) and constrained $t_0 < 14$ Gyr, with peak values of 9–11 Gyr, in contradiction with direct measurements of the oldest globular clusters (Hu et al. 2001).

The *Planck* satellite was developed concurrently with WMAP, and their operation lifetimes briefly overlapped, with *Planck* observing from 2009–2013 and WMAP from 2001–2011 (cite). *Planck*’s stated goal was to (check overview papers) fully characterize the temperature fluctuations from recombination, as well as to characterize the polarized microwave sky on large angular scales. Overall, the *Planck* experiment’s sensitivity to the CMB was an improvement in white noise sensitivity of a factor x, and a factor of y improvement in angular resolution. Overall, the raw sensitivity of *Planck* was an order of magnitude lower than WMAP. As opposed to WMAP, which used minimal COBE data in its fiducial analysis, *Planck*’s initial release calibrated off

of WMAP’s Solar dipole solution, and the Galactic component separation solution found in Planck Collaboration X (2016) by Commander (Jewell et al. 2004; Eriksen et al. 2004, 2006, 2008) made use of WMAP frequency maps. Most crucially, the *Planck* and WMAP maps are of similar quality that meaningful comparisons can be made between them. This last aspect has been critical, especially for the *Planck* Low Frequency Instrument (LFI), whose channels lie between those of WMAP.

As became clear in the LFI analysis (2018 LFI analysis), there was a circular dependency between the instrument calibration and the sky – a robust sky model made from *Planck* LFI maps was required to calibrate the timestreams sufficiently accurately. It was from this need that the BEYONDPLANCK project grew (BeyondPlanck 2022), powered by Commander3 (Galloway et al. 2022), a Gibbs sampling software that performed high-level and low-level parameter estimation in a single integrated framework. This analysis demonstrated the feasibility of a full end-to-end Gibbs sampling analysis in the CMB framework, while providing the highest-quality LFI maps to date.

The success of this paradigm, using properly characterized external datasets to improve TOD processing, led to the COSMOGLOBE initiative. As part of the BEYONDPLANCK suite of papers, Watts et al. (2022) integrated WMAP Q -band TODs into the Commander3 framework, calibrated off of the BEYONDPLANCK sky model. Beyond demonstrating that Commander3 can be applied to non-*Planck* data, this analysis uncovered an instrumental effect not previously described in the literature, namely a spurious polarization signal induced by the coupling of the Solar dipole, sidelobes, and horn transmission imbalance.

This paper is the next logical step in the set of previous developments, and presents the first end-to-end TOD analysis of multiple datasets. In this work, we analyze the full WMAP dataset at the raw TOD level alongside the *Planck* LFI TODs. As described in Sect. 2, this takes into account the fact that *Planck* and WMAP observed the same sky, and hence uses the sky as determined from a component separation using these data as a given in each stage of the Gibbs chain. We describe the underlying data in more detail in Sect. 5, and follow this by detailing the statistical properties of the output Markov chains in Sect. 4. We describe the posterior distribution of instrumental parameters in Sect. 7, and describe the properties of the derived frequency maps in Sect. 8. In Sect. ??, we compare the COSMOGLOBE results with the fiducial WMAP9 analysis in both map and power spectrum space, and Sect. 9 includes a thorough discussion of systematic error treatment in both frameworks. We conclude in Sect. 11, and lay a path forward for the COSMOGLOBE project.

2. End-to-end Bayesian WMAP analysis

We begin by discussing the WMAP analysis from uncalibrated TOD to maps. Sect. 2.1 provides a brief overview of the official WMAP pipeline, and Sect. 2.2 constructs the data model that will be used in the end-to-end Gibbs sampling analysis.

2.1. Official WMAP pipeline

The WMAP satellite carried forty differential polarization-sensitive radiometers grouped as differencing assemblies (DAs), where one pair was sensitive to the difference in signal at one polarization orientation and the other pair sensitive to the orthogonal polarization. In total, the DAs were allocated as: 1 K (23 GHz), 1 Ka (30 GHz), 2 Q (40 GHz), 2 V (60 GHz), and 4 W (90 GHz).

(We assume that the pointing solution and beams are perfectly known.)

Here we describe the calibration procedure as reported in Hinshaw et al. (2009). The TOD are initially modelled as having constant gain and baseline for a 1–24 hour period, and are fit to the orbital dipole assuming T_0 from Mather et al. (1999) and a map made from a previous iteration of the mapmaking procedure. Once the gain and baseline solution has converged, the data are fit to a parametric form of the radiometer performance as a function of housekeeping data, given in Greason et al. (2012).

(Sidelobes, mapmaking. Also need to mention the pointing solution.)

As described in Jarosik et al. (2007), the frequency response of the radiometers forming a DA are slightly different, which causes a spurious signal to be leaked into the polarization maps. This effect is mitigated by assigning a spurious pseudo-Stokes parameter, S , and solving for it explicitly in the mapmaking procedure.

2.2. Instrument model

Write down data model; refer to WMAP and BP papers extensively

In the COSMOGLOBE paradigm, it is simplest to characterize the data's goodness-of-fit to a model,

$$\mathbf{d} = \text{GP}[\mathbf{B}^{\text{symm}} \mathbf{M} \mathbf{a} + \mathbf{B}^{4\pi} (\mathbf{s}^{\text{orb}} + \mathbf{s}^{\text{fsl}})] + \mathbf{s}^{\text{inst}} + \mathbf{n}^{\text{corr}} + \mathbf{n}^{\text{w}}, \quad (1)$$

where \mathbf{G} is the time-dependent gain in the form of the matrix $\text{diag}(g_t)$, \mathbf{P} is the $n_p \times n_t$ pointing matrix, \mathbf{B}^{symm} and $\mathbf{B}^{4\pi}$ are the symmetrized and full symmetric beam, respectively, \mathbf{M} is the mixing matrix between a given component c with spectral energy distribution $f_c(\nu/\nu_{0,c})$ and a detector j with bandpass $\tau_j(\nu)$, given by

$$\mathbf{M}_{cj} = \int d\nu \tau_j(\nu) f_c(\nu/\nu_{c,0}). \quad (2)$$

The maps \mathbf{a} are the component amplitudes, \mathbf{s}^{orb} is the orbital dipole induced by the motion of the telescope with respect to the Sun, and \mathbf{s}^{fsl} is the time-dependent far sidelobe signal. In the Commander3 (Galloway et al. 2022) implementation, \mathbf{n}^{corr} is a realization of the correlated noise component whose SED is parametrized by $P(f \mid \xi_n)$, where ξ_n generally includes f_{knee} , a slope α , and whose amplitude is fixed by the white noise σ_0 . This model is often augmented, as we will discuss in Sects. ?? and ???. Similarly, each experiment has particular signals that are specific to the instrument in question, e.g., the 1 Hz spike in *Planck* LFI or the large baseline in *WMAP*, which can be modeled by \mathbf{s}^{inst} .

2.3. Sky model

Following BeyondPlanck (2022), we assume that the sky can be modeled as a linear combination of CMB fluctuations, synchrotron, free-free emission, anomalous microwave emission, thermal dust, and radio point sources. The parametric sky model

we adopt is given in brightness temperature units as

$$s_{\text{RJ}} = (\mathbf{a}_{\text{CMB}} + \mathbf{a}_{\text{quad}}(\nu)) \frac{x^2 e^x}{(e^x - 1)^2} + \quad (3)$$

$$+ \mathbf{a}_s \left(\frac{\nu}{\nu_{0,s}} \right)^{\beta_s} + \quad (4)$$

$$+ \mathbf{a}_{\text{ff}} \left(\frac{\nu_{0,\text{ff}}}{\nu} \right)^2 \frac{g_{\text{ff}}(\nu; T_e)}{g_{\text{ff}}(\nu_{0,\text{ff}}; T_e)} + \quad (5)$$

$$+ \mathbf{a}_{\text{ame}} e^{\beta(\nu - \nu_{0,\text{ame}})} + \quad (6)$$

$$+ \mathbf{a}_d \left(\frac{\nu}{\nu_{0,d}} \right)^{\beta_d + 1} \frac{e^{h\nu_{0,d}/k_B T_d} - 1}{e^{h\nu/k_B T_d} - 1} + \quad (7)$$

$$+ U_{\text{mJy}} \sum_{j=1}^{N_{\text{src}}} \mathbf{a}_{j,\text{src}} \left(\frac{\nu}{\nu_{0,\text{src}}} \right)^{\alpha_{j,\text{src}} - 2}. \quad (8)$$

Note that the AME model we adopt is a pure exponential, rather than the SED template $s_0^{\text{sd}}(\nu)$ computed using SpDust2 (Ali-Haïmoud et al. 2009; Ali-Haïmoud 2010; Silsbee et al. 2011). The SpDust2 model was parameterized in BeyondPlanck (2022) by a peak frequency ν_p such that

$$s_{\text{RJ}}^{\text{sd}}(\nu) \propto \nu^{-2} s_0^{\text{sd}} \left(\nu \cdot \frac{30 \text{ GHz}}{\nu_p} \right). \quad (9)$$

In the *WMAP* and LFI frequency range, the exponential model and the SpDust2 are phenomenologically quite similar, despite their very different origins. As we describe in (...), the exponential model is a simple fit with β drawn from a prior value of -3.57 , and is a clear parametric form that is easy to interpret. (Compare with log-normal model...)

2.4. Posterior distribution and Gibbs sampling

As shown in BeyondPlanck (2022), this allows us to write down a total model for the data, $\mathbf{d} = s^{\text{tot}}(\omega) + \mathbf{n}^{\text{w}}$, where s^{tot} encompasses all of the terms in Eq. (1) except for the white noise term. Assuming that all instrumental effects have been modelled, the data should be Gaussian distributed with a mean of $s^{\text{tot}}(\omega)$ and variance σ_0^2 . Given this model, we can evaluate the likelihood for arbitrary chunks of time-ordered data in the context of the entire model, so that individual chunks of data with poor fits can be more easily identified. In general, the likelihood is written

$$P(\mathbf{d} \mid \omega) \propto \exp \left(-\frac{1}{2} \sum_t \frac{(d_t - s_t^{\text{tot}}(\omega))^2}{\sigma_0^2} \right). \quad (10)$$

If $\mathbf{d} \sim \mathcal{N}(s^{\text{tot}}, \sigma_0^2)$ is the correct model for the data, the argument of the exponent is proportional to a χ^2 -distribution with n_{TOD} degrees of freedom. In the limit of large n , a χ^2 distribution is well-approximated by a Gaussian with mean n and variance $2n$. Therefore we define and use the reduced- χ^2 statistic,

$$\chi^2 \equiv \frac{\sum_t ((d_t - s_t^{\text{tot}})^2 / \sigma_0^2 - n_{\text{TOD}})}{\sqrt{2n_{\text{TOD}}}}, \quad (11)$$

which is approximately drawn from the standard normal distribution $\mathcal{N}(0, 1)$.

The COSMOGLOBE Gibbs chain is given by

$$\mathbf{g} \leftarrow P(\mathbf{g} \mid \mathbf{d}, \xi_n, s^{\text{inst}}, \beta, \mathbf{a}, C_\ell, \theta) \quad (12)$$

$$\mathbf{n}_{\text{corr}} \leftarrow P(\mathbf{n}_{\text{corr}} \mid \mathbf{d}, \mathbf{g}, \xi_n, s^{\text{inst}}, \beta, \mathbf{a}, C_\ell, \theta) \quad (13)$$

$$\xi_n \leftarrow P(\xi_n \mid \mathbf{d}, \mathbf{g}, \mathbf{n}_{\text{corr}}, s^{\text{inst}}, \beta, \mathbf{a}, C_\ell, \theta) \quad (14)$$

$$s^{\text{inst}} \leftarrow P(s^{\text{inst}} \mid \mathbf{d}, \mathbf{g}, \mathbf{n}_{\text{corr}}, \xi_n, \beta, \mathbf{a}, C_\ell, \theta) \quad (15)$$

$$\beta \leftarrow P(\beta \mid \mathbf{d}, \mathbf{g}, \mathbf{n}_{\text{corr}}, \xi_n, s^{\text{inst}}, C_\ell, \theta) \quad (16)$$

$$\mathbf{a} \leftarrow P(\mathbf{a} \mid \mathbf{d}, \mathbf{g}, \mathbf{n}_{\text{corr}}, \xi_n, s^{\text{inst}}, \beta, C_\ell, \theta) \quad (17)$$

$$C_\ell \leftarrow P(C_\ell \mid \mathbf{d}, \mathbf{g}, \mathbf{n}_{\text{corr}}, \xi_n, s^{\text{inst}}, \beta, \mathbf{a}, \theta) \quad (18)$$

$$\theta \leftarrow P(\theta \mid \mathbf{d}, \mathbf{g}, \mathbf{n}_{\text{corr}}, \xi_n, s^{\text{inst}}, \beta, \mathbf{a}, C_\ell), \quad (19)$$

with each step requiring its own dedicated sampling algorithm, and in the case of BEYONDPLANCK, its own publication. The Commander3 pipeline is designed so that results of each Gibbs sample can be easily passed to each other, and that the internal calculations of each step do not directly depend on the inner workings of each other. Therefore, in order to add another data set to the Gibbs chain, one must implement Eqs. (12)–(15) for each instrument, as was done in BeyondPlanck (2022) and Basyyrov et al. (2022) for *Planck* LFI and in Watts et al. (2022) for *WMAP*, or simply pass processed maps with beam, mask, and noise information to Eqs. (16)–(19), as was done for the Haslam 408 MHz map (Haslam et al. 1982; Remazeilles et al. 2015) and the *Planck* 353 and 857 GHz maps.

Before we discuss the results of this Gibbs chain as applied to the *Planck* LFI and *WMAP* data, we summarize the TOD processing steps in Sects. ?? and ??.

2.5. Sampling algorithms

Each step of the Gibbs chain requires its own distribution to be sampled from. In Sects. ?? we review the sampling algorithms implemented in the BEYONDPLANCK suite of papers, while Sects. 2.5.1–2.5.4 provide an overview of the *WMAP*-specific processing steps.

Gain sampling (Eq. ??) is described in Ihle et al. (2022).

Correlated noise sampling and noise SED sampling is described in Gjerløw et al. (2022).

Component separation for intensity and polarization are described in Andersen et al. (2022) and Svalheim et al. (2022), respectively.

Power spectrum estimation is described in Basyyrov et al. (2022).

Cosmological parameter estimation is described in Colombo et al. (2022).

2.5.1. Differential mapmaking

After calibration and correction for instrumental effects, the TOD can be modeled as

$$\mathbf{d} = \mathbf{P}\mathbf{m} + \mathbf{n}^{\text{w}}, \quad (20)$$

where

$$\mathbf{m} = \mathbf{B}^{\text{symm}} \mathbf{M} \mathbf{a} \quad (21)$$

is the expected map for each detector after removing the orbital dipole, far sidelobe, baseline, and a realization of correlated noise. The differential pointing strategy can be represented

in matrix form as

$$\mathbf{P}_{tp} = (1 + x_{\text{im}})(\delta_{p' p_A^l} + \delta_{p' p_B^l} \cos 2\psi_A + \delta_{p' p_A^U} \sin 2\psi_A) \quad (22)$$

$$- (1 - x_{\text{im}})(\delta_{p' p_B^l} - \delta_{p' p_B^U} \cos 2\psi_B - \delta_{p' p_B^U} \sin 2\psi_B) \quad (23)$$

where p_A and p_B are the time-dependent pointings for each DA. The maximum likelihood map can in principle be solved using the usual mapmaking equation,

$$\mathbf{P}^T \mathbf{N}^{-1} \mathbf{P} \mathbf{m} = \mathbf{P}^T \mathbf{N}^{-1} \mathbf{d}. \quad (24)$$

For a single-horn experiment, i.e., *Planck* LFI, this reduces to a 3×3 matrix that can be inverted for each pixel independently. For the pointing matrix in Eq. (22), this is no longer possible, as there is inherently coupling between horns A and B in the timestreams. The $3N_{\text{pix}} \times 3N_{\text{pix}}$ matrix can be solved using an iterative algorithm, e.g., preconditioned conjugate gradients.

(???) identified an issue where a large difference in the sky temperature at pixel value at pixel A versus pixel B induced artifacts in the mapmaking procedure. We adopt the procedure first described in (???) where only the pixel in a bright region, defined by a small processing mask by (???), is accumulated, this modifying the mapmaking equation to

$$\mathbf{P}_{\text{am}}^T \mathbf{N}^{-1} \mathbf{P} \mathbf{m} = \mathbf{P}_{\text{am}}^T \mathbf{N}^{-1} \mathbf{d}. \quad (25)$$

This equation can be solved using the BiCG-STAB algorithm for a non-symmetric matrix \mathbf{A} where $\mathbf{A}\mathbf{x} = \mathbf{b}$. We apply a preconditioner \mathbf{M} by numerically inverting the same problem with $N_{\text{side}} = 16$ maps and applying a diagonal noise matrix. Numerically, we define convergence as when the residual $\mathbf{r} \equiv \mathbf{b} - \mathbf{Ax}$ satisfies $\mathbf{r}^T \mathbf{M}^{-1} \mathbf{r} / \mathbf{b}^T \mathbf{M}^{-1} \mathbf{b} < 10^{-10}$, which typically takes about 20 iterations for producing frequency maps.

2.5.2. Gain estimation

2.5.3. Transmission imbalance estimation

Transmission imbalance, i.e., the differential power transmission of the optics and waveguide components, can be parameterized as

$$d_{t,j} = g_{t,j}[(1 + x_{\text{im},j})s_{t,j}^{\text{tot,A}} - (1 - x_{\text{im},j})s_{t,j}^{\text{tot,B}}] + n_t. \quad (26)$$

This can be decomposed into a differential (d) and common-mode (c) signal such that

$$d_{t,j} = g_{t,j}[s_{t,j}^{\text{d}} + x_{\text{im},j}s_{t,j}^{\text{c}}] + n_t. \quad (27)$$

In this form, the imbalance parameters can be estimated by drawing Gaussian samples from the standard mean and standard deviation over the entire mission.

The *WMAP* procedure, described in Jarosik et al. (2003a), fit for common-mode and differential coefficients along with a cubic baseline over 10 precession periods at a time, corresponding to 10 hours of observation. The mean and uncertainty were then calculated by averaging and taking the standard deviation of these values. This approach has the benefit of allowing for the tracking of possible transmission imbalance variation throughout the mission. However, none of the *WMAP* suite of papers have indicated this, and it has not arisen in our analysis, so we model this as an effect whose value is constant throughout the mission.

2.5.4. Baseline sampling

The data model adopted in Hinshaw et al. (2003) can be written in raw digital units (du) as

$$d = \text{GPBM}a + n + b, \quad (28)$$

where \mathbf{b} is the instrumental baseline and \mathbf{n} is the total instrumental noise. As detailed in Ihle et al. (2022), Commander3 divides the noise into $\mathbf{n} = \mathbf{n}^w + \mathbf{n}^{corr}$, a white noise term and a correlated noise term. By definition, the white noise does not have any correlations between adjacent pixels, so that any pixel-pixel covariance should be fully described by realizations of the \mathbf{n}^{corr} timestamp.

Commander estimates the baseline using the full estimate of the current sky model, $\mathbf{r} = \mathbf{d} - \mathbf{gs}^{\text{tot}} = \mathbf{b} + \mathbf{n}$. Modeling $\mathbf{b} = b_0 + b_1\Delta t$, we solve for b_0 and b_1 using linear regression in each timestamp stream while masking out samples that lie within the processing mask. Strictly speaking, this is breaking the Gibbs chain, as we are not formally sampling b_0 and b_1 for each TOD chunk. In practice, baseline estimation uncertainty propagates to correlated noise realizations and PSD parameters, as discussed below.

The approach detailed in Hinshaw et al. (2003) and the Commander implementation differ mainly in the assumed stable timescale – the initial *WMAP* baseline is estimated over one hour timescales, whereas Commander assumes constant values through the entire timestream, 3–7 days depending on the band in question. As noted in Hinshaw et al. (2003), residual baseline variations manifest as correlated noise stripes in the final maps. *WMAP9* solves this using a time-domain filter, downweighting the data based off of the noise characterization. This approach is equivalent to the Commander3 procedure of removing a constrained realization of correlated noise from the timestream directly, based on the best-fit to the noise PSD.

3. Data

3.1. Time-ordered data

3.2. Survey of fixed WMAP data products

**Summarize everything we assume from the WMAP analysis:
Beams, bandpasses, pointing, etc.**

4. Data selection, Markov chains and resources

4.1. Data selection

The full nine-year *WMAP* archive spans from August 10, 2001 to August 10, 2010, with the raw uncalibrated data spanning 626 GB. A little over 1 % of the data were lost or rejected due to incomplete satellite telemetry, thermal disturbances, spacecraft anomalies, and station-keeping maneuvers, with an extra 0.1 % rejected due to planet flagging (Bennett et al. 2003b; Hinshaw et al. 2007, 2009; Bennett et al. 2013). The final results reported in Bennett et al. (2013) included roughly 98.4 % of the total data volume. A full accounting of all data cuts can be found in Table 1.8 of Greason et al. (2012). In total, we flag the same data indicated in the fiducial *WMAP* analysis, and use the same planet flags

As shown in Galloway et al. (2022), a large fraction of Commander3’s computational time is spent performing FFTs on individual scans. Rather than truncating datastreams to have lengths equal to “magic numbers” for which FFTW (Frigo & Johnson 2005) is fastest, as in Galloway et al. (2022), we split

Table 1. Flagging statistics

Band	Flagged (%)	Discarded (%)	Used (%)
K	1.72	0.87	97.4
Ka	1.64	0.88	97.5
$Q1$	1.84	0.84	96.5
$Q2$	1.62	0.81	97.6
$V1$	1.62	1.10	97.3
$V2$	1.61	1.01	97.4
$W1$	1.76	1.03	97.2
$W2$	1.60	0.81	97.6
$W3$	1.61	0.87	97.5
$W4$	1.60	0.81	97.6

the data into scans of length 2^N , where $N = 22$ for $K-Q$, $N = 23$ for $V-W$. This yields scans with lengths of 6.21 days for K - and Ka -band, 4.97 days for Q -band, 7.46 days for V -band, and 4.97 days for W -band. These datastream lengths are short enough to be processed quickly and distributed efficiently across multiple processors, while being long enough to properly characterize the noise properties of the timestreams, whose f_{knee} 's are on the order 1 mHz. Most importantly, FFTW performs fastest when the datastream is of length 2^N .

When rechunking the data, timestreams of length 2^N were interrupted by events logged in Table 1.8 of Greason et al. (2012). When we encountered these events, TOD segments that were interrupted by the event were appended to the previous TOD, in most cases creating TODs with lengths $> 2^N$. We found that events of length $< 2^N$ were too short to accurately estimate the noise PSD parameters. This criterion led us to discard these otherwise useful data. In addition, when $> 10\%$ of the TOD was flagged, the large number of gaps in the data made the constrained realizations unreliable, as well as biasing the noise PSD parameters. Together, these two effects led to $\simeq 1\%$ of the data to be discarded despite being of acceptable quality. We present the full statistics for our maps in Table 3. In total, the COSMOGLOBE maps use slightly less data than the WMAP9 official products, which had a total efficiency of $\simeq 98.4\%$ (Bennett et al. 2013). The total difference in data volume can be entirely accounted for by the cuts described in this paragraph.

4.2. Trace plots

djfksajf lasj fkfdas fklasaj lfjds1 kfkj jasd1kfj aslkfj klsad1jf lsdajf lkasd1 flksdj kflsajdk f djfksajf lasj fkfdas fklasaj lfjds1 kfkj jasd1kfj aslkfj klsad1jf lsdajf lkasd1 flksdj kflsajdk f djfksajf lasj fkfdas fklasaj lfjds1 kfkj jasd1kfj aslkfj klsad1jf lsdajf lkasd1 flksdj kflsajdk f djfksajf lasj fkfdas fklasaj lfjds1 kfkj jasd1kfj aslkfj klsad1jf lsdajf lkasd1 flksdj kflsajdk f

dfjksajf lasj fkfdjas fklsaj lfjds1 kfkj jasdkfj aslkfj klsad1f ls-
dajf lkasd1 flksdj kf1sajdk f jfk1sajf lasj fkfdjas fklsaj lfjds1 kfkj
jasdkfj aslkfj klsad1f lsdajf lkasd1 flksdj kf1sajdk f djfksajf lasj
fkfdjas fklsaj lfjds1 kfkj jasdkfj aslkfj klsad1f lsdajf lkasd1 flksdj
kf1sajdk f djfksajf lasj fkfdjas fklsaj lfjds1 kfkj jasdkfj aslkfj klsad1f
lsdajf lkasd1 flksdj kf1sajdk f jfk1sajf lasj fkfdjas fklsaj lfjds1 kfkj
iasdkfj aslkfj klsad1f lsdajf lkasd1 flksdj kf1sajdk f

djfkfksajf lasj fkjdksaj fklksaj lfjdsf kfkj jasdlkfj aslkfj klsadjf ls-dajf lkasdjf flksdj kfslsajdk f djfksajf lasj fkjdjas fklksaj lfjdsf kfkj jasdlkfj aslkfj klsadjf lsdajf lkasdjf flksdj kfslsajdk f jfksajf lasj fkjdjas fklksaj lfjdsf kfkj jasdlkfj aslkfj klsadjf lsdajf lkasdjf flksdj kfslsajdk f djfksajf lasj fkjdjas fklksaj lfjdsf kfkj jasdlkfj aslkfj klsadjf lsdajf lkasdi flksdj kfslsajdk f difksaif lasj fkjdjas fklksaj lfjdsf

kfkj jasdlkfj aslkfj klsadjf lsdajf lkasdj flksdj kflsajdk f jfksajf lasj fkfdjas fklsaj lfjdsf kfkj jasdlkfj aslkfj klsadjf lsdajf lkasdj flksdj kflsajdk f

djfksajf lasj fkfdjas fklsaj lfjdsf kfkj jasdlkfj aslkfj klsadjf lsdajf lkasdj flksdj kflsajdk f djfksajf lasj fkfdjas fklsaj lfjdsf kfkj jasdlkfj aslkfj klsadjf lsdajf lkasdj flksdj kflsajdk f jfksajf lasj fkfdjas fklsaj lfjdsf kfkj jasdlkfj aslkfj klsadjf lsdajf lkasdj flksdj kflsajdk f djfksajf lasj fkfdjas fklsaj lfjdsf kfkj jasdlkfj aslkfj klsadjf lsdajf lkasdj flksdj kflsajdk f djfksajf lasj fkfdjas fklsaj lfjdsf kfkj jasdlkfj aslkfj klsadjf lsdajf lkasdj flksdj kflsajdk f

4.3. Parameter correlations

djfksajf lasj fkfdjas fklsaj lfjdsf kfkj jasdlkfj aslkfj klsadjf lsdajf lkasdj flksdj kflsajdk f djfksajf lasj fkfdjas fklsaj lfjdsf kfkj jasdlkfj aslkfj klsadjf lsdajf lkasdj flksdj kflsajdk f djfksajf lasj fkfdjas fklsaj lfjdsf kfkj jasdlkfj aslkfj klsadjf lsdajf lkasdj flksdj kflsajdk f jfksajf lasj fkfdjas fklsaj lfjdsf kfkj jasdlkfj aslkfj klsadjf lsdajf lkasdj flksdj kflsajdk f djfksajf lasj fkfdjas fklsaj lfjdsf kfkj jasdlkfj aslkfj klsadjf lsdajf lkasdj flksdj kflsajdk f

djfksajf lasj fkfdjas fklsaj lfjdsf kfkj jasdlkfj aslkfj klsadjf lsdajf lkasdj flksdj kflsajdk f jfksajf lasj fkfdjas fklsaj lfjdsf kfkj jasdlkfj aslkfj klsadjf lsdajf lkasdj flksdj kflsajdk f djfksajf lasj fkfdjas fklsaj lfjdsf kfkj jasdlkfj aslkfj klsadjf lsdajf lkasdj flksdj kflsajdk f djfksajf lasj fkfdjas fklsaj lfjdsf kfkj jasdlkfj aslkfj klsadjf lsdajf lkasdj flksdj kflsajdk f djfksajf lasj fkfdjas fklsaj lfjdsf kfkj jasdlkfj aslkfj klsadjf lsdajf lkasdj flksdj kflsajdk f

djfksajf lasj fkfdjas fklsaj lfjdsf kfkj jasdlkfj aslkfj klsadjf lsdajf lkasdj flksdj kflsajdk f djfksajf lasj fkfdjas fklsaj lfjdsf kfkj jasdlkfj aslkfj klsadjf lsdajf lkasdj flksdj kflsajdk f djfksajf lasj fkfdjas fklsaj lfjdsf kfkj jasdlkfj aslkfj klsadjf lsdajf lkasdj flksdj kflsajdk f djfksajf lasj fkfdjas fklsaj lfjdsf kfkj jasdlkfj aslkfj klsadjf lsdajf lkasdj flksdj kflsajdk f djfksajf lasj fkfdjas fklsaj lfjdsf kfkj jasdlkfj aslkfj klsadjf lsdajf lkasdj flksdj kflsajdk f djfksajf lasj fkfdjas fklsaj lfjdsf kfkj jasdlkfj aslkfj klsadjf lsdajf lkasdj flksdj kflsajdk f djfksajf lasj fkfdjas fklsaj lfjdsf kfkj jasdlkfj aslkfj klsadjf lsdajf lkasdj flksdj kflsajdk f

djfksajf lasj fkfdjas fklsaj lfjdsf kfkj jasdlkfj aslkfj klsadjf lsdajf lkasdj flksdj kflsajdk f djfksajf lasj fkfdjas fklsaj lfjdsf kfkj jasdlkfj aslkfj klsadjf lsdajf lkasdj flksdj kflsajdk f djfksajf lasj fkfdjas fklsaj lfjdsf kfkj jasdlkfj aslkfj klsadjf lsdajf lkasdj flksdj kflsajdk f djfksajf lasj fkfdjas fklsaj lfjdsf kfkj jasdlkfj aslkfj klsadjf lsdajf lkasdj flksdj kflsajdk f djfksajf lasj fkfdjas fklsaj lfjdsf kfkj jasdlkfj aslkfj klsadjf lsdajf lkasdj flksdj kflsajdk f

4.3.1. K-band calibration and AME

In a preliminary **Commander3** run, we discovered an unbounded rise in the *K*-band absolute calibration, g_0 , and the dipole in the AME component of the sky. Because the AME is strongest among all bands at *K*-band, any increase in the *K*-band absolute calibration can easily be accounted for by changing the amplitude of the AME, while leaving goodness-of-fit tests such as relative- χ^2 and residual maps unaffected.

In order to break this degeneracy, it was necessary to impose a prior either on the AME itself or on the absolute calibration. The AME prior we explored followed the approach of [Andersen et al. \(2022\)](#), in which the prior mean was the *Planck* DR4 857 GHz map scaled by $3 \cdot 10^{-5}$, and the variance is given in angular scales by a parameter q . We found that a prior of $q = 10^{-2} \mu\text{K}^2$ was necessary to stabilize the gain, resulting in an AME map that was nearly identical to the *Planck* 857 GHz band. As this gave a result that was inconsistent with many previous results, we opted instead to sample the absolute calibration instead.

Any error in g_0 leads to a residual due to the large Solar dipole. In practice, we found that the typical variation of g_0 was 0.002, giving a relative error of $\sim 0.1\%$. This variation induces a $\sim 6 \mu\text{K}$ Solar dipole uncertainty, which is easily attributed to AME during component separation. In Figure 33, we demonstrate this effect on recovered AME maps using extreme g_0 values of 1.175 and 1.9. We find that AME maps consistent with those presented in [Bennett et al. \(2013\)](#) and [Planck Collaboration X \(2016\)](#) are recovered when g_0 is between 1.180 and 1.182. Based on this analysis, we sample g_0 from a Gaussian with mean 1.1815 and standard deviation 0.001.

[Bennett et al. \(2013\)](#) and [Planck Collaboration X \(2016\)](#) find AME peak frequencies 12.0–17.5 GHz and 17–23 GHz, respectively, both with low signal-to-noise at high Galactic latitude and with structure along the plane. The Q-U-I JOint Tenerife Experiment (QUIJOTE) has recently released maps of the sky with approximately 70 % sky coverage at frequencies 11, 13, 17, and 19 GHz ([Rubiño-Martín et al. 2023](#)). QUIJOTE is optimized for characterizing the polarized sky, and constraints from, e.g., [de la Hoz et al. \(2023\)](#), will be critical for future polarized synchrotron SED characterization and polarized AME limits. While in principle the AME SED can be constrained by a joint *WMAP/LFI/QUIJOTE* analysis, we consider this outside of the scope of the paper, which aims to evaluate the effect of jointly analyzing *WMAP* and *Planck LFI* at the TOD level. Future analysis will include the QUIJOTE data, and hopefully break the $g_{a,\text{ame}}$ degeneracy.

4.4. Computational resources

Table 2. Computational resources required for end-to-end COSMOGLOBE processing. All times correspond to CPU hours, and all data volumes are reported in GB. Reported times are averaged over more than 100 samples, and vary by $\lesssim 5\%$ from sample to sample. **Preliminary numbers, not all accurate**

ITEM	30	44	70	K	Ka	Q1	Q2	V1	V2	W1	W2	W3	W4	SUM
<i>Data volume</i>														
Compressed TOD volume	86	178	597	13	12	15	15	19	18	26	26	26	26	1 053
<i>Processing time (cost per run)</i>														
TOD initialization/IO time	1.8	2.5	9.3	0.3	0.3	0.4	0.4	0.4	0.4	0.5	0.5	0.5	0.5	17.8
Other initialization														13.4
Total initialization														31.2
<i>Gibbs sampling steps (cost per sample)</i>														
Huffman decompression	1.1	2.1	10.5	0.9	0.8	1.0	1.0	1.3	1.3	1.8	1.8	1.8	1.8	27.2
TOD projection (\mathbf{P} operation)	0.4	0.9	4.2	2.6	2.6	3.3	3.4	4.3	4.3	6.4	6.3	6.3	6.4	54.0
Sidelobe evaluation	1.0	2.1	7.6	2.9	2.9	3.5	3.5	4.7	4.8	7.0	6.9	6.9	6.9	60.7
Orbital dipole	0.9	1.9	7.1	1.3	1.3	1.7	1.7	2.2	2.3	3.4	3.3	3.3	3.3	33.7
Gain sampling	0.5	0.8	1.9	0.8	0.8	0.5	0.5	0.9	0.9	0.7	0.7	0.7	0.7	10.4
1 Hz spike sampling	0.3	0.4	1.6											2.4
Correlated noise sampling	2.0	4.0	21.7	2.8	2.9	3.3	3.6	5.1	5.4	8.0	7.7	7.2	8.5	81.3
Correlated noise PSD sampling	4.8	5.9	1.5	0.2	0.2	0.3	0.3	0.5	0.4	0.7	0.6	0.6	0.7	16.7
TOD binning (\mathbf{P}^t operation)	0.1	0.1	4.0	0.5	0.5	0.7	0.8	0.8	0.8	1.2	1.2	1.2	1.2	13.1
Mapmaking						6.4	7.0	8.9	8.1	11.1	9.5	14.4	14.3	15.3
Sum of other TOD processing	4.4	8.6	44.4	14.7	4.6	5.1	5.0	9.4	7.7	8.1	6.8	8.6	8.7	136.1
TOD processing cost per sample	15.5	26.8	104.5	23.0	24.1	27.6	27.9	40.3	37.4	51.7	50.6	51.9	54.6	535.9
Amplitude sampling														14.0
Spectral index sampling														25.5
Total cost per sample														581.2

Table 3. Flagging statistics

Band	Flagged (%)	Discarded (%)	Used (%)
<i>K</i>	1.72	0.87	97.4
<i>Ka</i>	1.64	0.88	97.5
<i>Q1</i>	1.84	0.84	96.5
<i>Q2</i>	1.62	0.81	97.6
<i>V1</i>	1.62	1.10	97.3
<i>V2</i>	1.61	1.01	97.4
<i>W1</i>	1.76	1.03	97.2
<i>W2</i>	1.60	0.81	97.6
<i>W3</i>	1.61	0.87	97.5
<i>W4</i>	1.60	0.81	97.6

results reported in [Bennett et al. \(2013\)](#) included roughly 98.4 % of the total data volume. A full accounting of all data cuts can be found in Table 1.8 of [Greason et al. \(2012\)](#). In total, we flag the same data indicated in the fiducial *WMAP* analysis, and use the same planet flags

As shown in [Galloway et al. \(2022\)](#), a large fraction of Commander3’s computational time is spent performing FFTs on individual scans. Rather than truncating datastreams to have lengths equal to “magic numbers” for which FFTW ([Frigo & Johnson 2005](#)) is fastest, as in [Galloway et al. \(2022\)](#), we split the data into scans of length 2^N , where $N = 22$ for *K*–*Q*, $N = 23$ for *V*–*W*. This yields scans with lengths of 6.21 days for *K*- and *Ka*-band, 4.97 days for *Q*-band, 7.46 days for *V*-band, and 4.97 days for *W*-band. These datastream lengths are short enough to be processed quickly and distributed efficiently across multiple processors, while being long enough to properly characterize the noise properties of the timestreams, whose f_{knee} ’s are on the order 1 mHz. Most importantly, FFTW performs fastest when the datastream is of length 2^N .

When rechunking the data, timestreams of length 2^N were interrupted by events logged in Table 1.8 of [Greason et al. \(2012\)](#). When we encountered these events, TOD segments that were interrupted by the event were appended to the previous TOD, in most cases creating TODs with lengths $> 2^N$. We found that events of length $< 2^N$ were too short to accurately estimate the noise PSD parameters. This criterion led us to discard these otherwise useful data. In addition, when $> 10\%$ of the TOD was flagged, the large number of gaps in the data made the constrained realizations unreliable, as well as biasing the noise PSD parameters. Together, these two effects led to $\simeq 1\%$ of the data to be discarded despite being of acceptable quality. We present the full statistics for our maps in Table 3. In total, the COSMOGLOBE maps use slightly less data than the *WMAP9* official products, which had a total efficiency of $\simeq 98.4\%$ ([Bennett et al. 2013](#)). The total difference in data volume can be entirely accounted for by the cuts described in this paragraph.

djfkasajf lasj fkfdjas fklsaj lfjdsf kfkj jasdlkfj aslkfj klsadjf lsdajf lkasdj flksdj kfslsajdk f djfkasajf lasj fkfdjas fklsaj lfjdsf kfkj jasdlkfj aslkfj klsadjf lsdajf lkasdj flksdj kfslsajdk f djfkasajf lasj fkfdjas fklsaj lfjdsf kfkj jasdlkfj aslkfj klsadjf lsdajf lkasdj flksdj kfslsajdk f djfkasajf lasj fkfdjas fklsaj lfjdsf kfkj jasdlkfj aslkfj klsadjf lsdajf lkasdj flksdj kfslsajdk f

djfkasajf lasj fkfdjas fklsaj lfjdsf kfkj jasdlkfj aslkfj klsadjf lsdajf lkasdj flksdj kfslsajdk f jfkasajf lasj fkfdjas fklsaj lfjdsf kfkj jasdlkfj aslkfj klsadjf lsdajf lkasdj flksdj kfslsajdk f djfkasajf lasj fkfdjas fklsaj lfjdsf kfkj jasdlkfj aslkfj klsadjf lsdajf lkasdj flksdj kfslsajdk f djfkasajf lasj fkfdjas fklsaj lfjdsf kfkj jasdlkfj aslkfj klsadjf lsdajf lkasdj flksdj kfslsajdk f

djfkasajf lasj fkfdjas fklsaj lfjdsf kfkj jasdlkfj aslkfj klsadjf lsdajf lkasdj flksdj kfslsajdk f djfkasajf lasj fkfdjas fklsaj lfjdsf kfkj jasdlkfj aslkfj klsadjf lsdajf lkasdj flksdj kfslsajdk f jfkasajf lasj fkfdjas fklsaj lfjdsf kfkj jasdlkfj aslkfj klsadjf lsdajf lkasdj flksdj kfslsajdk f djfkasajf lasj fkfdjas fklsaj lfjdsf kfkj jasdlkfj aslkfj klsadjf lsdajf lkasdj flksdj kfslsajdk f

djfkasajf lasj fkfdjas fklsaj lfjdsf kfkj jasdlkfj aslkfj klsadjf lsdajf lkasdj flksdj kfslsajdk f djfkasajf lasj fkfdjas fklsaj lfjdsf kfkj jasdlkfj aslkfj klsadjf lsdajf lkasdj flksdj kfslsajdk f jfkasajf lasj fkfdjas fklsaj lfjdsf kfkj jasdlkfj aslkfj klsadjf lsdajf lkasdj flksdj kfslsajdk f djfkasajf lasj fkfdjas fklsaj lfjdsf kfkj jasdlkfj aslkfj klsadjf lsdajf lkasdj flksdj kfslsajdk f

5. Data

5.1. Publicly available WMAP products

5.2. TOD pre-processing and data selection

Chunking, events, compression, data volume, planet flags, pixelized pointing

5.3. Inspection of time-ordered WMAP data

Figure with raw TOD, WMAP cleaned, components, total, difference etc.

The full nine-year *WMAP* archive spans from August 10, 2001 to August 10, 2010, with the raw uncalibrated data spanning 626 GB. A little over 1 % of the data were lost or rejected due to incomplete satellite telemetry, thermal disturbances, spacecraft anomalies, and station-keeping maneuvers, with an extra 0.1 % rejected due to planet flagging ([Bennett et al. 2003b](#); [Hinshaw et al. 2007, 2009](#); [Bennett et al. 2013](#)). The final

sadjf lsdajf lkasdj flksdj kflsajdk f djfksajf lasj fkfdas fklsaj lfjdsf kfkj jasdlkfj aslkfj klsadjf lsdajf lkasdj flksdj kflsajdk f

djfksajf lasj fkfdas fklsaj lfjdsf kfkj jasdlkfj aslkfj klsadjf lsdajf lkasdj flksdj kflsajdk f djfksajf lasj fkfdas fklsaj lfjdsf kfkj jasdlkfj aslkfj klsadjf lsdajf lkasdj flksdj kflsajdk f djfksajf lasj fkfdas fklsaj lfjdsf kfkj jasdlkfj aslkfj klsadjf lsdajf lkasdj flksdj kflsajdk f jfksajf lasj fkfdas fklsaj lfjdsf kfkj jasdlkfj aslkfj klsadjf lsdajf lkasdj flksdj kflsajdk f djfksajf lasj fkfdas fklsaj lfjdsf kfkj jasdlkfj aslkfj klsadjf lsdajf lkasdj flksdj kflsajdk f djfksajf lasj fkfdas fklsaj lfjdsf kfkj jasdlkfj aslkfj klsadjf lsdajf lkasdj flksdj kflsajdk f

djfksajf lasj fkfdas fklsaj lfjdsf kfkj jasdlkfj aslkfj klsadjf lsdajf lkasdj flksdj kflsajdk f jfksajf lasj fkfdas fklsaj lfjdsf kfkj jasdlkfj aslkfj klsadjf lsdajf lkasdj flksdj kflsajdk f djfksajf lasj fkfdas fklsaj lfjdsf kfkj jasdlkfj aslkfj klsadjf lsdajf lkasdj flksdj kflsajdk f djfksajf lasj fkfdas fklsaj lfjdsf kfkj jasdlkfj aslkfj klsadjf lsdajf lkasdj flksdj kflsajdk f

djfksajf lasj fkfdas fklsaj lfjdsf kfkj jasdlkfj aslkfj klsadjf lsdajf lkasdj flksdj kflsajdk f djfksajf lasj fkfdas fklsaj lfjdsf kfkj jasdlkfj aslkfj klsadjf lsdajf lkasdj flksdj kflsajdk f djfksajf lasj fkfdas fklsaj lfjdsf kfkj jasdlkfj aslkfj klsadjf lsdajf lkasdj flksdj kflsajdk f djfksajf lasj fkfdas fklsaj lfjdsf kfkj jasdlkfj aslkfj klsadjf lsdajf lkasdj flksdj kflsajdk f

djfksajf lasj fkfdas fklsaj lfjdsf kfkj jasdlkfj aslkfj klsadjf lsdajf lkasdj flksdj kflsajdk f djfksajf lasj fkfdas fklsaj lfjdsf kfkj jasdlkfj aslkfj klsadjf lsdajf lkasdj flksdj kflsajdk f djfksajf lasj fkfdas fklsaj lfjdsf kfkj jasdlkfj aslkfj klsadjf lsdajf lkasdj flksdj kflsajdk f djfksajf lasj fkfdas fklsaj lfjdsf kfkj jasdlkfj aslkfj klsadjf lsdajf lkasdj flksdj kflsajdk f

In a preliminary `Commander3` run, we discovered an unbounded rise in the K -band absolute calibration, g_0 , and the dipole in the AME component of the sky. Because the AME is strongest among all bands at K -band, any increase in the K -band absolute calibration can easily be accounted for by changing the amplitude of the AME, while leaving goodness-of-fit tests such as relative- χ^2 and residual maps unaffected.

In order to break this degeneracy, it was necessary to impose a prior either on the AME itself or on the absolute calibration. The AME prior we explored followed the approach of [Andersen et al. \(2022\)](#), in which the prior mean was the *Planck* DR4 857 GHz map scaled by $3 \cdot 10^{-5}$, and the variance is given in angular scales by a parameter q . We found that a prior of $q = 10^{-2} \mu\text{K}^2$ was necessary to stabilize the gain, resulting in an AME map that was nearly identical to the *Planck* 857 GHz band. As this gave a result that was inconsistent with many previous results, we opted instead to sample the absolute calibration instead.

Any error in g_0 leads to a residual due to the large Solar dipole. In practice, we found that the typical variation of g_0 was 0.002, giving a relative error of $\sim 0.1\%$. This variation induces a $\sim 6 \mu\text{K}$ Solar dipole uncertainty, which is easily attributed to AME during component separation. In Figure 33, we demonstrate this effect on recovered AME maps using extreme g_0 values of 1.175 and 1.9. We find that AME maps consistent with those presented in [Bennett et al. \(2013\)](#) and [Planck Collaboration X \(2016\)](#) are recovered when g_0 is between 1.180 and 1.182. Based on this analysis, we sample g_0 from a Gaussian with mean 1.1815 and standard deviation 0.001.

[Bennett et al. \(2013\)](#) and [Planck Collaboration X \(2016\)](#) find AME peak frequencies 12.0–17.5 GHz and 17–23 GHz, respectively, both with low signal-to-noise at high Galactic latitude and with structure along the plane. The Q-U-I JOint Tenerife

Experiment (QUIJOTE) has recently released maps of the sky with approximately 70 % sky coverage at frequencies 11, 13, 17, and 19 GHz ([Rubiño-Martín et al. 2023](#)). QUIJOTE is optimized for characterizing the polarized sky, and constraints from, e.g., [de la Hoz et al. \(2023\)](#), will be critical for future polarized synchrotron SED characterization and polarized AME limits. While in principle the AME SED can be constrained by a joint *WMAP/LFI/QUIJOTE* analysis, we consider this outside of the scope of the paper, which aims to evaluate the effect of jointly analyzing *WMAP* and *Planck LFI* at the TOD level. Future analysis will include the QUIJOTE data, and hopefully break the g_0 -AME degeneracy.

A key motivation of the COSMOGLOBE project is to evaluate whether it is feasible to perform a joint analysis of two datasets simultaneously, each with its own particular processing requirements and algorithmic treatment. One of the results from [Watts et al. \(2022\)](#) was that most of the data processing overlapped between *WMAP* and *Planck LFI*, with the notable exception of mapmaking. While the algorithmic requirements have been discussed in the previous section, we have not yet quantified the requirements in terms of RAM and CPU hours. In Table 2, we enumerate the RAM requirements and CPU time for each sampling step using the local cluster at the Institute of Theoretical Astrophysics at the University of Oslo. The node that these numbers come from used 128 cores of an AMD EPYC 7H12, 2.6 GHz machine with 2 TB of memory. As `Commander3` is parallelized and used 128 cores, wall hours in Table 2 can be obtained by dividing by 128.

Despite the relatively small data volume spanned by *WMAP*, the CPU time is comparable to each of the LFI channels. By far the largest reason for this is the mapmaking step, which requires looping over the entire dataset for each matrix multiplication, a process which must be repeated ~ 20 times. This is vastly sped up by the use of a low resolution preconditioner, reducing the number of iterations by an order of magnitude.

(One thing I would like to explain – why does it take so much longer for TOD operations? My initial thought was that each timestream requires two timestreams for each horn, but that's not enough.)

Additionally, operations that require creating timestreams for each detector, i.e., TOD projection, sidelobe evaluation, and orbital dipole projection, take much longer than expected from a pure data volume scaling. Part of this is due to each *WMAP* radiometer needing to evaluate the sky in two pixels simultaneously, doubling the expected workload. The operations of gain sampling and correlated noise sampling include multiple FFTs. Typical LFI TODs are of length $\sim 200\,000$, an order of magnitude smaller than the *WMAP* TODs of length 2^{22-23} .

(Need to expand “other”)

To compare the TODs, it's important to look at the *WMAP* gain model,

$$g = \alpha \frac{\bar{V} - V_\circ - \beta(T_{\text{RXB}} - 290 \text{ K})}{T_{\text{FPA}} - T_\circ} + (m\Delta t + c), \quad (29)$$

where α , V_\circ , β , T_\circ , m , and c are fit to a constant value across the mission for each radiometer. \bar{V} are radio frequency bias powers per detector, and T_{RXB} and T_{FPA} are the receiver box and focal plane assembly temperatures, which are recorded every 23.04 s. Since we couldn't find the exact thermistors that recorded T_{RXB} and T_{FPA} that were used for the gain solution, we are unable to evaluate this exactly. Although we are unable to reproduce the exact gain model parametrized in [Greason et al. \(2012\)](#), the ~ 20 s time dependence of the gain model on housekeeping data

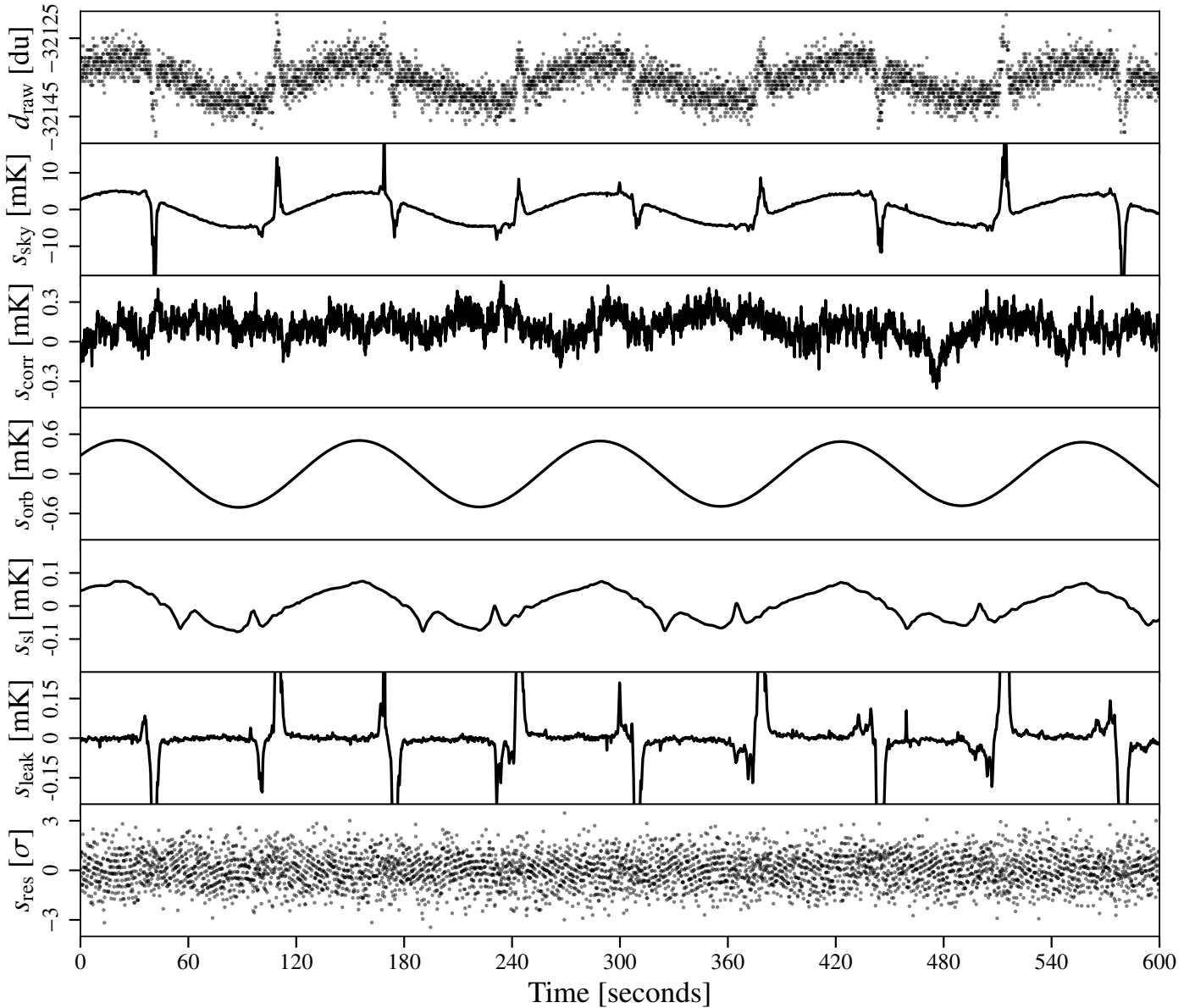


Fig. 1. Each of the timestreams that go into the model. Note the varying dynamic ranges of each plot.

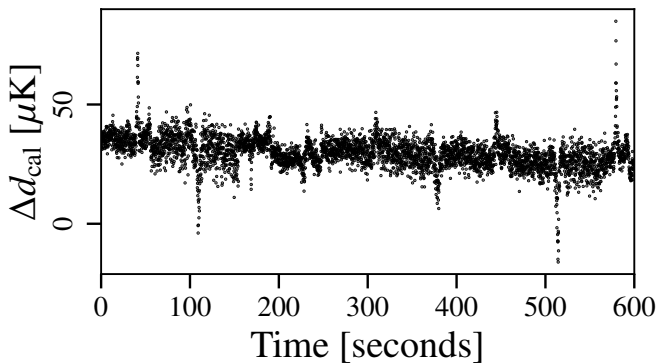


Fig. 2. Difference between the COSMOGLOBE $d_{\text{cal}} = d/g - b - s_{\text{sl}}$ and the delivered calibrated TOD from WMAP.

is a plausible explanation for the time-dependent noise variation in the different calibrated data solutions.

As reported in Hinshaw et al. (2007), the calibrated data archive has been calibrated using the procedure listed above, with a baseline subtracted each hour and the sidelobe subtracted. Figure 2 shows the COSMOGLOBE timestream $d/g - b - s_{\text{sl}}$ with the WMAP delivered calibrated signal subtracted. The most prominent feature is a $\sim 25 \mu\text{K}$ offset, which is unsurprising, given the different treatment of baselines in our two pipelines. The second obvious difference is a series of spikes associated with Galactic plane crossings. The differences of order $50 \mu\text{K}$ correspond to sky brightness of order 10 mK , equivalent to $\sim 0.5\%$ deviations in the gain solution. This is twice as large as the 0.2% uncertainty estimated in Bennett et al. (2013) based on end-to-end simulations.

On longer timescales, as displayed in Figure 3, the most prominent feature is a signal of amplitude 0.2 mK . This likely due to the hourly baseline subtraction mentioned above, which contrasts with the COSMOGLOBE approach of assigning a linear baseline solution for the entire scan. However, the variations are commensurate with correlated noise, which for K113 has $f_{\text{knee}} \sim 0.5 \text{ mHz}$, corresponding to a little over half an hour.

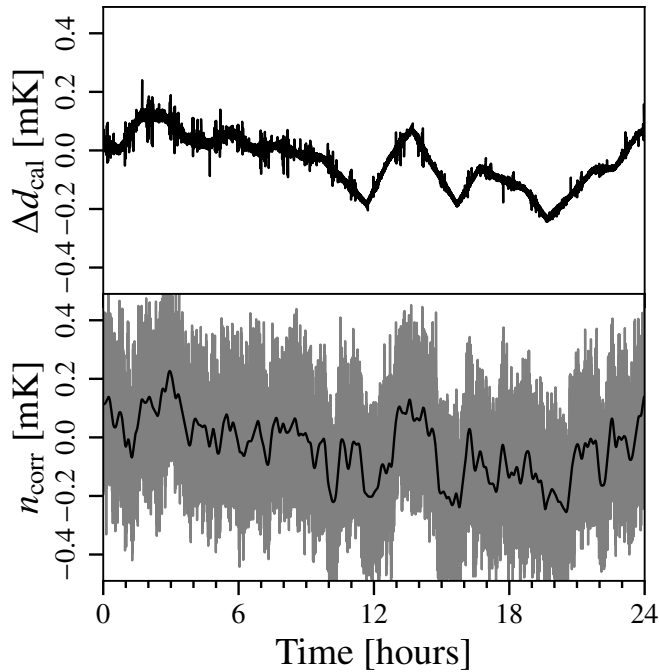


Fig. 3. (top) Difference between the COSMOGLOBE $d_{\text{cal}} = d/g - \mathbf{b} - \mathbf{s}_{\text{sl}}$ and the delivered calibrated TOD from WMAP. (bottom) Raw correlated noise (gray) and smoothed data with Gaussian kernel (black). This shows more clearly the hourly baseline subtraction from the WMAP treatment.

Therefore, the hourlong baseline subtraction essentially acts as a destriper, removing an estimate of the correlated noise. To test this hypothesis, we plot a realization of correlated noise generated by `Commander`, and find that the signals are very similar, both in amplitude and morphology.

6. Markov chains and parameter correlations

These parameters are themselves sampled conditioned on a full sky model.

Remember that the frequency maps themselves are deterministic functions of the low-level sampled parameters.

djfksajf lasj fkdjas fklsaj lfjdsf kfkj jasdlkfj aslkfj klsadjf lsdajf lkasdj flksdj kfslsajdk f djfksajf lasj fkdjas fklsaj lfjdsf kfkj jasdlkfj aslkfj klsadjf lsdajf lkasdj flksdj kfslsajdk f djfksajf lasj fkdjas fklsaj lfjdsf kfkj jasdlkfj aslkfj klsadjf lsdajf lkasdj flksdj kfslsajdk f djfksajf lasj fkdjas fklsaj lfjdsf kfkj jasdlkfj aslkfj klsadjf lsdajf lkasdj flksdj kfslsajdk f jfksajf lasj fkdjas fklsaj lfjdsf kfkj jasdlkfj aslkfj klsadjf lsdajf lkasdj flksdj kfslsajdk f djfksajf lasj fkdjas fklsaj lfjdsf kfkj jasdlkfj aslkfj klsadjf lsdajf lkasdj flksdj kfslsajdk f

djfksajf lasj fkdjas fklsaj lfjdsf kfkj jasdlkfj aslkfj klsadjf lsdajf lkasdj flksdj kfslsajdk f jfksajf lasj fkdjas fklsaj lfjdsf kfkj jasdlkfj aslkfj klsadjf lsdajf lkasdj flksdj kfslsajdk f djfksajf lasj fkdjas fklsaj lfjdsf kfkj jasdlkfj aslkfj klsadjf lsdajf lkasdj flksdj kfslsajdk f djfksajf lasj fkdjas fklsaj lfjdsf kfkj jasdlkfj aslkfj klsadjf lsdajf lkasdj flksdj kfslsajdk f

djfksajf lasj fkdjas fklsaj lfjdsf kfkj jasdlkfj aslkfj klsadjf lsdajf lkasdj flksdj kfslsajdk f djfksajf lasj fkdjas fklsaj lfjdsf kfkj jasdlkfj aslkfj klsadjf lsdajf lkasdj flksdj kfslsajdk f djfksajf lasj fkdjas fklsaj lfjdsf kfkj jasdlkfj aslkfj klsadjf lsdajf lkasdj flksdj kfslsajdk f djfksajf lasj fkdjas fklsaj lfjdsf kfkj jasdlkfj aslkfj klsadjf lsdajf lkasdj flksdj kfslsajdk f

djfksajf lasj fkdjas fklsaj lfjdsf kfkj jasdlkfj aslkfj klsadjf lsdajf lkasdj flksdj kfslsajdk f djfksajf lasj fkdjas fklsaj lfjdsf kfkj jasdlkfj aslkfj klsadjf lsdajf lkasdj flksdj kfslsajdk f djfksajf lasj fkdjas fklsaj lfjdsf kfkj jasdlkfj aslkfj klsadjf lsdajf lkasdj flksdj kfslsajdk f djfksajf lasj fkdjas fklsaj lfjdsf kfkj jasdlkfj aslkfj klsadjf lsdajf lkasdj flksdj kfslsajdk f

The second main deviation... is in the treatment the noise power spectra. As shown in Sect 2.5 of [Jarosik et al. \(2007\)](#), the noise autocorrelation spectrum is fit on a year-by-year basis to a polynomial in $\log(\Delta t)$, where Δt is the time lag between data points. This method is very similar to the Commander3 approach, which fits for the power spectrum in Fourier space using a correlated noise model of the form $\sigma_0^2(f/f_{\text{knee}})^\alpha$. Properly parameterized, these two approaches should yield similar results, albeit with different levels of uncertainty and time resolution. However, we have confirmed that in many cases the simple $1/f$ noise model does not fit the signal-subtracted TOD, yielding χ^2 values that are up to 10σ discrepant from their expected values. [Show, discuss figure with the PSDs, residual spectrum, and Bessel filter.]

Deviations from the $1/f$ model consist either of a linear increase or downturn above 10 Hz. This can be partially explained by the use of a two pole Bessel low-pass filter just prior to signal quantization, which introduces a 2.62% correlation between 25.6 ms sample integrations ([Jarosik et al. 2003b](#), Sect. 5.3). The exact form of the Bessel filter was not used on flight data, but rather the parametric fit as discussed above. However, the filter is designed to reduce the signal by half at 100 Hz, and as such has a negligible effect.

djfksajf lasj fkdjas fklsaj lfjdsf kfkj jasdlkfj aslkfj klsadjf lsdajf lkasdj flksdj kfslsajdk f djfksajf lasj fkdjas fklsaj lfjdsf kfkj jasdlkfj aslkfj klsadjf lsdajf lkasdj flksdj kfslsajdk f djfksajf lasj fkdjas fklsaj lfjdsf kfkj jasdlkfj aslkfj klsadjf lsdajf lkasdj flksdj kfslsajdk f jfksajf lasj fkdjas fklsaj lfjdsf kfkj jasdlkfj aslkfj klsadjf lsdajf lkasdj flksdj kfslsajdk f

sadjf lsdajf lkasdj flksdj kfslsajdk f djfksajf lasj fkdjas fklsaj lfjdsf kfkj jasdlkfj aslkfj klsadjf lsdajf lkasdj flksdj kfslsajdk f
djfksajf lasj fkdjas fklsaj lfjdsf kfkj jasdlkfj aslkfj klsadjf lsdajf lkasdj flksdj kfslsajdk f djfksajf lasj fkdjas fklsaj lfjdsf kfkj jasdlkfj aslkfj klsadjf lsdajf lkasdj flksdj kfslsajdk f djfksajf lasj fkdjas fklsaj lfjdsf kfkj jasdlkfj aslkfj klsadjf lsdajf lkasdj flksdj kfslsajdk f djfksajf lasj fkdjas fklsaj lfjdsf kfkj jasdlkfj aslkfj klsadjf lsdajf lkasdj flksdj kfslsajdk f djfksajf lasj fkdjas fklsaj lfjdsf kfkj jasdlkfj aslkfj klsadjf lsdajf lkasdj flksdj kfslsajdk f

djfksajf lasj fkdjas fklsaj lfjdsf kfkj jasdlkfj aslkfj klsadjf lsdajf lkasdj flksdj kfslsajdk f djfksajf lasj fkdjas fklsaj lfjdsf kfkj jasdlkfj aslkfj klsadjf lsdajf lkasdj flksdj kfslsajdk f djfksajf lasj fkdjas fklsaj lfjdsf kfkj jasdlkfj aslkfj klsadjf lsdajf lkasdj flksdj kfslsajdk f djfksajf lasj fkdjas fklsaj lfjdsf kfkj jasdlkfj aslkfj klsadjf lsdajf lkasdj flksdj kfslsajdk f djfksajf lasj fkdjas fklsaj lfjdsf kfkj jasdlkfj aslkfj klsadjf lsdajf lkasdj flksdj kfslsajdk f

djfksajf lasj fkdjas fklsaj lfjdsf kfkj jasdlkfj aslkfj klsadjf lsdajf lkasdj flksdj kfslsajdk f djfksajf lasj fkdjas fklsaj lfjdsf kfkj jasdlkfj aslkfj klsadjf lsdajf lkasdj flksdj kfslsajdk f djfksajf lasj fkdjas fklsaj lfjdsf kfkj jasdlkfj aslkfj klsadjf lsdajf lkasdj flksdj kfslsajdk f djfksajf lasj fkdjas fklsaj lfjdsf kfkj jasdlkfj aslkfj klsadjf lsdajf lkasdj flksdj kfslsajdk f djfksajf lasj fkdjas fklsaj lfjdsf kfkj jasdlkfj aslkfj klsadjf lsdajf lkasdj flksdj kfslsajdk f

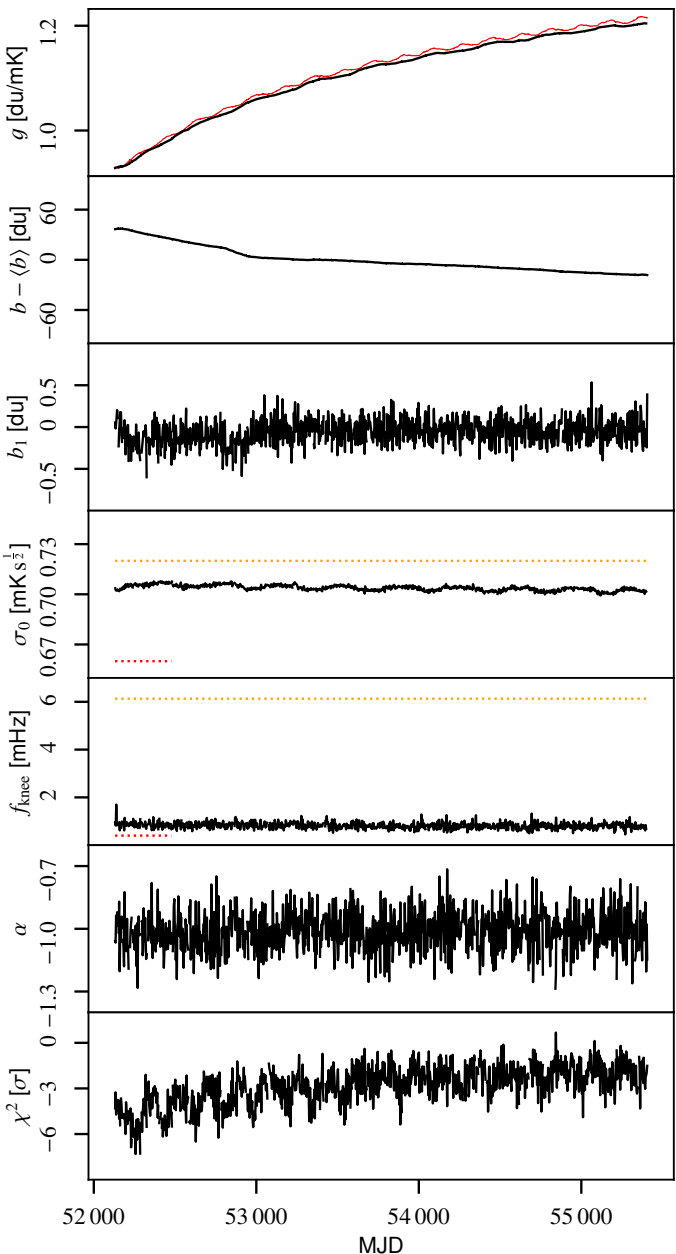


Fig. 4. Overview of K113

7. Low-level posterior distributions

7.1. Gain and baselines

7.2 Transmission imbalance

7.3 Instrumental noise and goodness-of-fit

Need to have the things that go directly into likelihood, the template-corrected WMAP data, theirs versus ours.

Show the low-resolution one. Plotting the W3-W4, W1-W2, V1-V2, Q1-Q2, K_a-0.32K

We need to have a brief overview of the sky model

We need to have a brief overview of the
Also need to have the sky model added

Include the SED from the 03 paper, reference it, remove the power law.

Resources table as from Q1

Resources table, as from Q1:
djfksajf lasj fkjdas fklasj lfjdsl kfkj jasdlnkfj aslkfj klsadljf ls-dafif lkasdi flksdi kflsaikd f djkcsaif lasi fkjdas fklasai lfidsl kfki

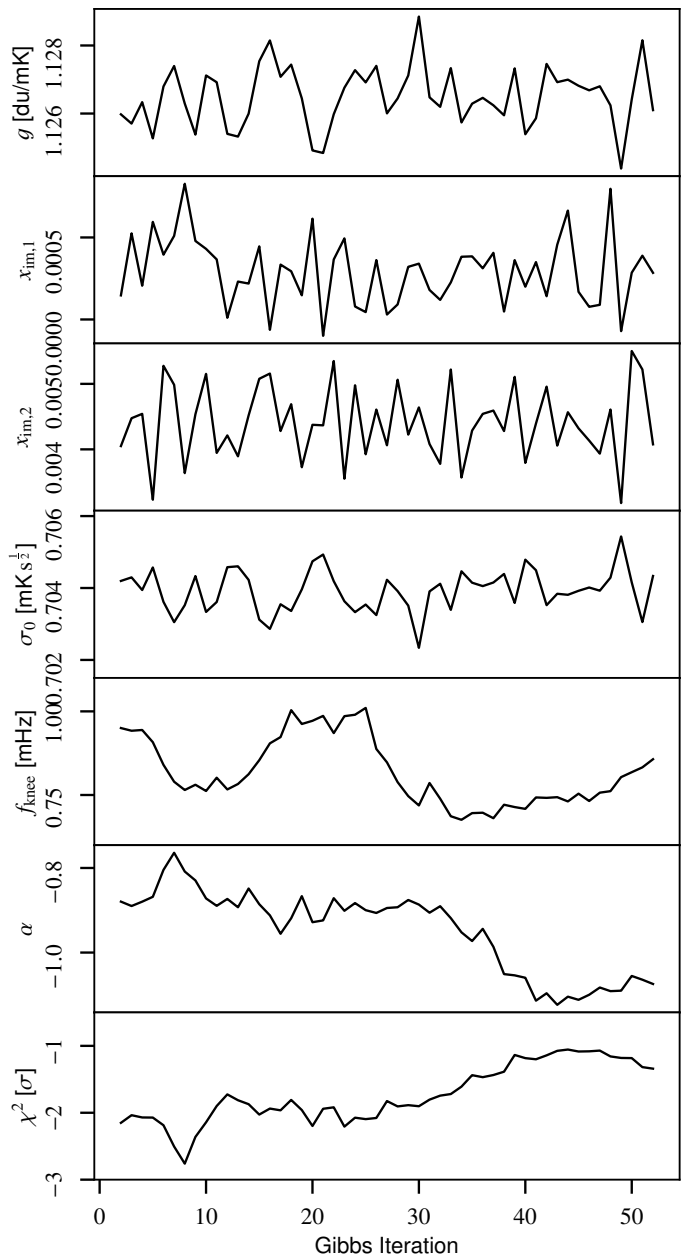
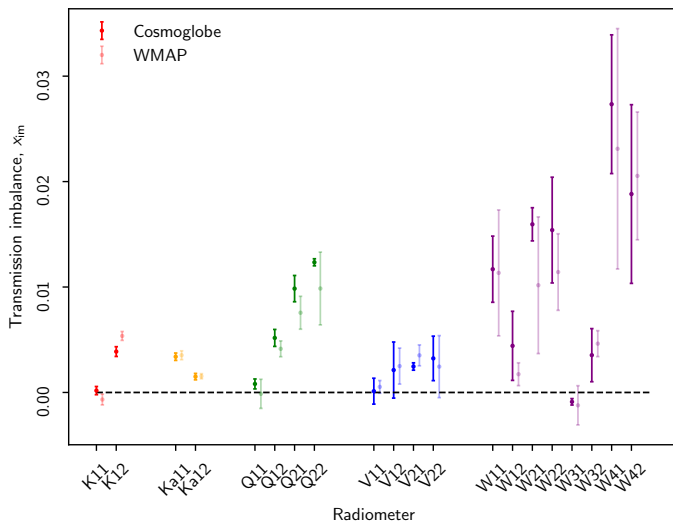


Fig. 5. Overview of K113

jasdlkjfj aslkfj klsadjf lsdajf lkasdj flksdj kfslsajdk f djfksajf lasj fkdjas fklsaj lfjds1 kfkj jasdlkjfj aslkfj klsadjf lsdajf lkasdj flksdj kfslsajdk f jfksajf lasj fkdjas fklsaj lfjds1 kfkj jasdlkjfj aslkfj kl-sadjf lsdajf lkasdj flksdj kfslsajdk f djfksajf lasj fkdjas fklsaj lfjds1 kfkj jasdlkjfj aslkfj klsadjf lsdajf lkasdj flksdj kfslsajdk f

dfjkſajf lasj fkſdjas fkſlſaj lfjdſl kfkj jaſdlkfj aſlkſfj klsadſj lſ-dajf lkadſj fkſdſj kfſlſajdk f jfkſajf lasj fkſdjas fkſlſaj lfjdſl kfkj jaſdlkfj aſlkſfj klsadſj lſdajf lkadſj fkſdſj kfſlſajdk f dfjkſajf lasj fkſdjas fkſlſaj lfjdſl kfkj jaſdlkfj aſlkſfj klsadſj lſdajf lkadſj fkſdſj kfſlſajdk f djfkſajf lasj fkſdjas fkſlſaj lfjdſl kfkj jaſdlkfj aſlkſfj klsadſj lſdajf lkadſj fkſdſj kfſlſajdk f jfkſajf lasj fkſdjas fkſlſaj lfjdſl kfki iaſdlkfj aſlkſfj klsadſj lſdajf lkadſj fkſsdi kfſlſaidk f

djfksajf lasj fkfdjas fklsaj lfjdsj kfkj jasdlnkfj aslkfj klsadljf ls-
dajf lkasdj flksdj kfslsajdk f djfksajf lasj fkfdjas fklsaj lfjdsj kfkj
jasdlnkfj aslkfj klsadljf lsdajf lkasdj flksdj kfslsajdk f jfkssajf lasj
fkfdjas fklsaj lfjdsj kfkj jasdlnkfj aslkfj klsadljf lsdajf lkasdj flksdj
kfslsajdk f difksaif lasj fkfdias fklsai lfjdsj kfki jasdlnkfj aslkfj kl-

**Fig. 6.** Transmission imbalance**Table 4.** Transmission imbalance parameters for each *WMAP* radiometer as estimated in the current analysis (*second column*) and in the official 9-year *WMAP* analysis (*third column*). Our uncertainties indicate 1σ marginal posterior standard deviations.

RADIOMETER	x_{im}^{CG}	x_{im}^{WMAP}
K11	0.00018 ± 0.00013	-0.00067 ± 0.00017
K12	0.00388 ± 0.00015	0.00536 ± 0.00014
Ka11	0.00339 ± 0.00012	0.00353 ± 0.00017
Ka12	0.00150 ± 0.00010	0.00154 ± 0.00008
Q11	0.00081 ± 0.00016	-0.00013 ± 0.00046
Q12	0.00517 ± 0.00027	0.00414 ± 0.00025
Q21	0.00985 ± 0.00042	0.00756 ± 0.00052
Q22	0.01235 ± 0.00011	0.00986 ± 0.00115
V11	0.00012 ± 0.00041	0.00053 ± 0.00020
V12	0.00212 ± 0.00089	0.00250 ± 0.00057
V21	0.00246 ± 0.00012	0.00352 ± 0.00033
V22	0.00323 ± 0.00070	0.00245 ± 0.00098
W11	0.01169 ± 0.00105	0.01134 ± 0.00199
W12	0.00442 ± 0.00109	0.00173 ± 0.00036
W21	0.01595 ± 0.00052	0.01017 ± 0.00216
W22	0.01540 ± 0.00167	0.01142 ± 0.00121
W31	-0.00089 ± 0.00010	-0.00122 ± 0.00062
W32	0.00354 ± 0.00084	0.00463 ± 0.00041
W41	0.02734 ± 0.00219	0.02311 ± 0.00380
W42	0.01882 ± 0.00282	0.02054 ± 0.00202

sadjf lsdajf lkasdj flksdj kflsajdk f djfksajf lasj fkddas fklsaj lfjds
kfkj jasdlkfj aslkfj klsadjf lsdajf lkasdj flksdj kflsajdk f jfksajf
lasj fkddas fklsaj lfjds lfkj jasdlkfj aslkfj klsadjf lsdajf lkasdj
flksdj kflsajdk f

djfksajf lasj fkddas fklsaj lfjds lfkj jasdlkfj aslkfj klsadjf lsdajf
lkasdj flksdj kflsajdk f djfksajf lasj fkddas fklsaj lfjds lfkj
jasdlkfj aslkfj klsadjf lsdajf lkasdj flksdj kflsajdk f jfksajf lasj
fkddas fklsaj lfjds lfkj jasdlkfj aslkfj klsadjf lsdajf lkasdj flksdj
kflsajdk f djfksajf lasj fkddas fklsaj lfjds lfkj jasdlkfj aslkfj
klsadjf lsdajf lkasdj flksdj kflsajdk f djfksajf lasj fkddas fklsaj
lfjds lfkj jasdlkfj aslkfj klsadjf lsdajf lkasdj flksdj kflsajdk f

djfksajf lasj fkddas fklsaj lfjds lfkj jasdlkfj aslkfj klsadjf lsdajf
lkasdj flksdj kflsajdk f djfksajf lasj fkddas fklsaj lfjds lfkj
jasdlkfj aslkfj klsadjf lsdajf lkasdj flksdj kflsajdk f djfksajf lasj
fkddas fklsaj lfjds lfkj jasdlkfj aslkfj klsadjf lsdajf lkasdj flksdj
kflsajdk f jfksajf lasj fkddas fklsaj lfjds lfkj jasdlkfj aslkfj
klsadjf lsdajf lkasdj flksdj kflsajdk f jfksajf lasj fkddas fklsaj
lfjds lfkj jasdlkfj aslkfj klsadjf lsdajf lkasdj flksdj kflsajdk f

Article number, page 14 of 51

Table 5. Transmission imbalance template amplitudes for each *WMAP* radiometer as estimated by fitting the official templates to low-resolution difference maps between *Cosmoglobe* and *WMAP*. The templates are provided in mK, and the template amplitudes are therefore dimensionless. The fourth column lists the relative decrease in standard deviation, $\sqrt{\sigma_{\text{raw}}^2 - \sigma_{\text{corr}}^2}/\sigma_{\text{raw}}$, after subtracting the best-fit templates in percent.

DA	a_1	a_2	$\Delta\sigma[\%]$
K1	-27.5	-50.6	30
Ka1	-1.4	-1.9	25
Q1	-30.0	-71.6	11
Q2	-7.1	-1.5	20
V1	-32.8	-53.4	6
V2	8.8	-4.1	16
W1	-2.8	4.6	8
W2	-6.9	-3.5	11
W3	29.1	53.4	12
W4	15.5	-6.8	52

Table 6. Summary of noise properties.

Radiometer ..	Diode	Sensitivity, σ_0 (mK \sqrt{s})			Knee frequency, f_{knee} (mHz)			Slope, α
		GSFC	WMAP	CG/ $\sqrt{2}$	GSFC	WMAP	CG/ $\sqrt{2}$	
K11	1	0.72	0.66	0.704 ± 0.002	6.13	0.4	0.82 ± 0.20	-1.01 ± 0.10
	2			0.708 ± 0.003			0.63 ± 0.14	-0.95 ± 0.10
K12	1	0.87	0.75	0.796 ± 0.004	5.37	0.51	0.42 ± 0.19	-0.93 ± 0.12
	2			0.780 ± 0.005			0.71 ± 0.15	-1.02 ± 0.10
Ka11	1	0.75	0.71	0.788 ± 0.001	1.66	0.71	1.20 ± 0.22	-1.02 ± 0.09
	2			0.777 ± 0.001			1.19 ± 0.22	-1.02 ± 0.09
Ka12	1	0.77	0.72	0.788 ± 0.003	1.29	0.32	0.62 ± 0.16	-0.99 ± 0.11
	2			0.784 ± 0.001			0.63 ± 0.13	-1.01 ± 0.11
Q11	1	0.99	0.92	0.998 ± 0.002	3.21	1.09	1.06 ± 0.16	-1.09 ± 0.09
	2			0.992 ± 0.002			1.06 ± 0.16	-1.10 ± 0.09
Q12	1	0.95	1.02	1.159 ± 0.007	3.13	0.35	0.45 ± 0.47	-0.98 ± 0.11
	2			1.146 ± 0.007			0.83 ± 0.14	-1.00 ± 0.09
Q21	1	0.89	0.85	0.908 ± 0.002	1.92	5.76	2.88 ± 0.37	-1.10 ± 0.07
	2			0.906 ± 0.002			3.22 ± 0.56	-1.10 ± 0.06
Q22	1	1.04	0.99	1.074 ± 0.004	4.61	8.62	3.95 ± 0.54	-1.11 ± 0.06
	2			1.064 ± 0.003			4.05 ± 0.64	-1.11 ± 0.06
V11	1	1.25	1.22	1.551 ± 0.003	2.56	0.09	1.27 ± 0.15	-0.90 ± 0.06
	2			1.539 ± 0.003			1.19 ± 0.14	-0.89 ± 0.06
V12	1	1.07	1.11	1.398 ± 0.002	4.49	1.41	2.11 ± 0.20	-0.97 ± 0.05
	2			1.432 ± 0.002			1.88 ± 0.17	-0.96 ± 0.05
V21	1	1.01	0.97	1.241 ± 0.298	2.43	0.88	1.50 ± 0.24	-0.95 ± 0.07
	2			1.217 ± 0.294			1.60 ± 0.26	-0.97 ± 0.06
V22	1	1.13	1.1	1.443 ± 0.300	3.06	8.35	4.01 ± 0.85	-1.00 ± 0.08
	2			1.415 ± 0.316			3.08 ± 0.65	-1.01 ± 0.08
W11	1	1.18	1.35	1.938 ± 0.005	16.2	7.88	5.59 ± 0.53	-0.94 ± 0.05
	2			1.895 ± 0.005			8.99 ± 0.85	-0.95 ± 0.04
W12	1	1.41	1.61	2.301 ± 0.005	15.1	0.66	3.91 ± 0.42	-0.89 ± 0.05
	2			2.345 ± 0.006			4.81 ± 0.53	-0.89 ± 0.05
W21	1	1.38	1.61	2.225 ± 0.007	1.76	9.02	13.57 ± 1.47	-0.89 ± 0.03
	2			2.292 ± 0.006			5.06 ± 0.95	-0.93 ± 0.05
W22	1	1.44	1.72	2.291 ± 0.006	0.77	7.47	3.02 ± 0.53	-0.98 ± 0.05
	2			2.232 ± 0.007			7.26 ± 1.05	-0.95 ± 0.04
W31	1	1.47	1.65	2.328 ± 0.005	1.84	0.93	1.30 ± 0.46	-0.99 ± 0.07
	2			2.322 ± 0.006			1.97 ± 0.28	-0.98 ± 0.06
W32	1	1.69	1.86	2.707 ± 0.015	2.39	0.28	1.59 ± 0.29	-0.98 ± 0.07
	2			2.579 ± 0.015			1.40 ± 0.39	-1.00 ± 0.07
W41	1	1.6	1.71	2.519 ± 0.010	8.46	46.5	26.81 ± 1.83	-0.92 ± 0.04
	2			2.479 ± 0.009			24.75 ± 1.63	-0.92 ± 0.04
W42	1	1.43	1.65	2.221 ± 0.017	5.31	26.0	16.10 ± 1.09	-0.94 ± 0.04
	2			2.202 ± 0.015			17.11 ± 1.19	-0.94 ± 0.04

kflsajdk f djfksajf lasj fkddas fklsaj lfjdsf kfkj jasdlkfj aslkfj kl-
sadjf lsdajf lkasdj flksdj kflsajdk f djfksajf lasj fkddas fklsaj lfjdsf
kfkj jasdlkfj aslkfj klsadjf lsdajf lkasdj flksdj kflsajdk f jfksajf
lasj fkddas fklsaj lfjdsf kfkj jasdlkfj aslkfj klsadjf lsdajf lkasdj
flksdj kflsajdk f

djfksajf lasj fkddas fklsaj lfjdsf kfkj jasdlkfj aslkfj klsadjf ls-
dajf lkasdj flksdj kflsajdk f djfksajf lasj fkddas fklsaj lfjdsf kfkj
jasdlkfj aslkfj klsadjf lsdajf lkasdj flksdj kflsajdk f jfksajf lasj
fkddas fklsaj lfjdsf kfkj jasdlkfj aslkfj klsadjf lsdajf lkasdj flksdj
kflsajdk f djfksajf lasj fkddas fklsaj lfjdsf kfkj jasdlkfj aslkfj kl-
sadjf lsdajf lkasdj flksdj kflsajdk f djfksajf lasj fkddas fklsaj lfjdsf
kfkj jasdlkfj aslkfj klsadjf lsdajf lkasdj flksdj kflsajdk f

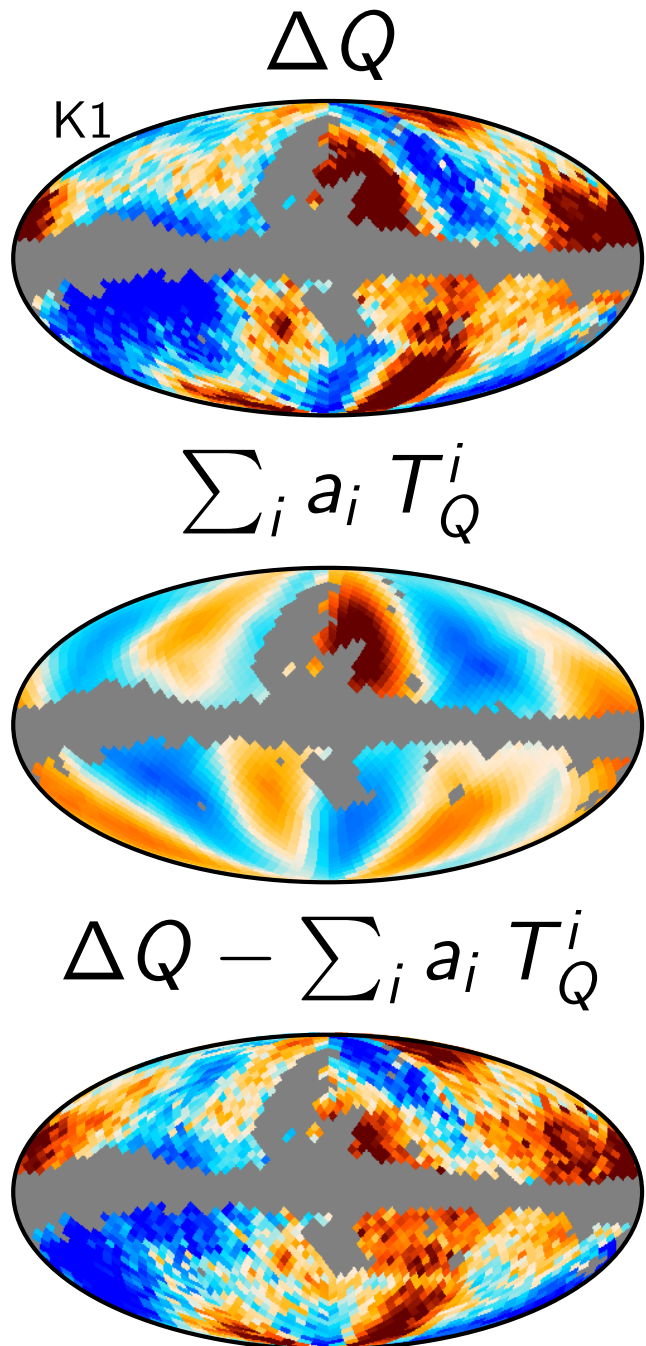


Fig. 7. K-band transmission imbalance templates

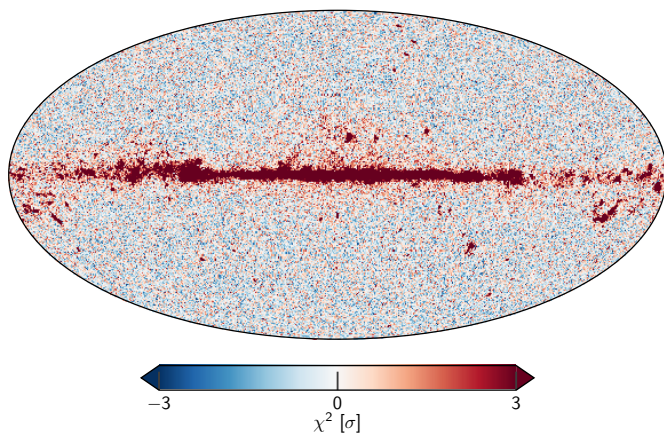


Fig. 8. Reduced- χ^2 , using $n_{\text{dof}} = 300$, which comes from fitting to the regions outside of the K -band processing mask.

8. High-level posterior distributions

8.1. Astrophysical sky model

8.2. Frequency maps

Will combine these spectra shortly

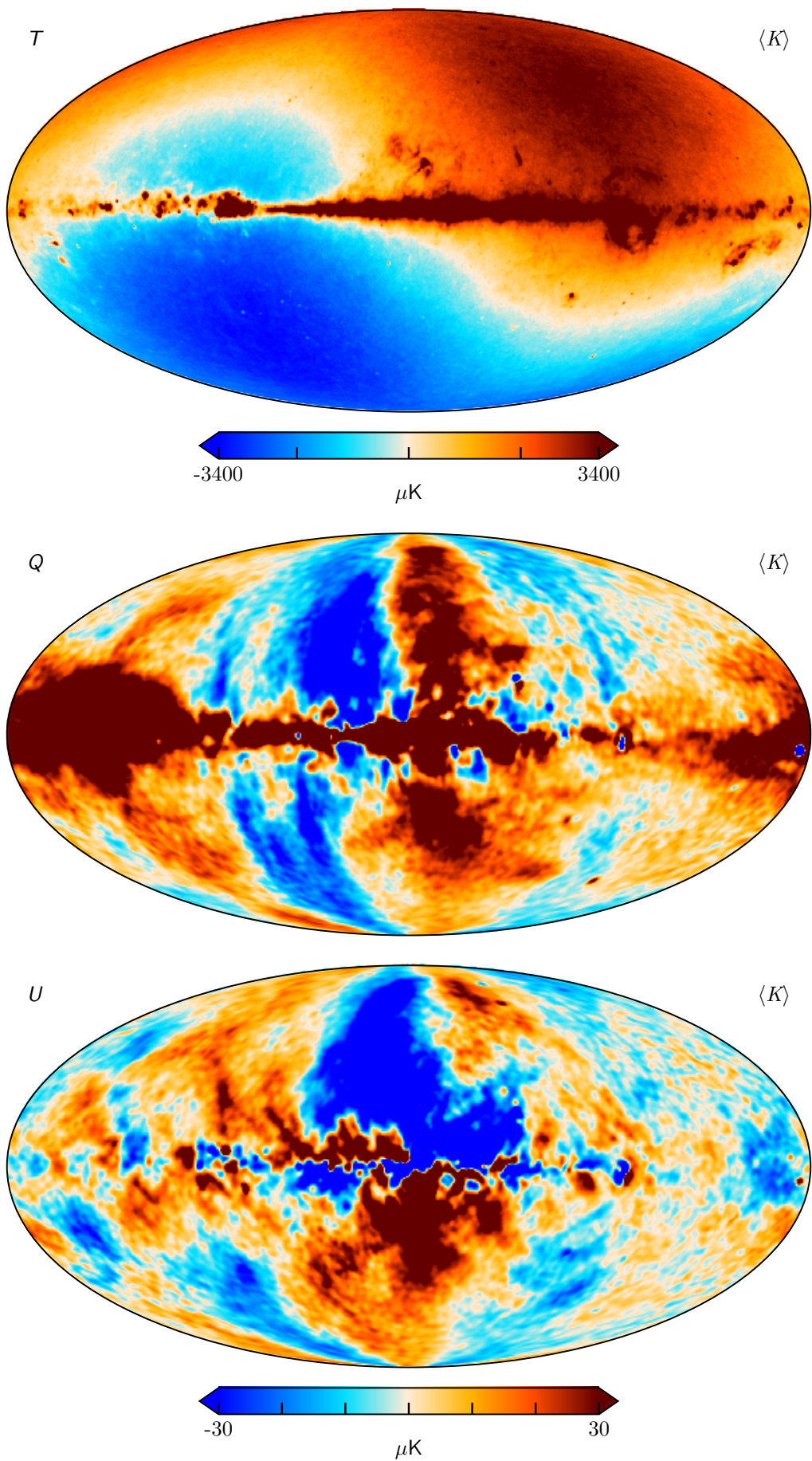


Fig. 9. K -band

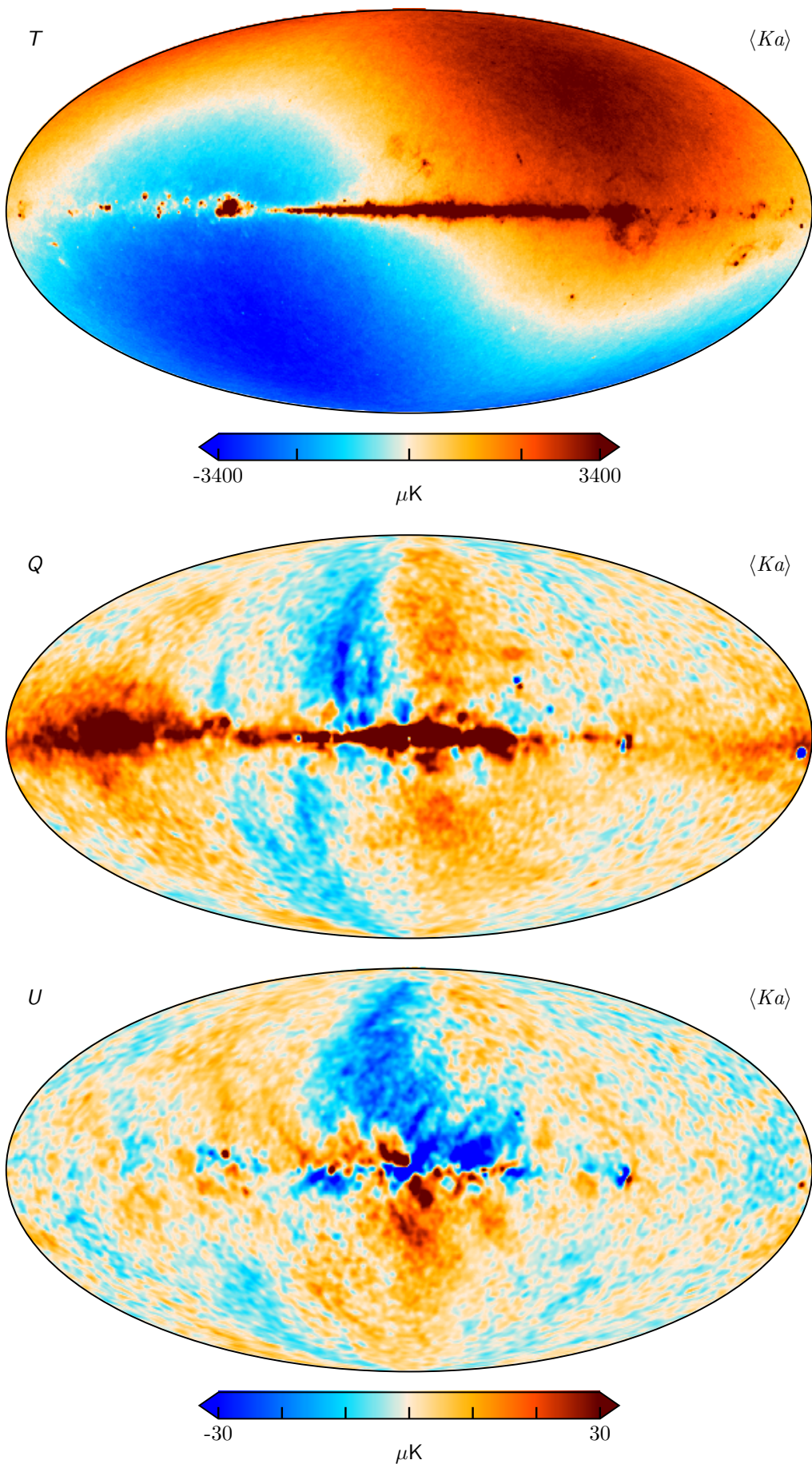


Fig. 10. *Ka*-band

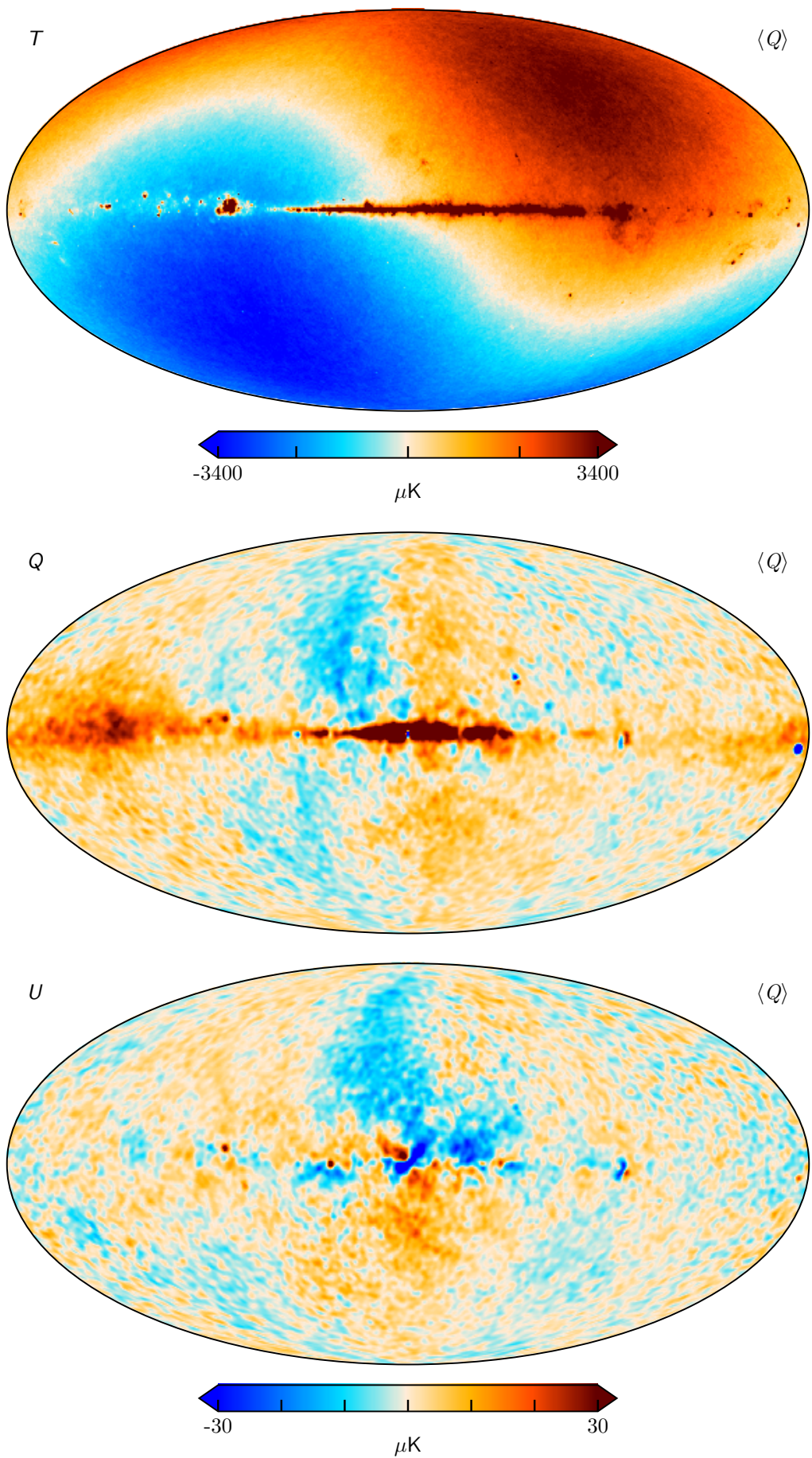


Fig. 11. Q -band

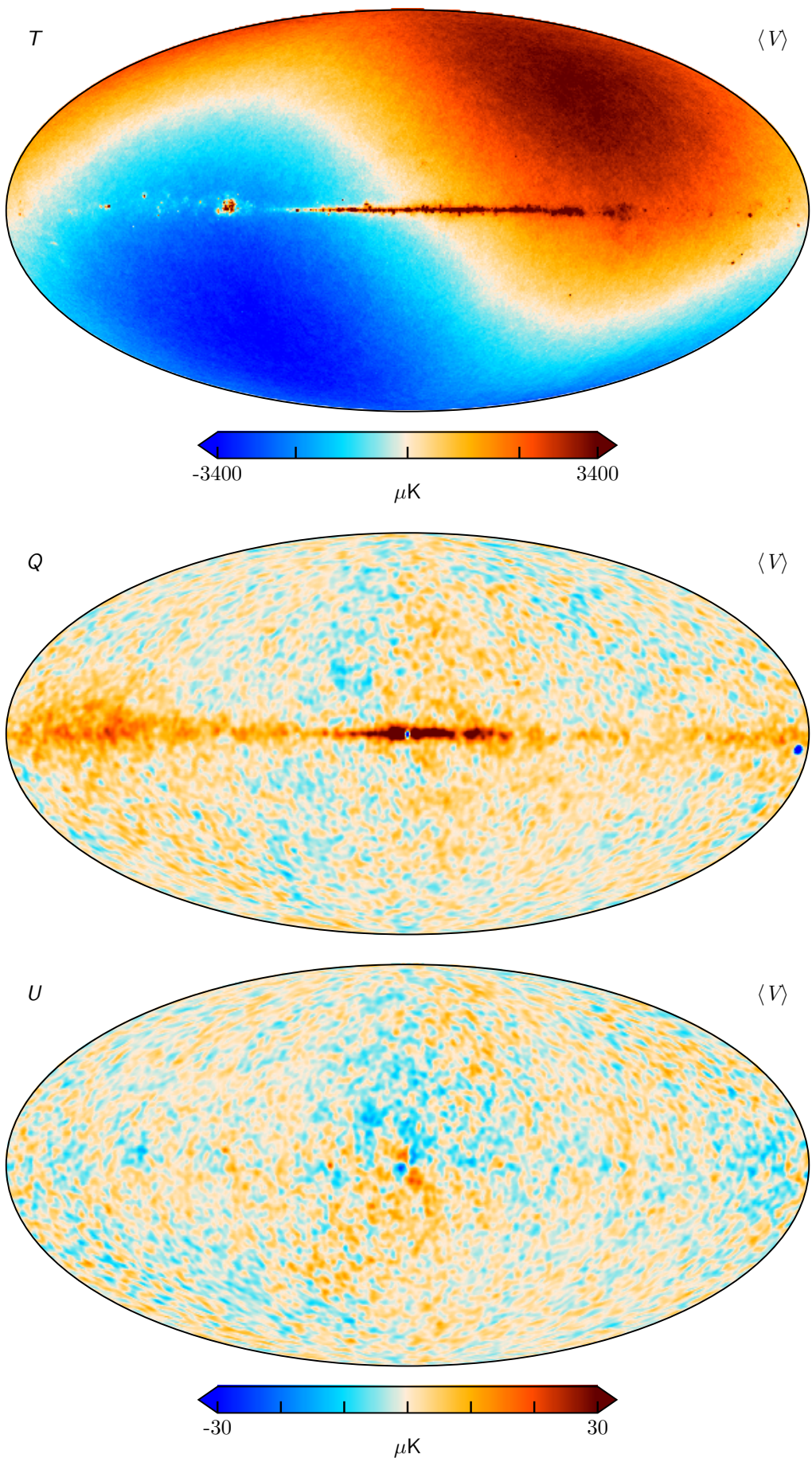


Fig. 12. V-band

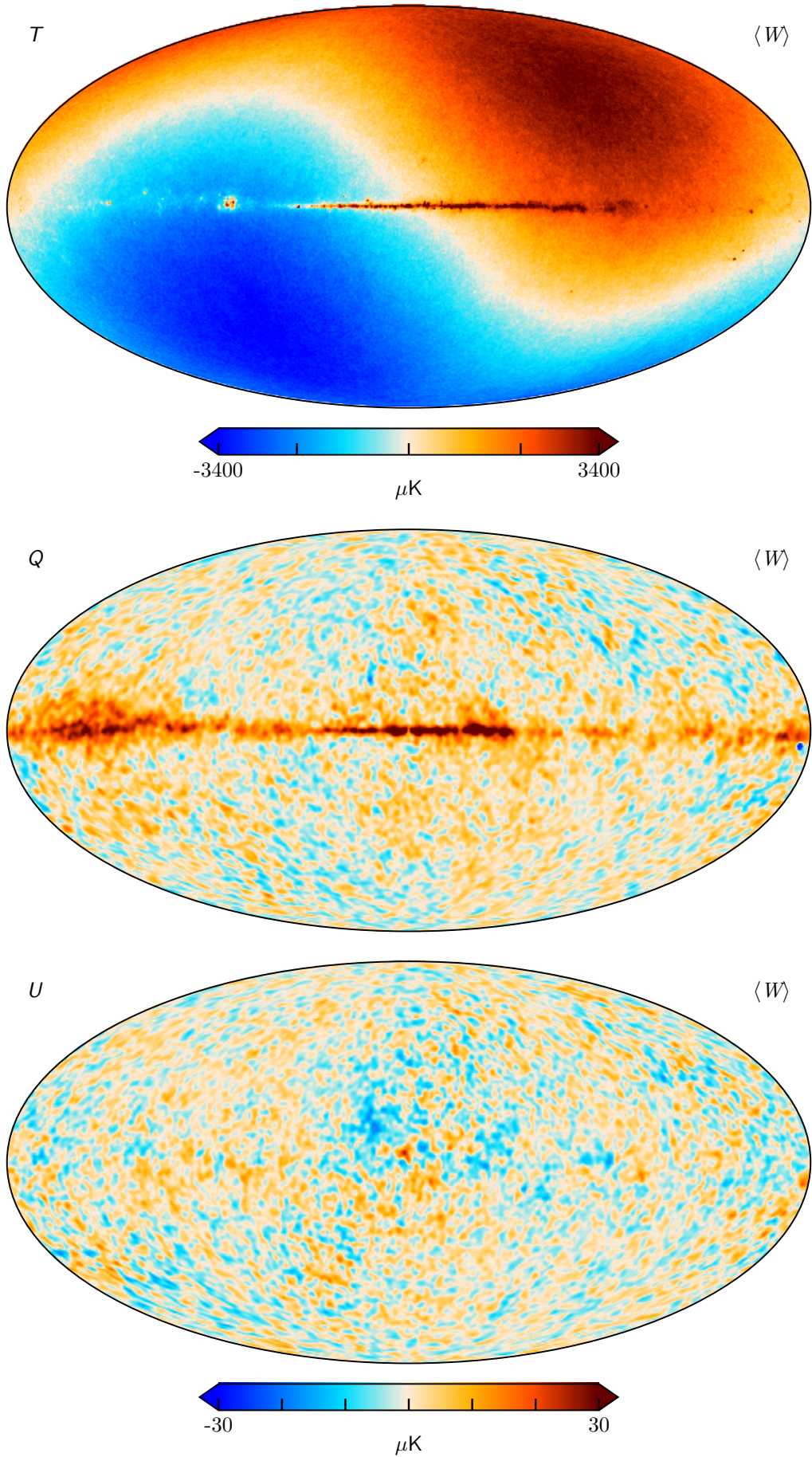
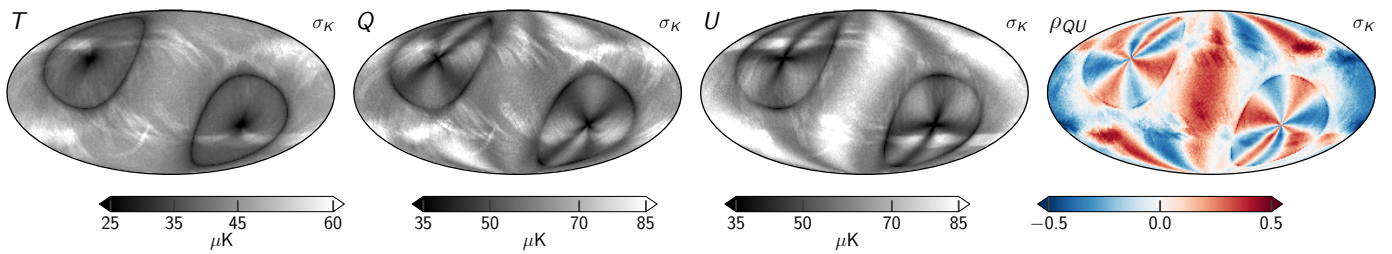
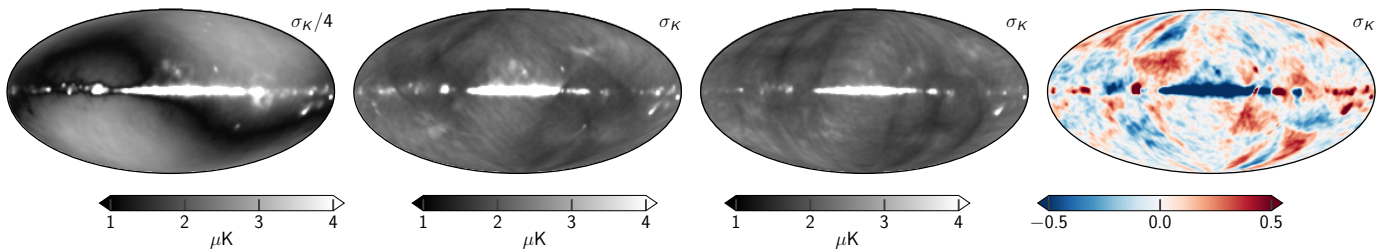
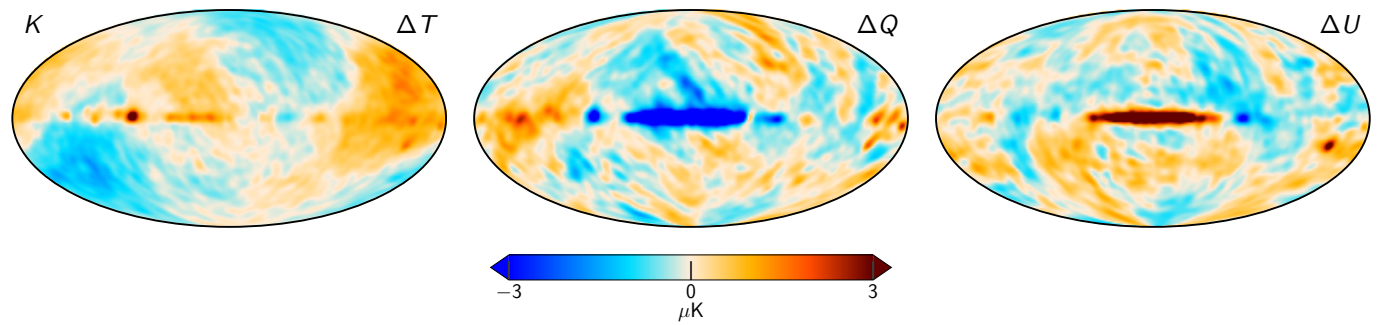
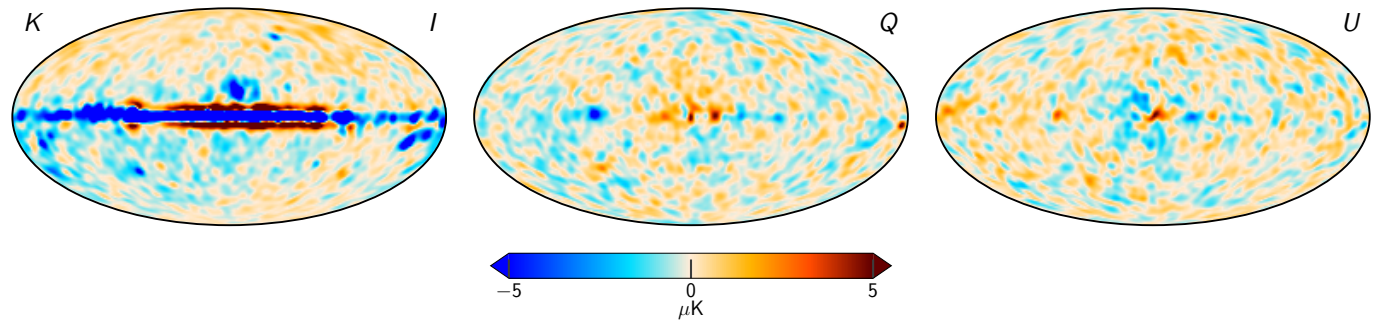
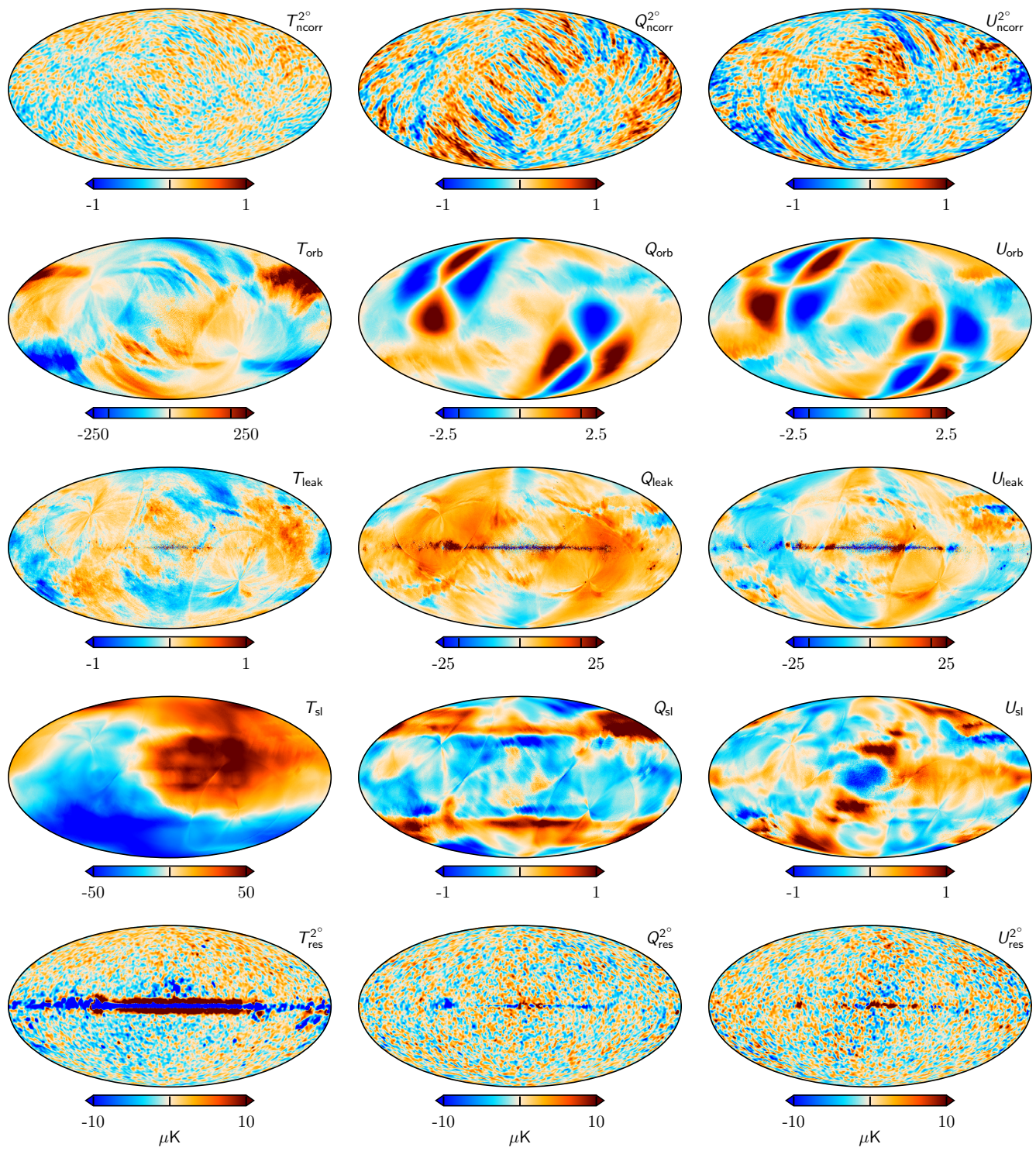


Fig. 13. W -band

**Fig. 14.** RMS**Fig. 15.** Kstd**Fig. 16.** K sample diff**Fig. 17.** K residual

**Fig. 18.** Time-ordered components projected

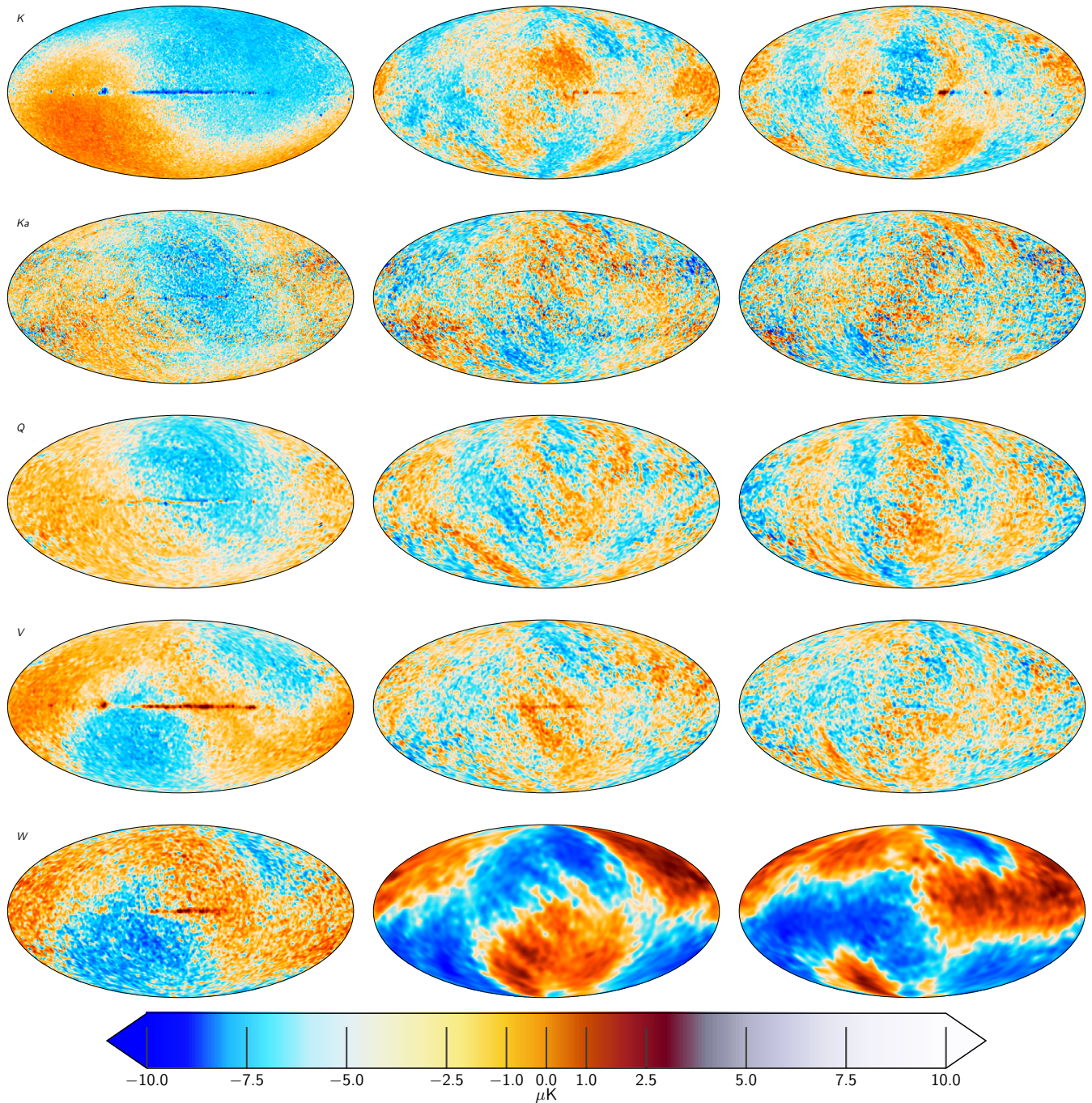
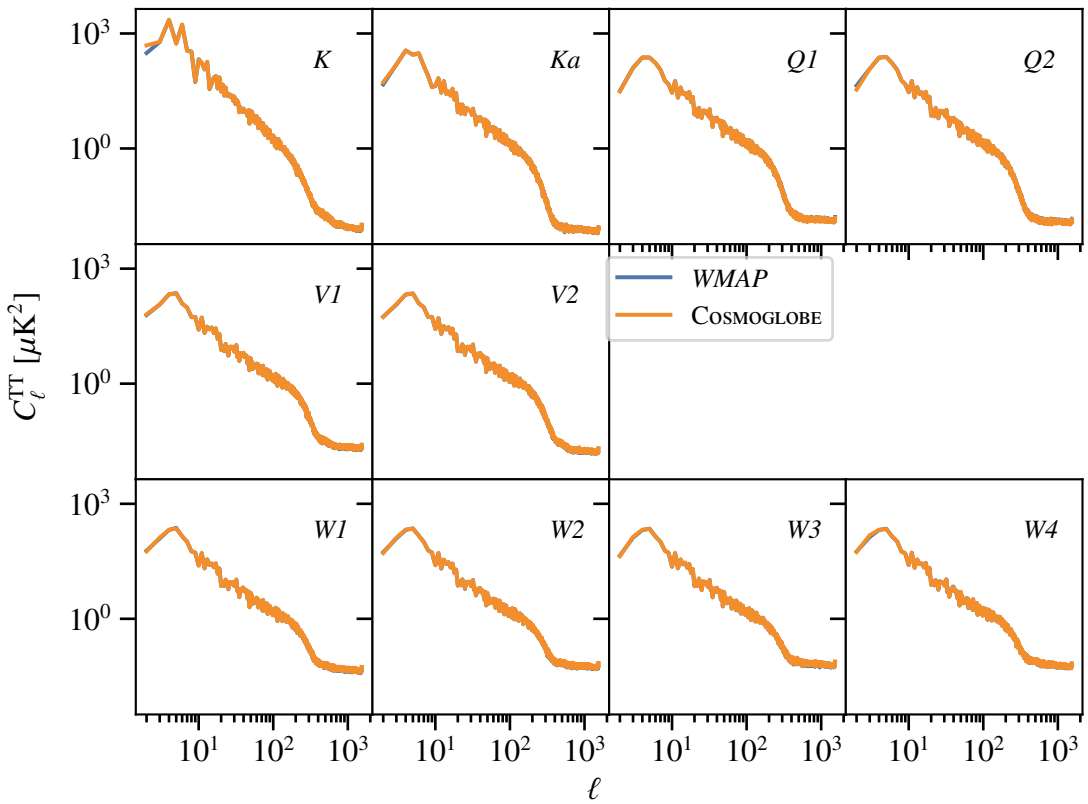
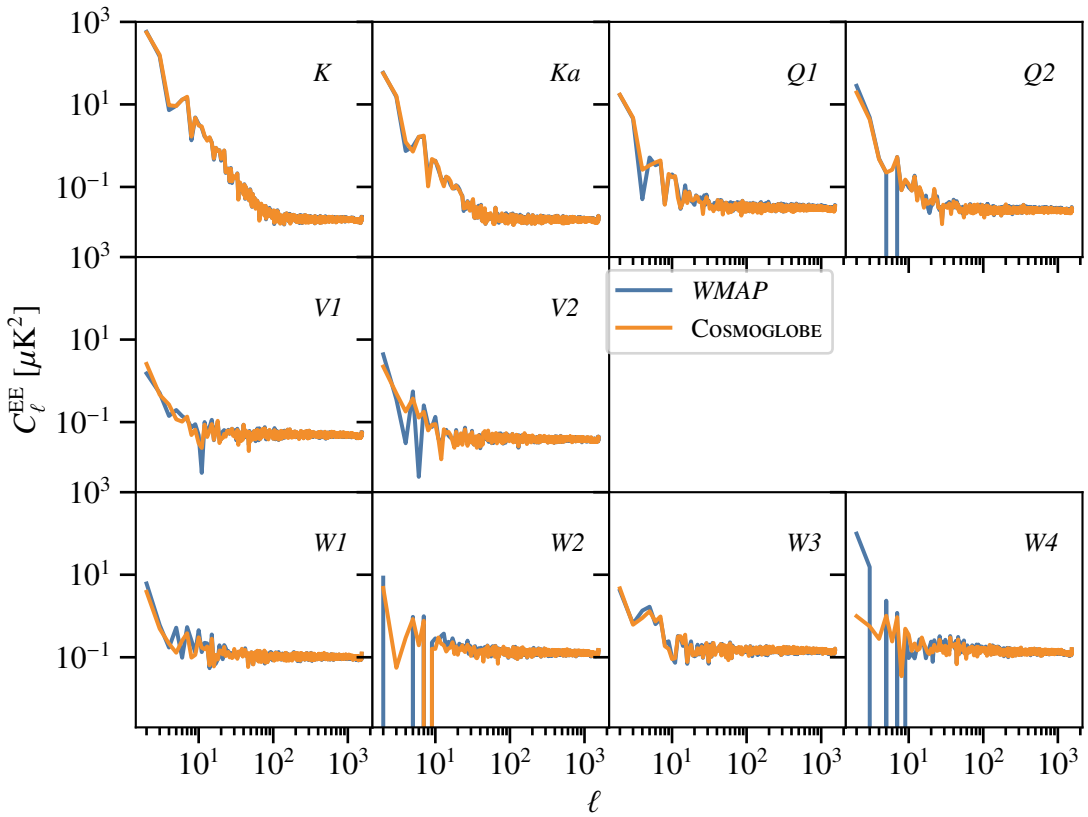
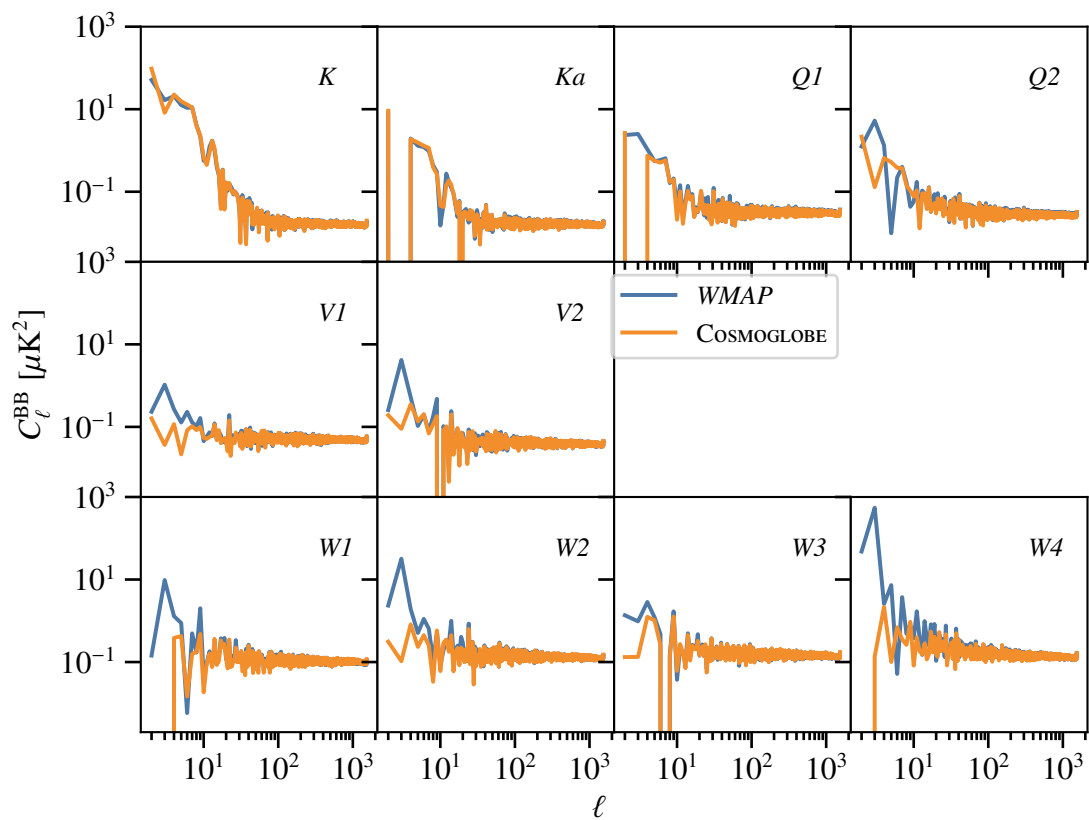
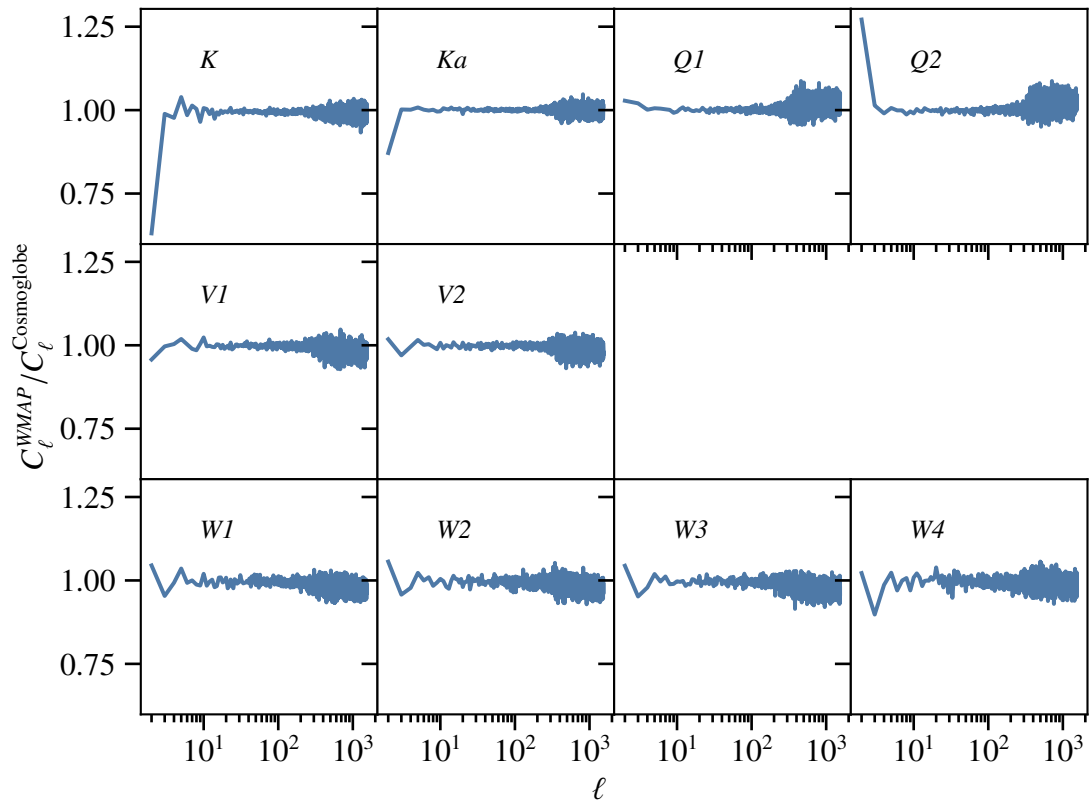


Fig. 19. Difference maps between the COSMOGLobe and 9-year *WMAP* frequency maps. Columns show Stokes T , Q , and U parameter maps, while rows show K -, Ka -, Q -, V -, and W -band maps. The temperature maps are smoothed to an angular resolution of 1° FWHM, while the polarization maps are smoothed to 5° FWHM.

**Fig. 20.** TT power spectra**Fig. 21.** EE power spectra

**Fig. 22.** BB power spectra**Fig. 23.** TT ratios

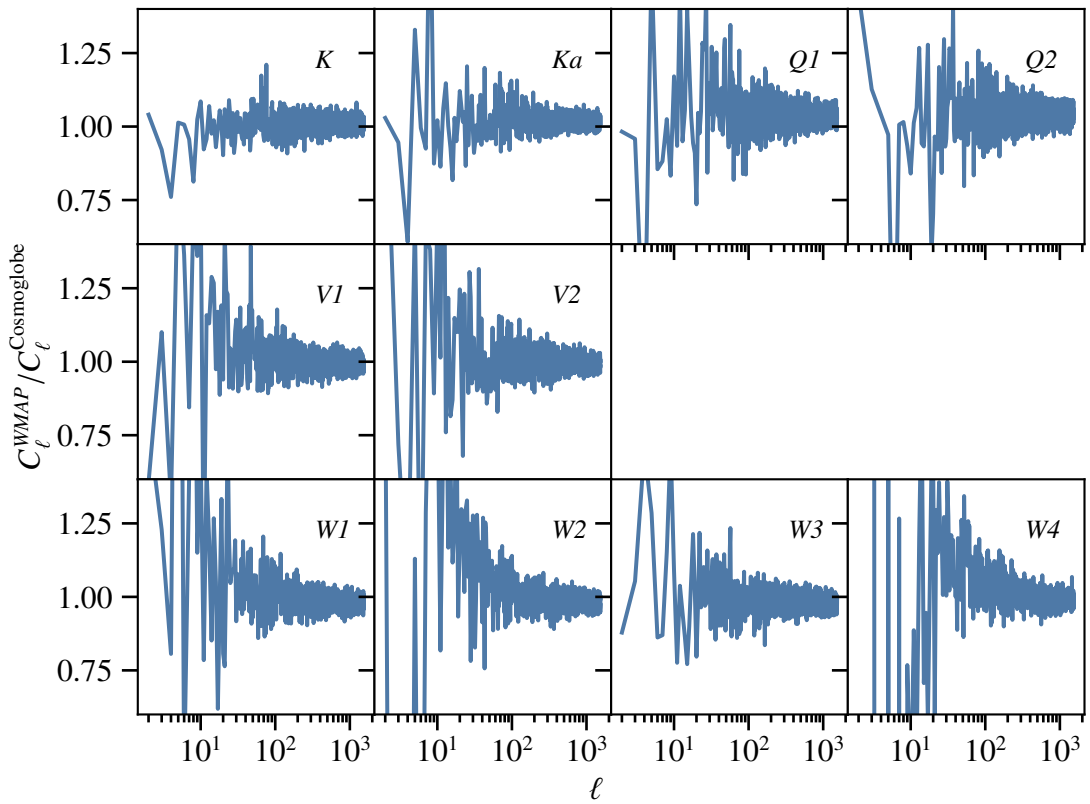
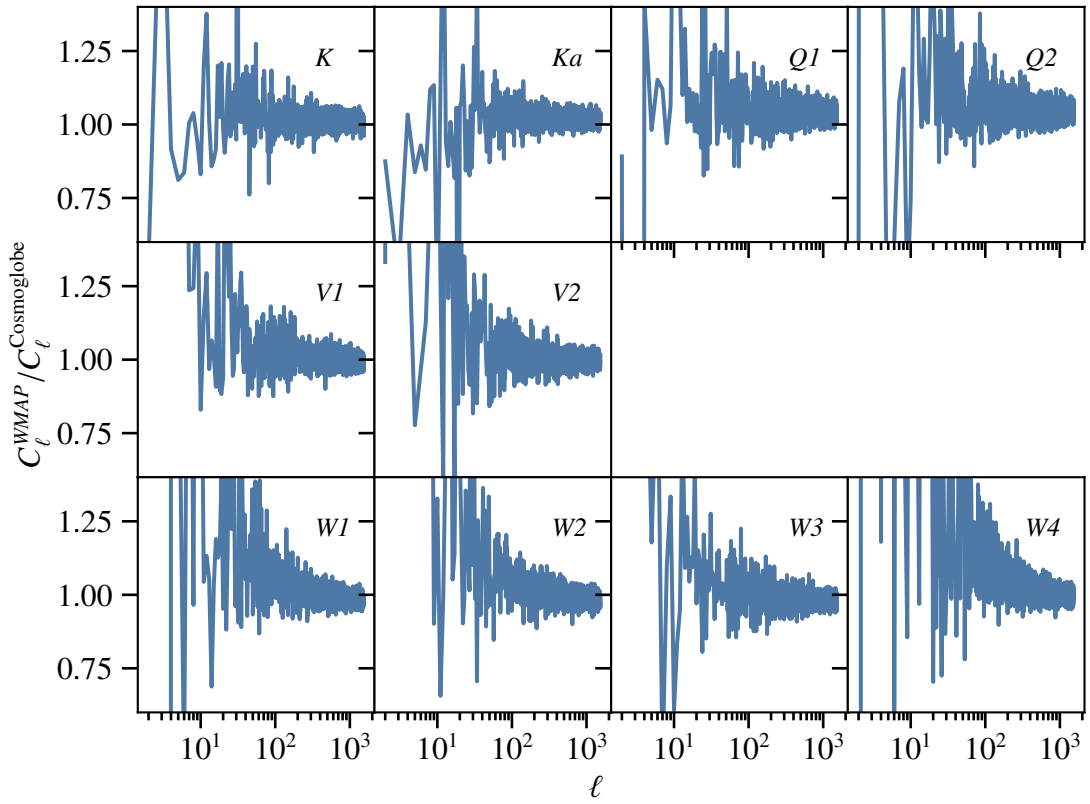
**Fig. 24.** EE ratios**Fig. 25.** BB ratios

Table 7. Difference map χ^2 statistics.

DIFFERENCE	χ^2_{uncorr}	χ^2_{corr}	$\Delta\chi^2$
0.32×K1 – Ka1 . . .	4291	4287	4
Q1 – Q2	4500	4380	120
V1 – V2	4490	4429	61
W1 – W2	4328	4270	68
W3 – W4	4257	4145	112

Want to compare the QU correlation in WMAP and Planck LFI, get a quantitative number. Point out that the polarization solution itself is much better, but the covariance between pixels themselves is much higher. This wasn't an issue for LFI, so we had to take that into account here.

I also want to put a bit here on why the low- ℓ approach needed to be done separately, how correlated noise sampling addresses it, to what extent it's mitigated, etc.

Note that LFI's 30 and 70 GHz QU correlation is ~ 0.1 , whereas 44 GHz is much larger, ~ 0.5 . This discrepancy is due to the number of horns with differing polarization orientation. Both 30 and 70 GHz have an even number of horns, allowing for pairs of datastreams to be combined to give independent polarization measurements. Conversely, 44 GHz has one horn pair and an unpaired horn, the latter of which induces more correlation in the QU observation matrix. An example for Ka and 30 GHz is shown in Fig. ???. Aside from the obvious morphological changes due to the two experiments' different observing strategies, the magnitude of WMAP's correlation is much larger than *Planck*'s.

The BEYONDPLANCK project took this covariance structure into account using the dense $N_{\text{side}} = 16$ noise covariance matrix provided by the WMAP team.¹ Properly sampled correlated noise only leaves white noise in the maps, so the noise properties of each map's sample do not require a dense pixel-pixel covariance, even at low resolution (BeyondPlanck 2022; Basyrov et al. 2022). The WMAP9 inverse noise covariance matrices were computed using the full time-space noise matrix $N = N^w + N^{\text{corr}}$, so the full pixel-pixel covariance matrix $\Sigma^{-1} = P^T N^{-1} P$ took into account the correlation between neighboring samples. The CosMOGLOBE maps, by subtracting a realization of correlated noise before mapmaking, estimates an inverse noise covariance matrix

$$\Sigma_{pp'}^{-1} = \sum_{t_1, t_2} P_{t_1, p_1}^T N_{t_1, t_2}^{-1} P_{t_2, p_2} = \sum_t P_{t, p_1}^T N_{t, t}^{-1} P_{t, p_2} \quad (30)$$

How much off-diagonal pixel covariance is there here?

dense noise covariance matrix also explicitly projected out the poorly-measured imbalance modes, but because we find no trace of these modes in our sky maps or residual maps, this treatment is not necessary in our approach. However, the correlation between Stokes Q and U was not taken into account in the BEYONDPLANCK LFI analysis. This was not a significant oversight in the LFI analysis because the 30 and 70 GHz maps only had a 10% correlation, and 44 GHz's 50% correlation was subdominant to other systematic effects. We have updated Commander3 to take QU correlation into account for LFI.

8.3. Comparison with 9-year WMAP maps

8.4. Consistency within WMAP channels

8.5. Consistency between WMAP and LFI

8.6. Preliminary CMB results

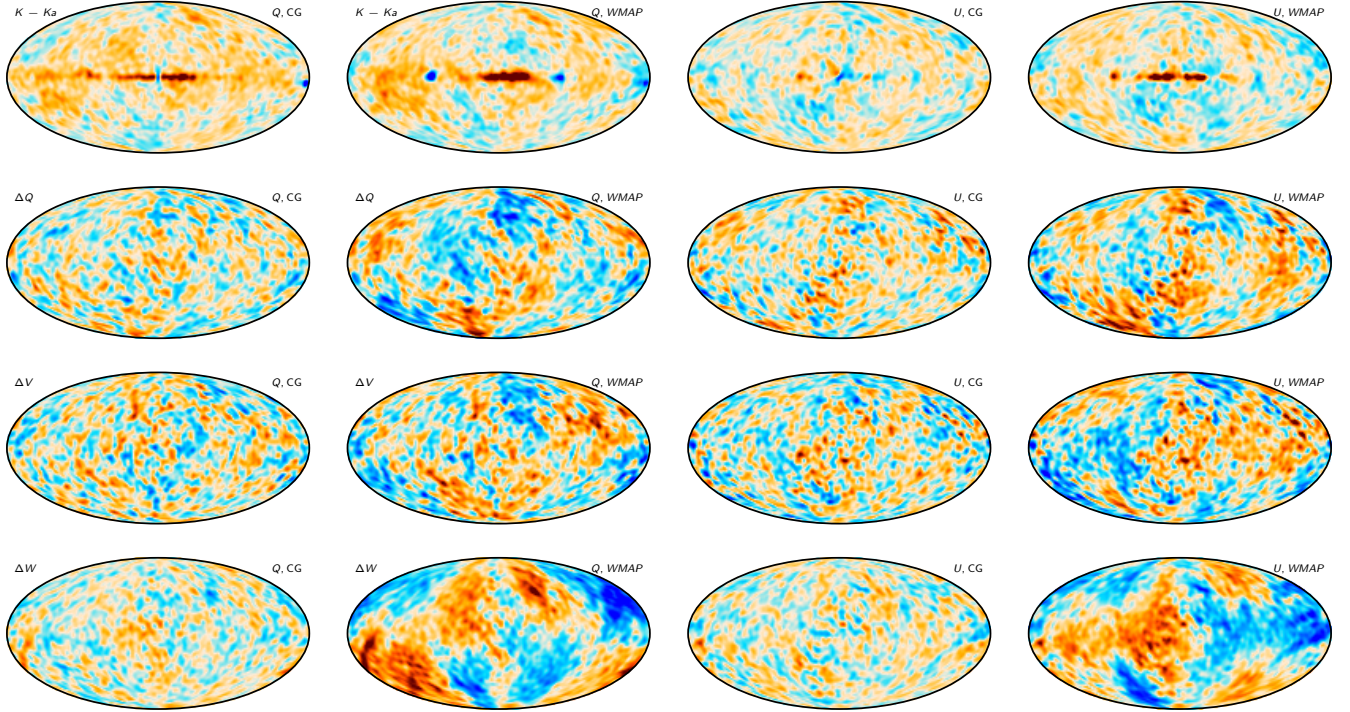
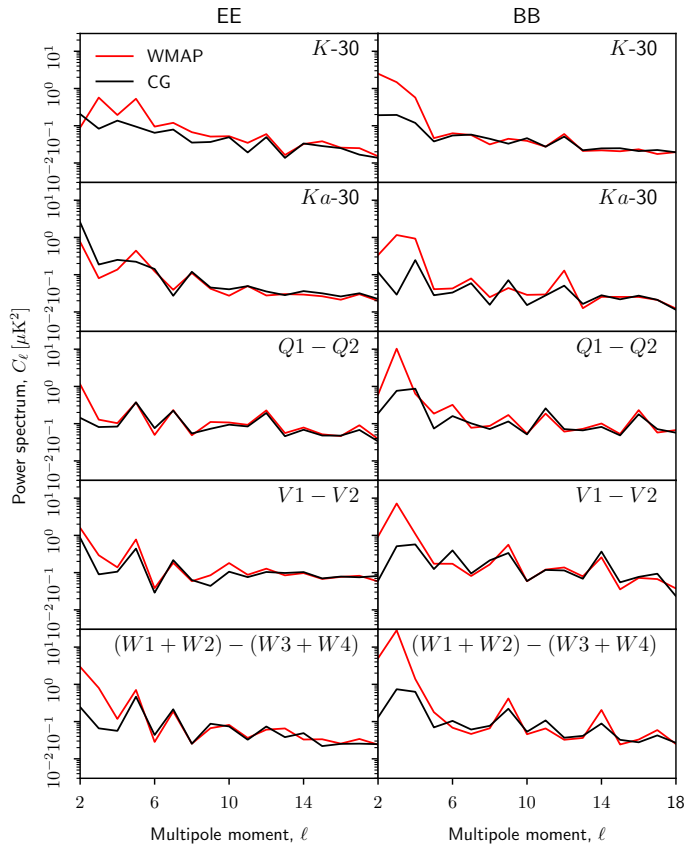
8.6.1. CMB Solar dipole

8.6.2. Temperature power spectrum

8.6.3. Preliminary large-scale CMB polarization results

8.7. Signal-to-noise ratio comparison between WMAP and LFI

¹ https://lambda.gsfc.nasa.gov/product/wmap/dr5/ninv_info.html

**Fig. 26.** Half-difference maps, smoothed by 10° .**Fig. 27.** Half-difference spectra.

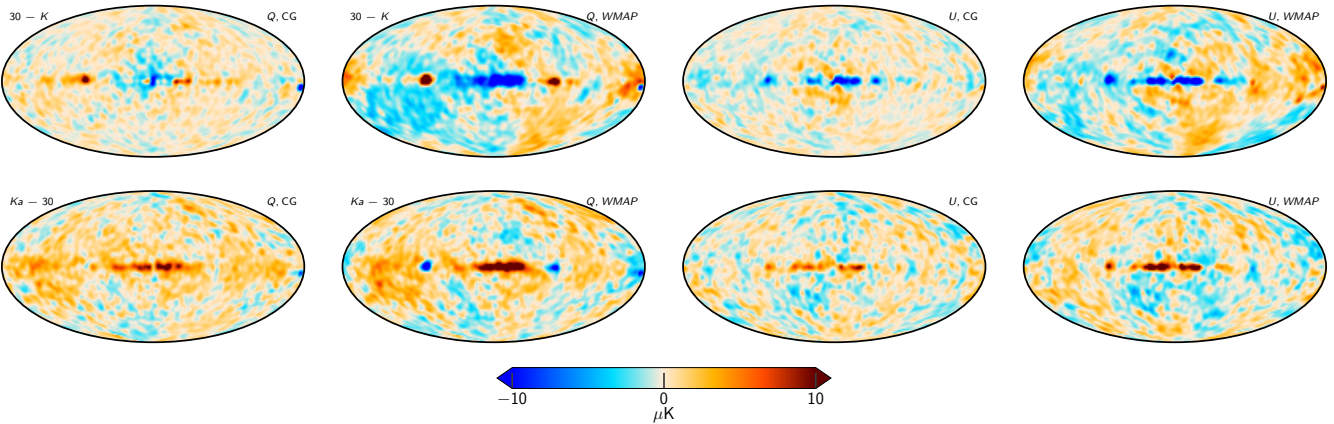


Fig. 28. Mean of WMAP+LFI bands

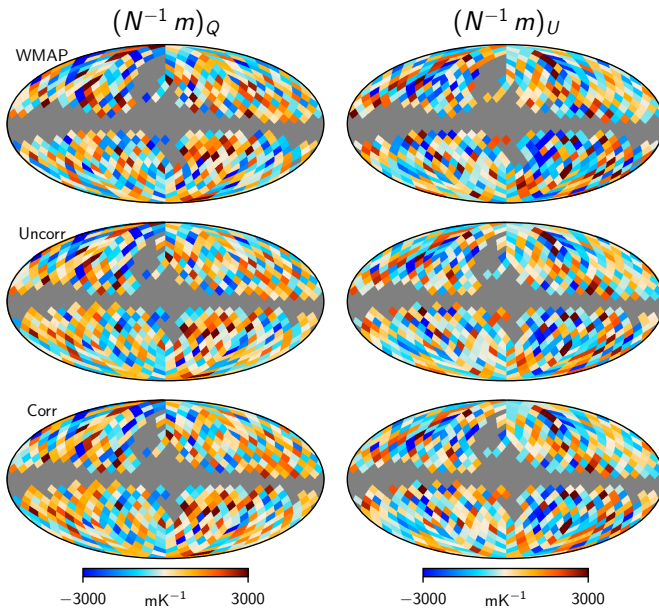


Fig. 29. Noise-weighted likelihood input maps.

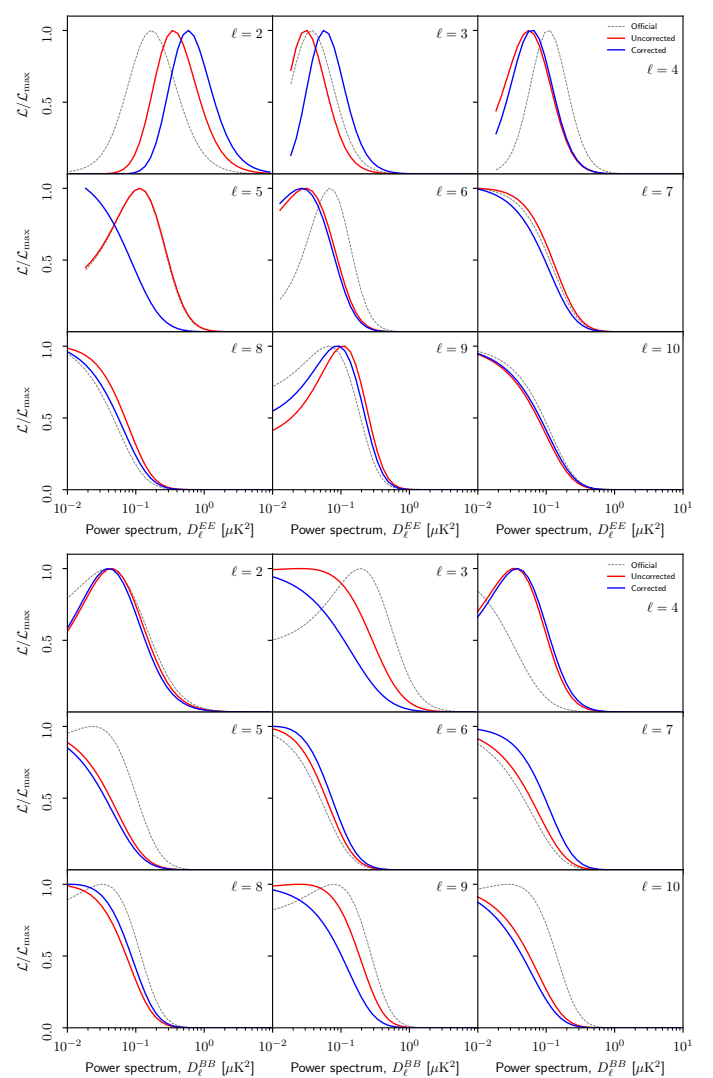


Fig. 30. Likelihood slices

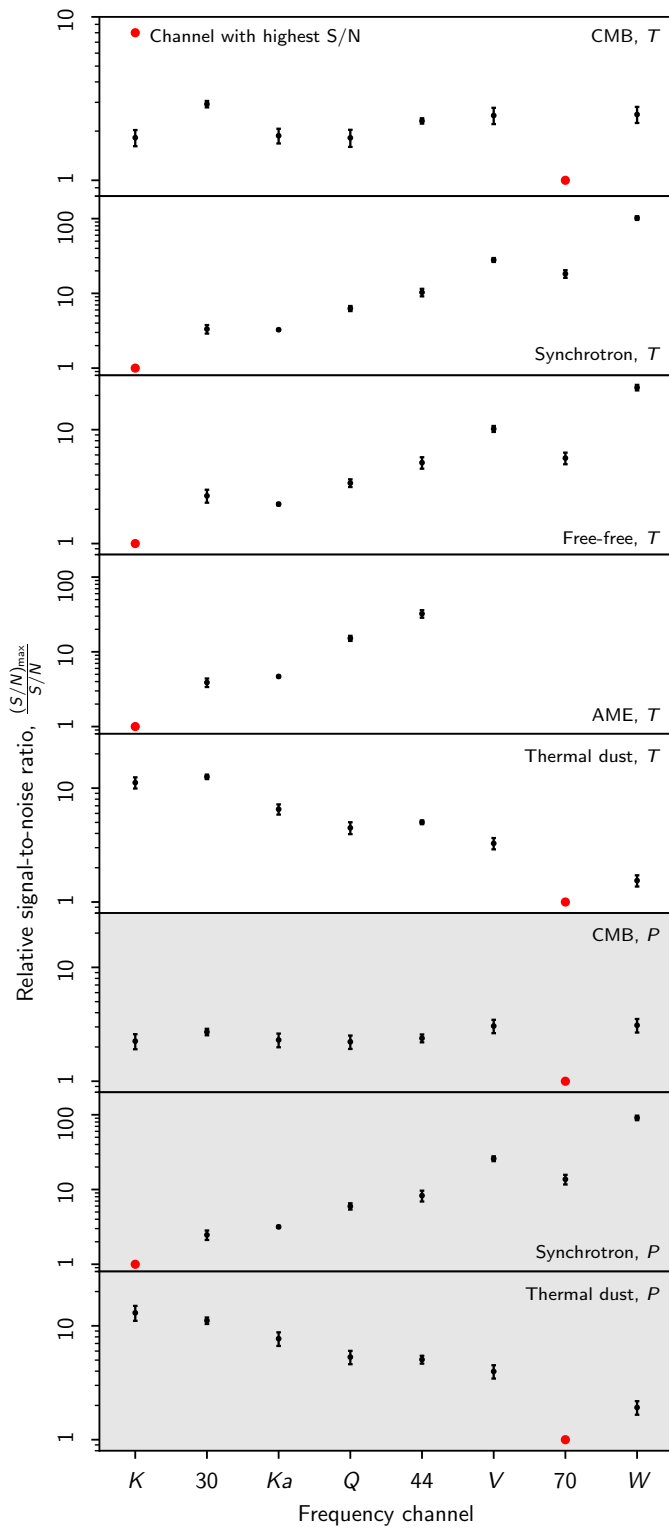


Fig. 31. Relative signal-to-noise ratios for WMAP and LFI channels and various components.

9. Systematic error corrections and uncertainties

9.1. *Sky map corrections*

9.2. *Power spectrum residuals*

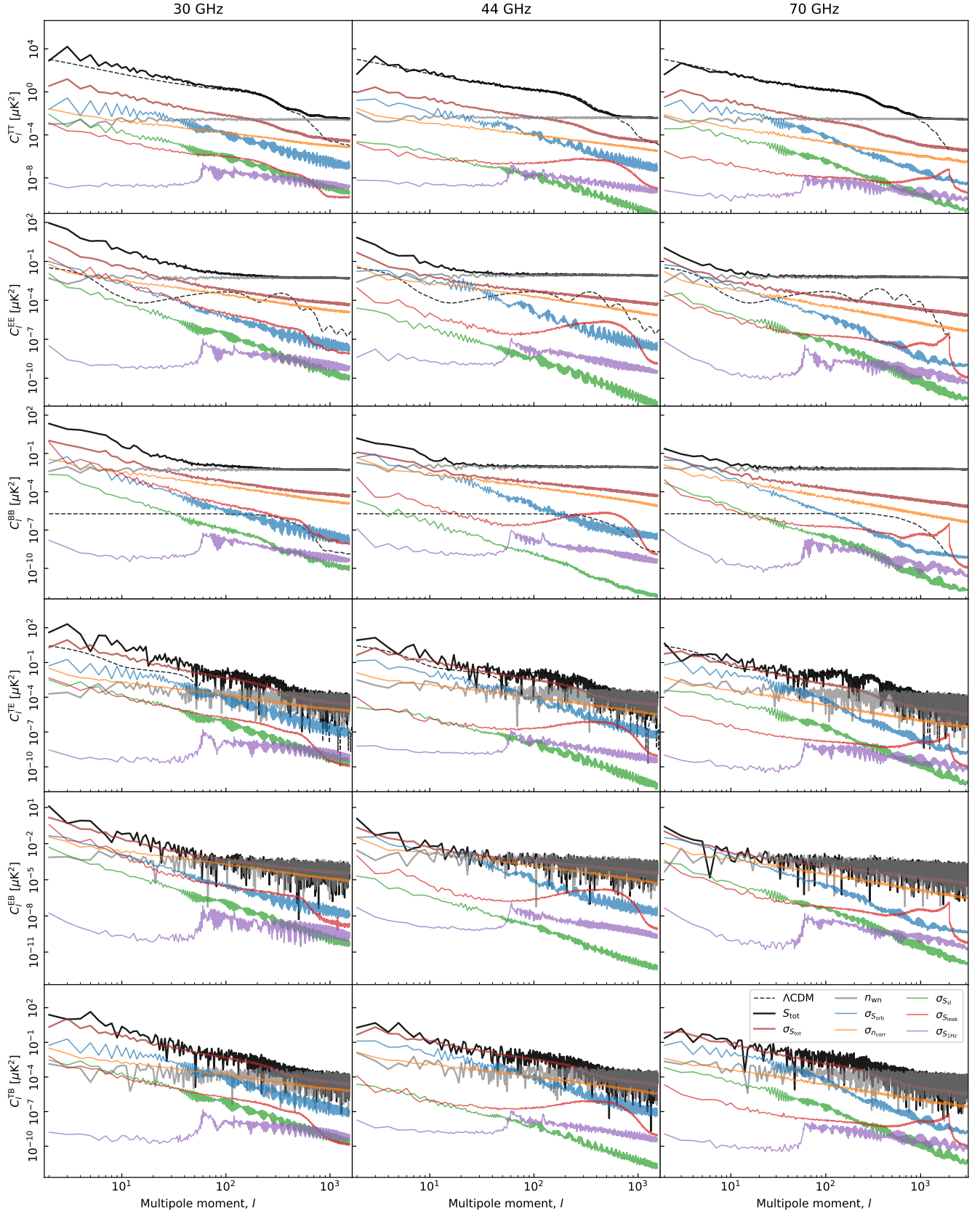


Fig. 32. Pseudo-spectrum standard deviation for each instrumental systematic correction shown in Figs. ??–?? (thin colored lines). For comparison, thick black lines show spectra for the full coadded frequency map; thick red lines show the standard deviation of the same (i.e., the full systematic uncertainty); gray lines show white noise; and dashed black lines show the best-fit *Planck* 2018 Λ CDM power spectrum convolved with the instrument beam. Columns show results for 30, 44 and 70 GHz, respectively, while rows show results for each of the six polarization states (TT, EE, BB, TE, TB, and EB). All spectra have been derived outside the CMB confidence mask presented by [Andersen et al. \(2022\)](#) using the HEALPix *anafast* utility, correcting only for sky fraction and not for mask mode coupling.

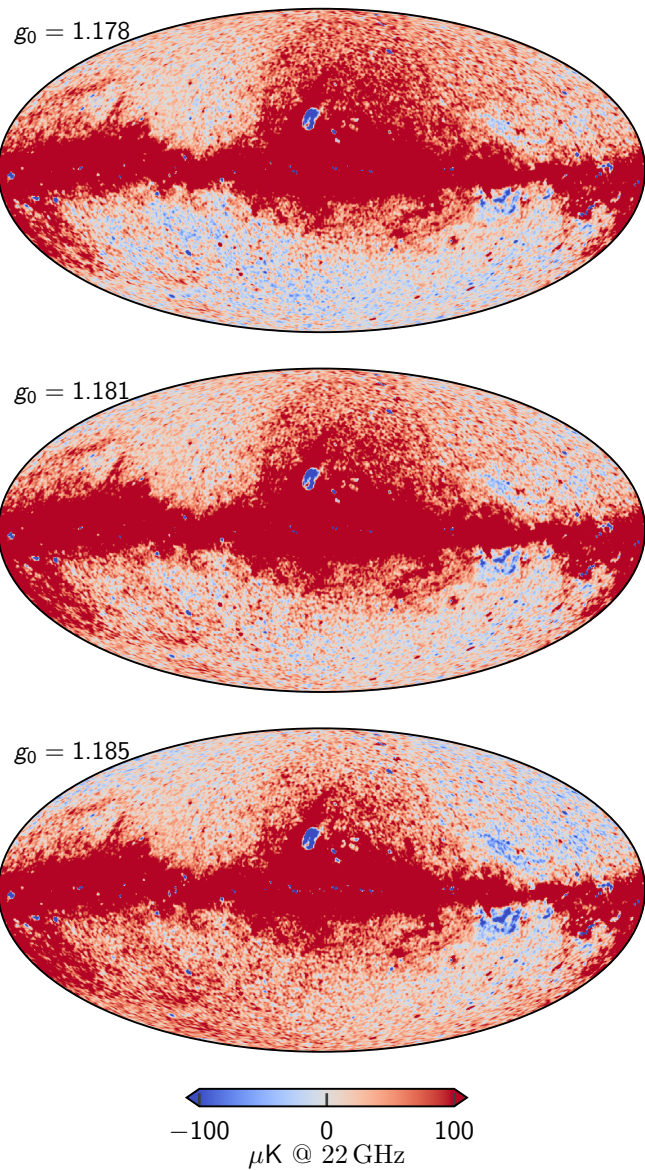


Fig. 33. Dependence on AME amplitude evaluated at 22 GHz as a function of absolute calibration. Each map comes from the fifth iteration of a dedicated *Commander* run that fixed g_0 while letting all other TOD parameters be fit. The values of $g_0 = 1.178$ and $g_0 = 1.185$ represent 3.5σ draws from the prior distribution with mean 1.1815 and standard deviation 0.001. The dipole visible in the top and bottom panels is aligned perfectly with the Solar dipole, and is directly due to variations in the K -band absolute calibration.

10. Outstanding issues

- 10.1. Noise modelling
- 10.2. V -band quadrupole residual
- 10.3. Degeneracy between K -band calibration and AME dipole
- 10.4. Other minor effects
 - 10.4.1. Time-variable bandpass modelling
 - 10.4.2. Polarized sidelobe modelling

11. Conclusions

References

- Ali-Haïmoud, Y. 2010, Astrophysics Source Code Library [ascl:1010.016]
- Ali-Haïmoud, Y., Hirata, C. M., & Dickinson, C. 2009, MNRAS, 395, 1055
- Andersen et al. 2022, A&A, in press [arXiv:2201.08188]
- Basyrov et al. 2022, A&A, submitted [arXiv:2208.14293]
- Bennett, C. L., Bay, M., Halpern, M., et al. 2003a, ApJ, 583, 1
- Bennett, C. L., Halpern, M., Hinshaw, G., et al. 2003b, ApJS, 148, 1
- Bennett, C. L., Larson, D., Weiland, J. L., et al. 2013, ApJS, 208, 20
- BeyondPlanck. 2022, A&A, submitted [arXiv:2011.05609]
- Colombo et al. 2022, A&A, submitted [arXiv:2208.14276]
- de la Hoz, E., Barreiro, R. B., Vielva, P., et al. 2023, MNRAS, 519, 3504
- Dicke, R. H., Peebles, P. J. E., Roll, P. G., & Wilkinson, D. T. 1965, ApJ, 142, 414
- Eriksen, H. K., Dickinson, C., Lawrence, C. R., et al. 2006, ApJ, 641, 665
- Eriksen, H. K., Jewell, J. B., Dickinson, C., et al. 2008, ApJ, 676, 10
- Eriksen, H. K., O'Dwyer, I. J., Jewell, J. B., et al. 2004, ApJS, 155, 227
- Frigo, M. & Johnson, S. G. 2005, Proceedings of the IEEE, 93, 216, special issue on "Program Generation, Optimization, and Platform Adaptation"
- Galloway et al. 2022, A&A, in press [arXiv:2201.03509]
- Gjerløw et al. 2022, A&A, submitted [arXiv:2011.08082]
- Greason, M. R., Limon, M., Wollack, E., et al. 2012, Nine-Year Explanatory Supplement, 5th edn., Greenbelt, MD: NASA/GSFC
- Haslam, C. G. T., Salter, C. J., Stoffel, H., & Wilson, W. E. 1982, A&AS, 47, 1
- Hinshaw, G., Barnes, C., Bennett, C. L., et al. 2003, ApJS, 148, 63
- Hinshaw, G., Nolta, M. R., Bennett, C. L., et al. 2007, ApJS, 170, 288
- Hinshaw, G., Weiland, J. L., Hill, R. S., et al. 2009, ApJS, 180, 225
- Hu, W., Fukugita, M., Zaldarriaga, M., & Tegmark, M. 2001, ApJ, 549, 669
- Ihle et al. 2022, A&A, in press [arXiv:2011.06650]
- Jarosik, N., Barnes, C., Bennett, C. L., et al. 2003a, ApJS, 148, 29
- Jarosik, N., Barnes, C., Greason, M. R., et al. 2007, ApJS, 170, 263
- Jarosik, N., Bennett, C. L., Halpern, M., et al. 2003b, ApJS, 145, 413
- Jewell, J., Levin, S., & Anderson, C. H. 2004, ApJ, 609, 1
- Lange, A. E., Ade, P. A., Bock, J. J., et al. 2001, Phys. Rev. D, 63, 042001
- Mather, J. C., Cheng, E. S., Cottingham, D. A., et al. 1994, ApJ, 420, 439
- Mather, J. C., Fixsen, D. J., Shafer, R. A., Mosier, C., & Wilkinson, D. T. 1999, ApJ, 512, 511
- Penzias, A. A. & Wilson, R. W. 1965, ApJ, 142, 419
- Planck Collaboration X. 2016, A&A, 594, A10
- Remazeilles, M., Dickinson, C., Banday, A. J., Bigot-Sazy, M.-A., & Ghosh, T. 2015, MNRAS, 451, 4311
- Rubiño-Martín, J. A., Guidi, F., Génova-Santos, R. T., et al. 2023, MNRAS, 519, 3383
- Silsbee, K., Ali-Haïmoud, Y., & Hirata, C. M. 2011, MNRAS, 411, 2750
- Smoot, G. F., Bennett, C. L., Kogut, A., et al. 1992, ApJ, 396, L1
- Svalheim et al. 2022, A&A, in press [arXiv:2011.08503]
- Watts et al. 2022, A&A, in press [arXiv:2202.11979]

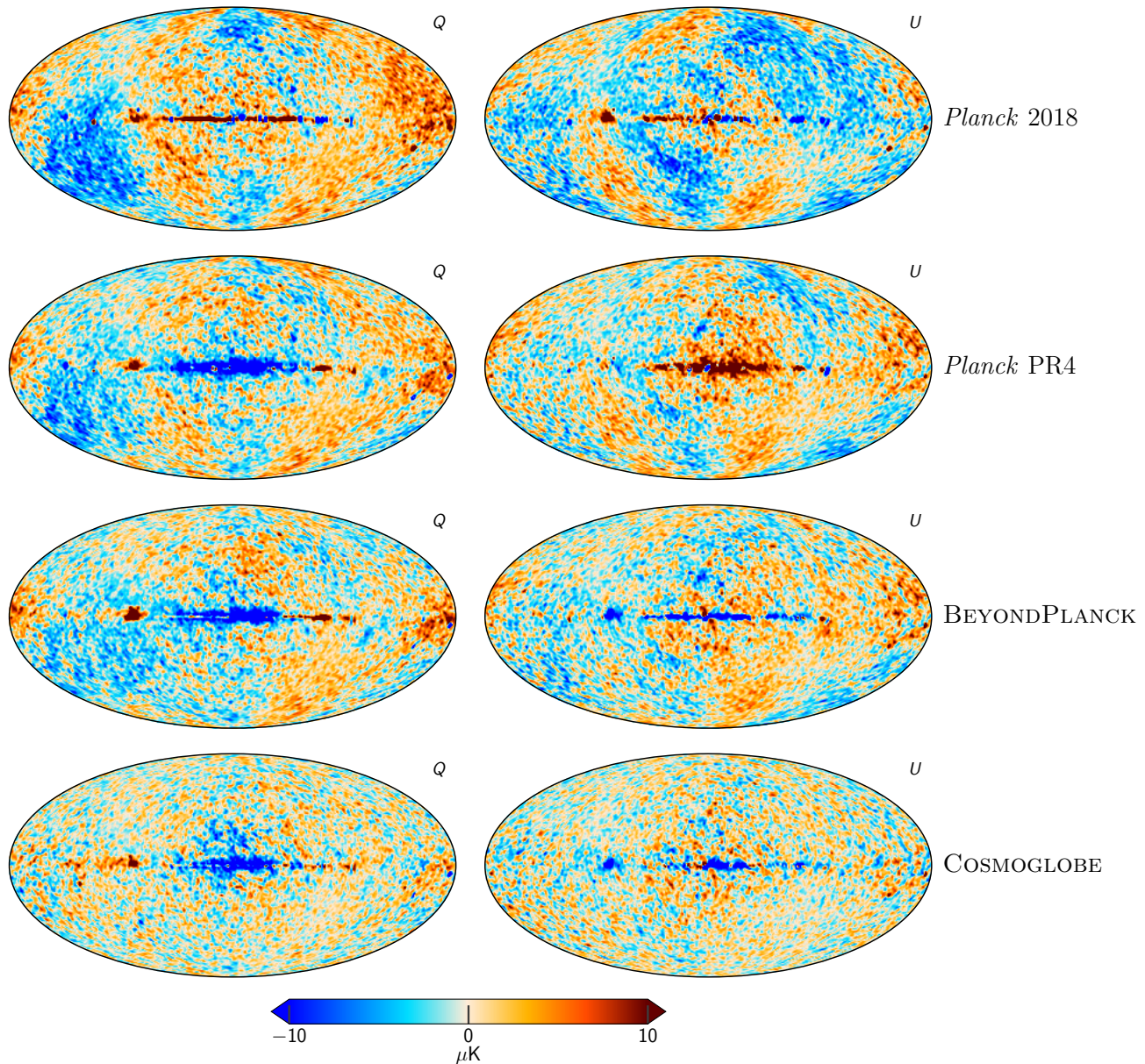


Fig. 34. Difference maps between the *Planck* 30 GHz and WMAP *K*-band maps. The columns are (1) *Planck* 2018 v. WMAP9, (2) *Planck* PR4 v. WMAP9, (3) BEYONDPLANCK v. WMAP9, and (4) COSMOGLOBE *Planck* 30 GHz and WMAP *K*-band both produced in this paper. All maps have been smoothed to a common resolution of 2° FWHM, and the *K*-band map has been scaled by 0.495 to account for different central frequencies, assuming a synchrotron spectral index $\beta_s = -3.1$.

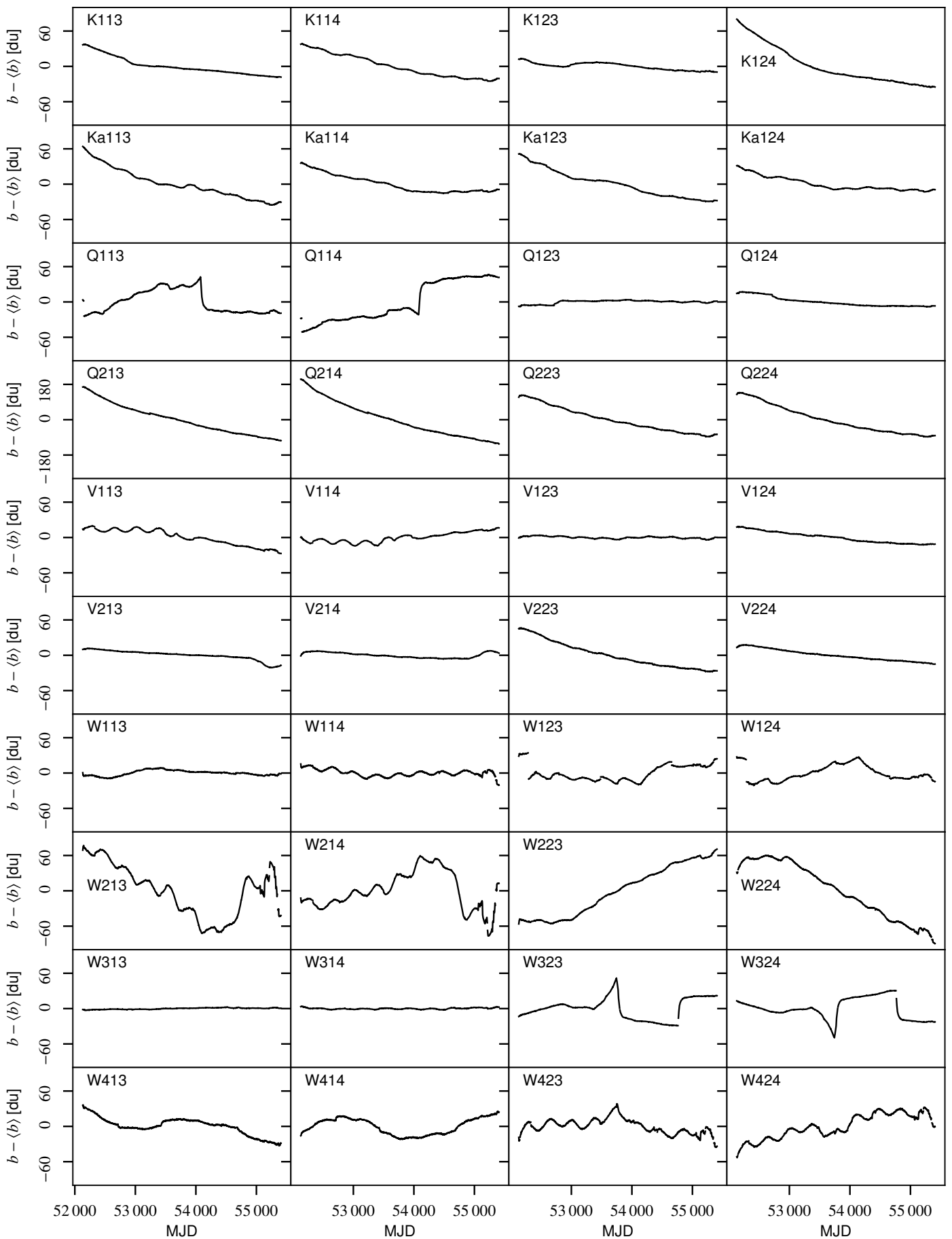
Appendix A: Survey of instrumental parameters

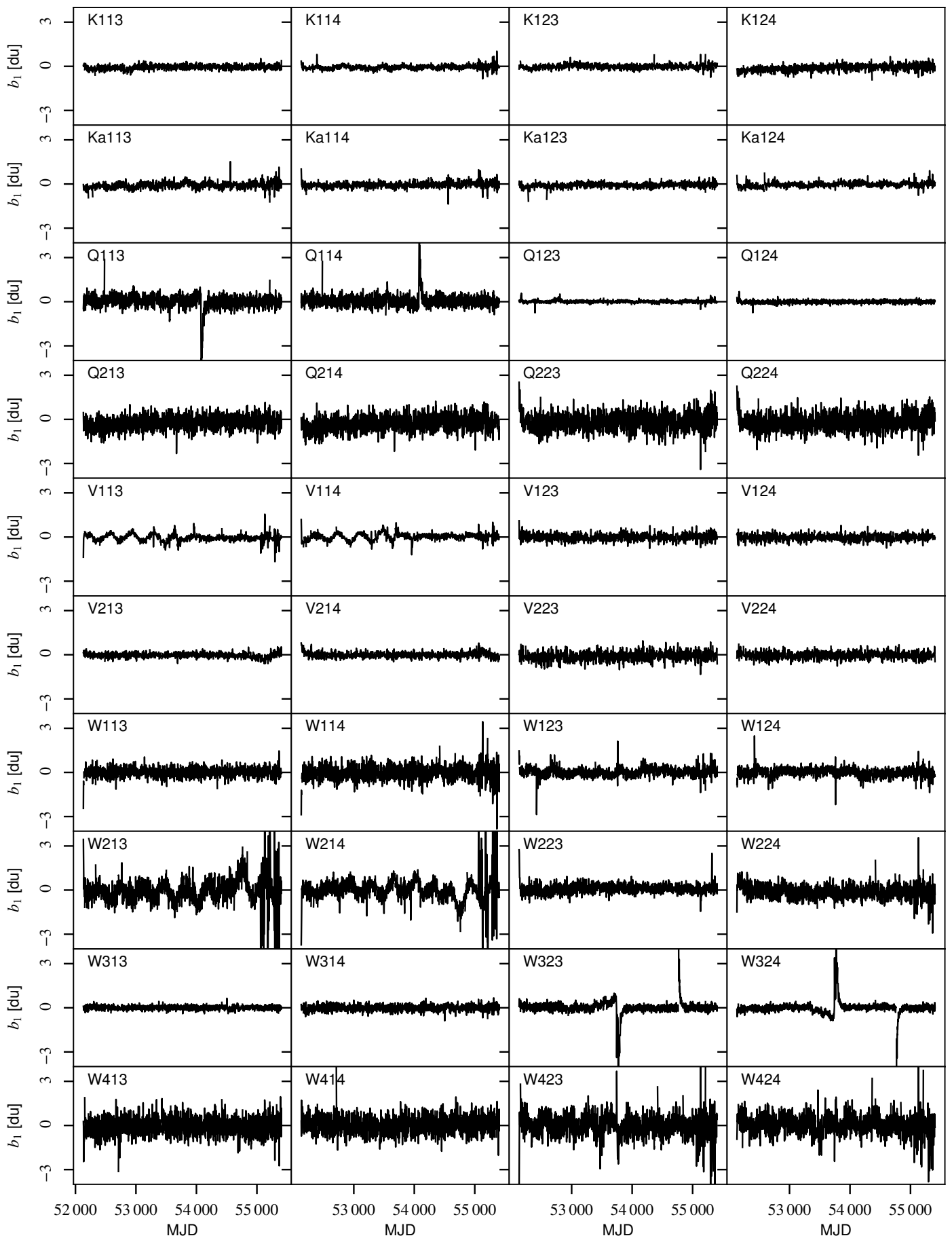
Appendix A.1: Gain, baselines, noise and χ^2

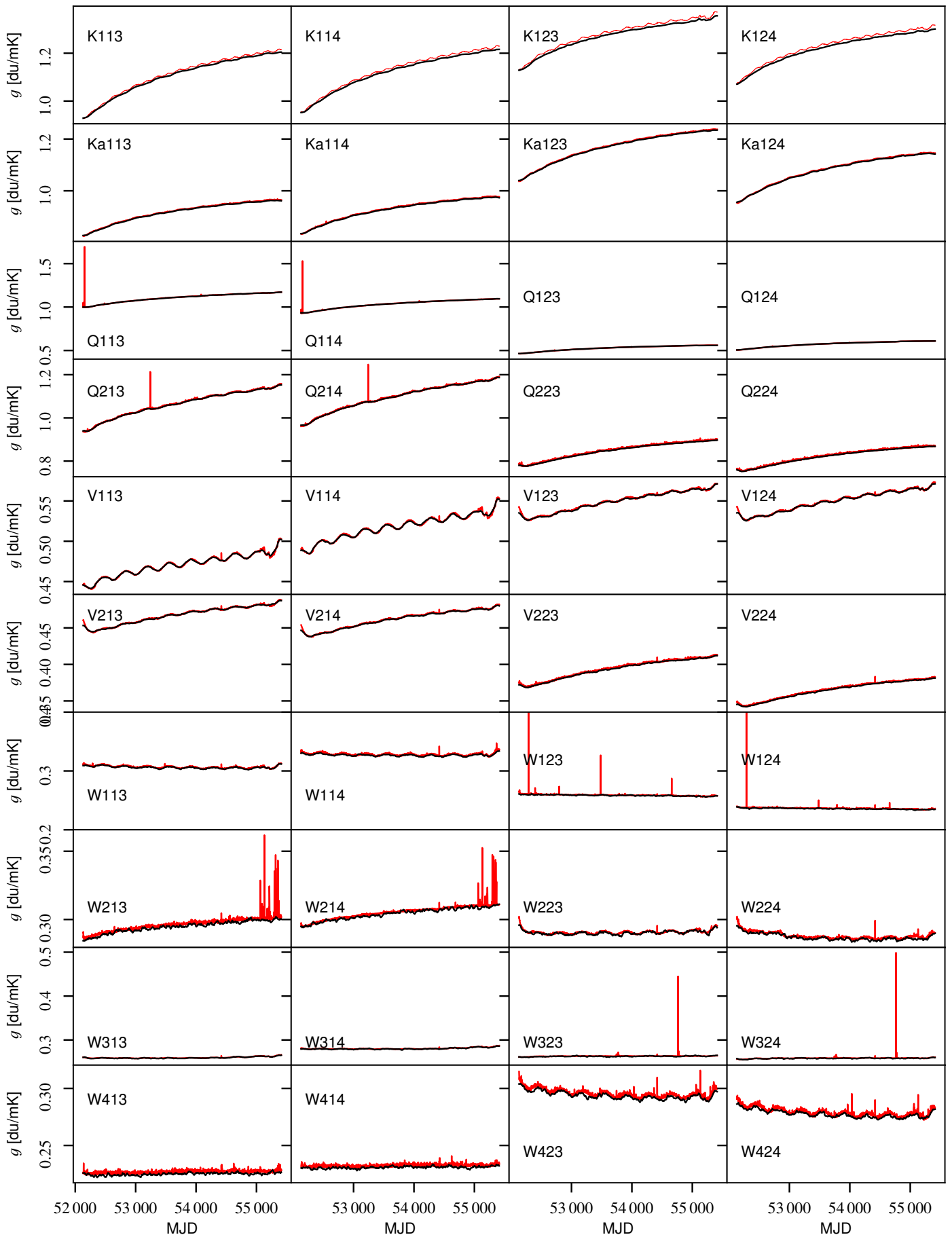
Appendix A.2: Transmission imbalance

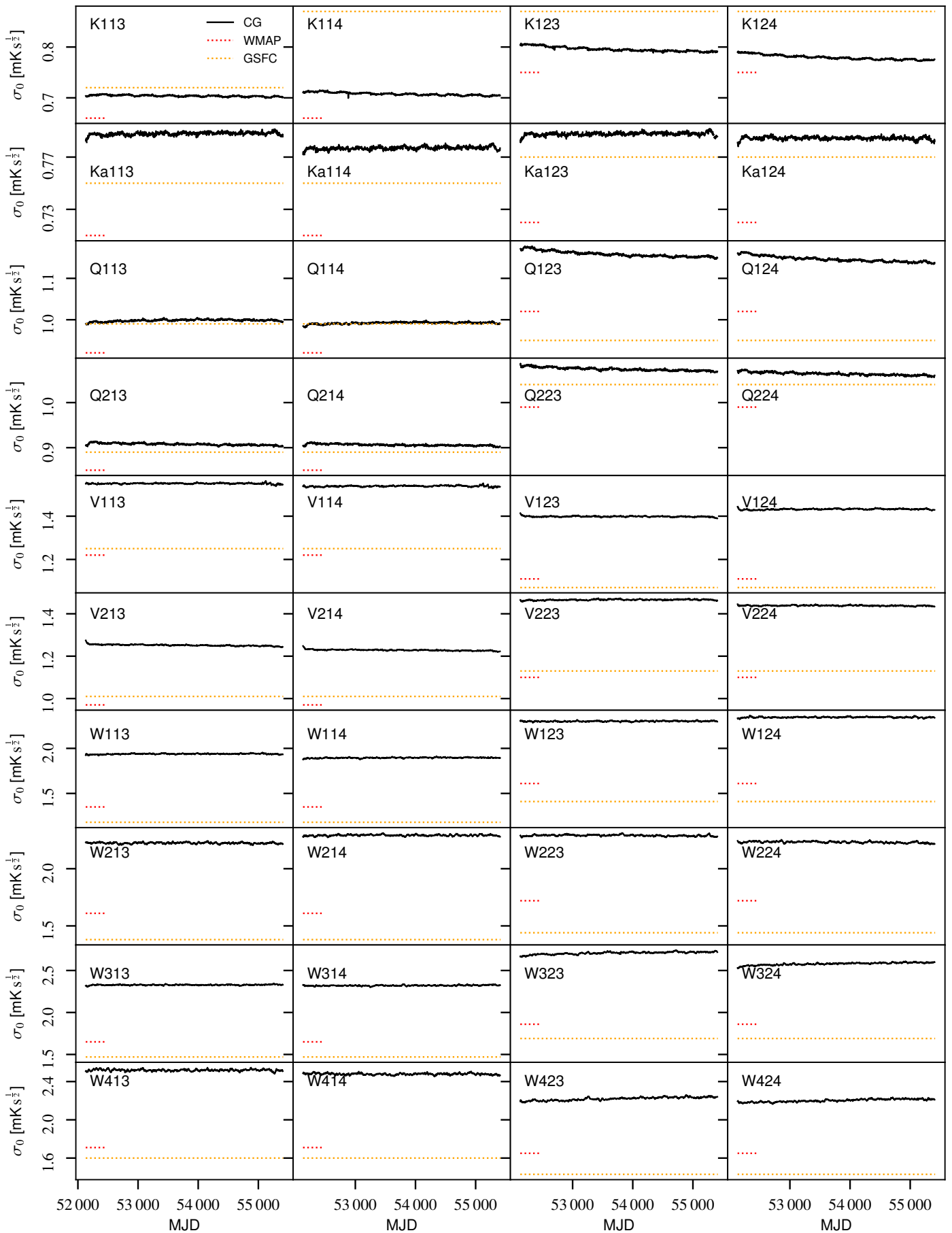
Appendix B: WMAP frequency map survey

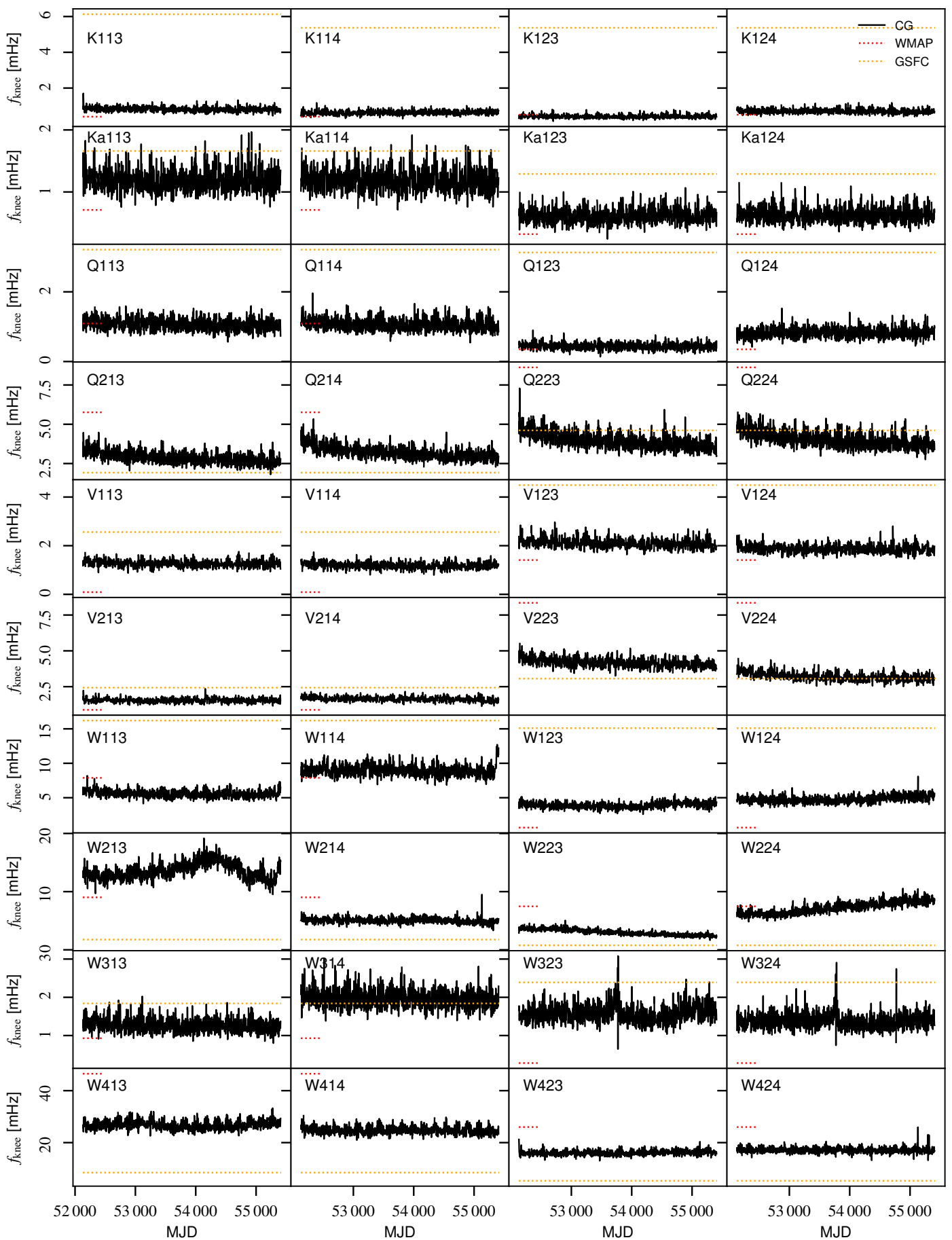
Appendix C: Comparison with BEYONDPLANCK LFI results

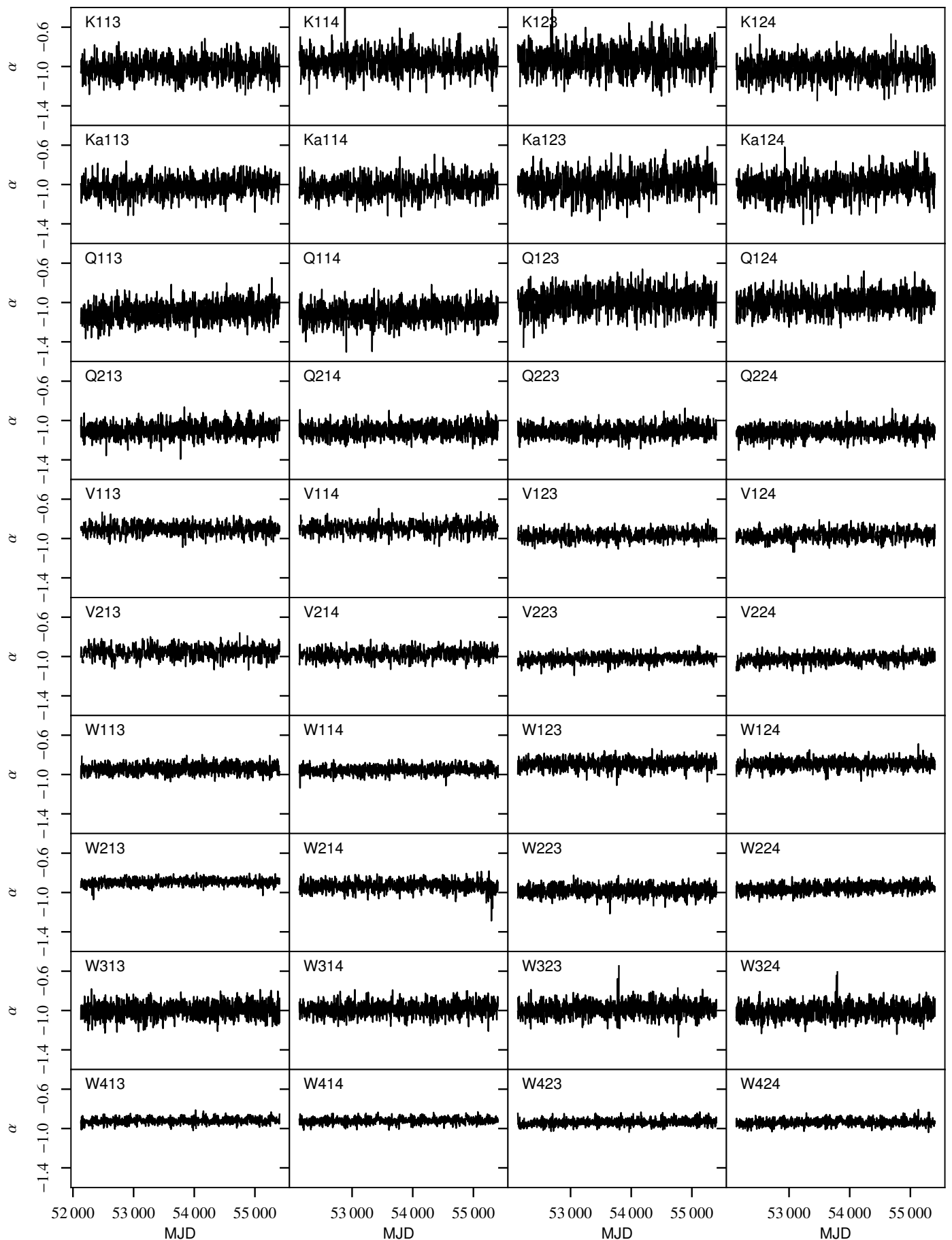
**Fig. A.1.** baseline.

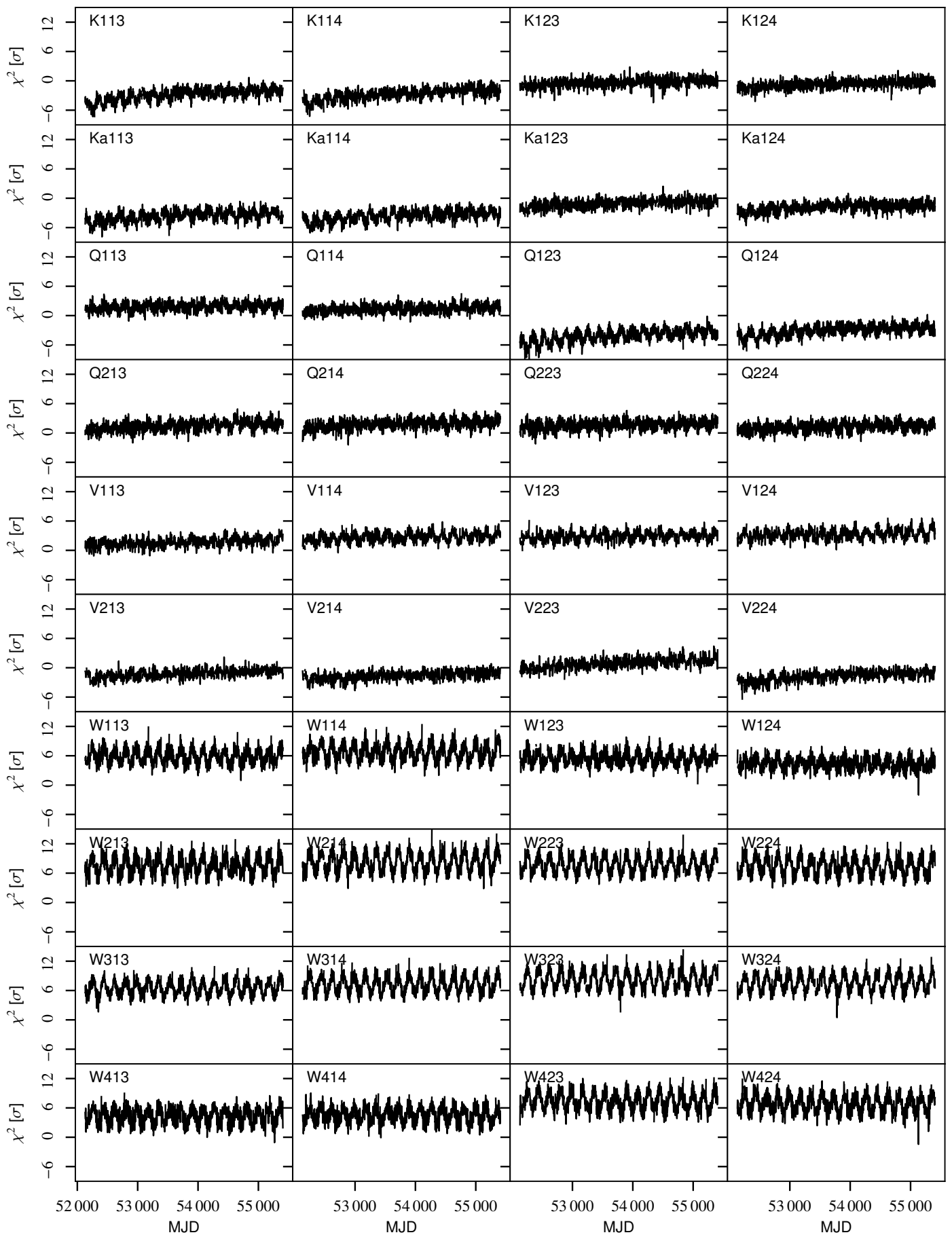
**Fig. A.2.** baseline slopes.

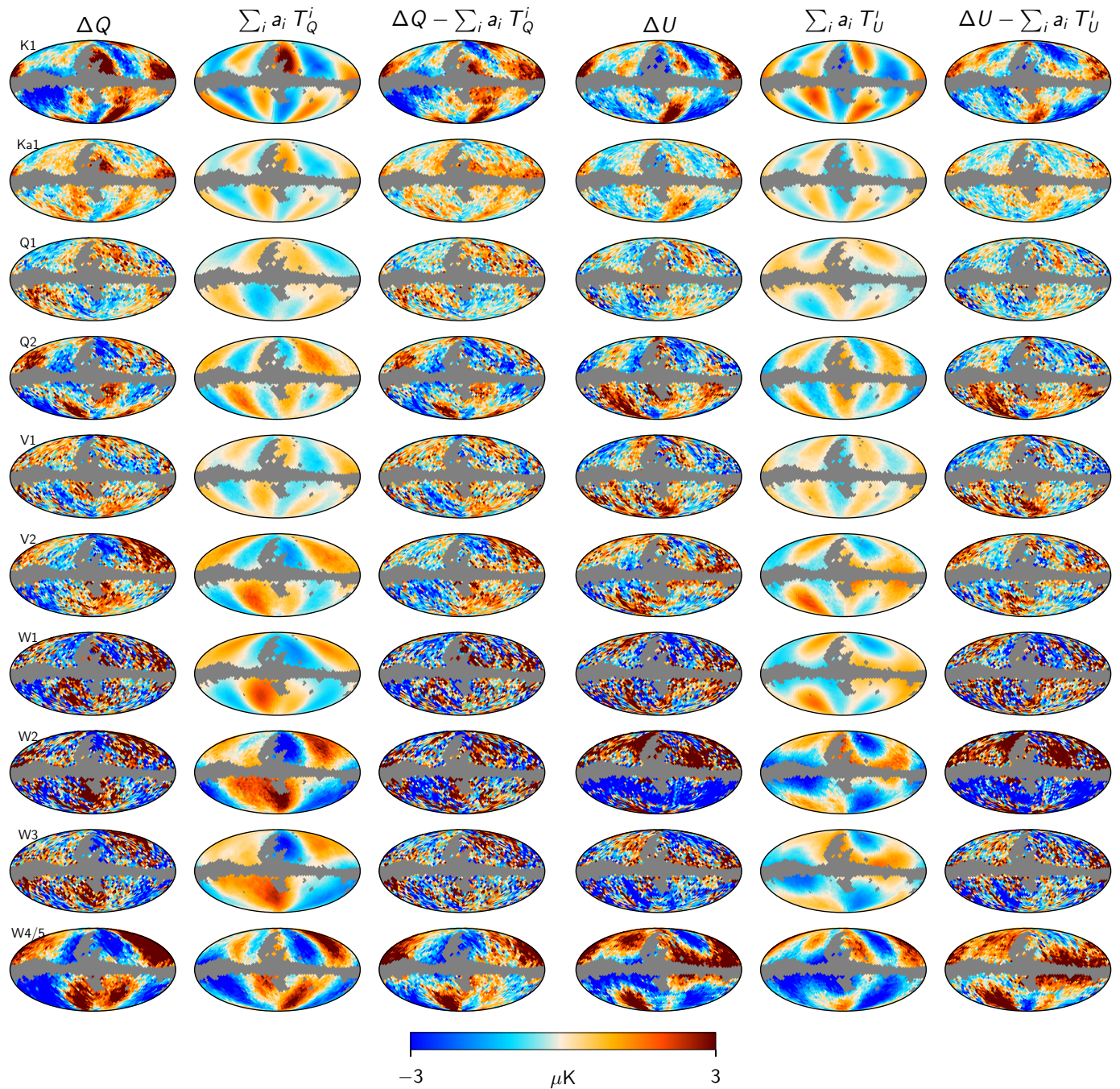
**Fig. A.3.** Gain.

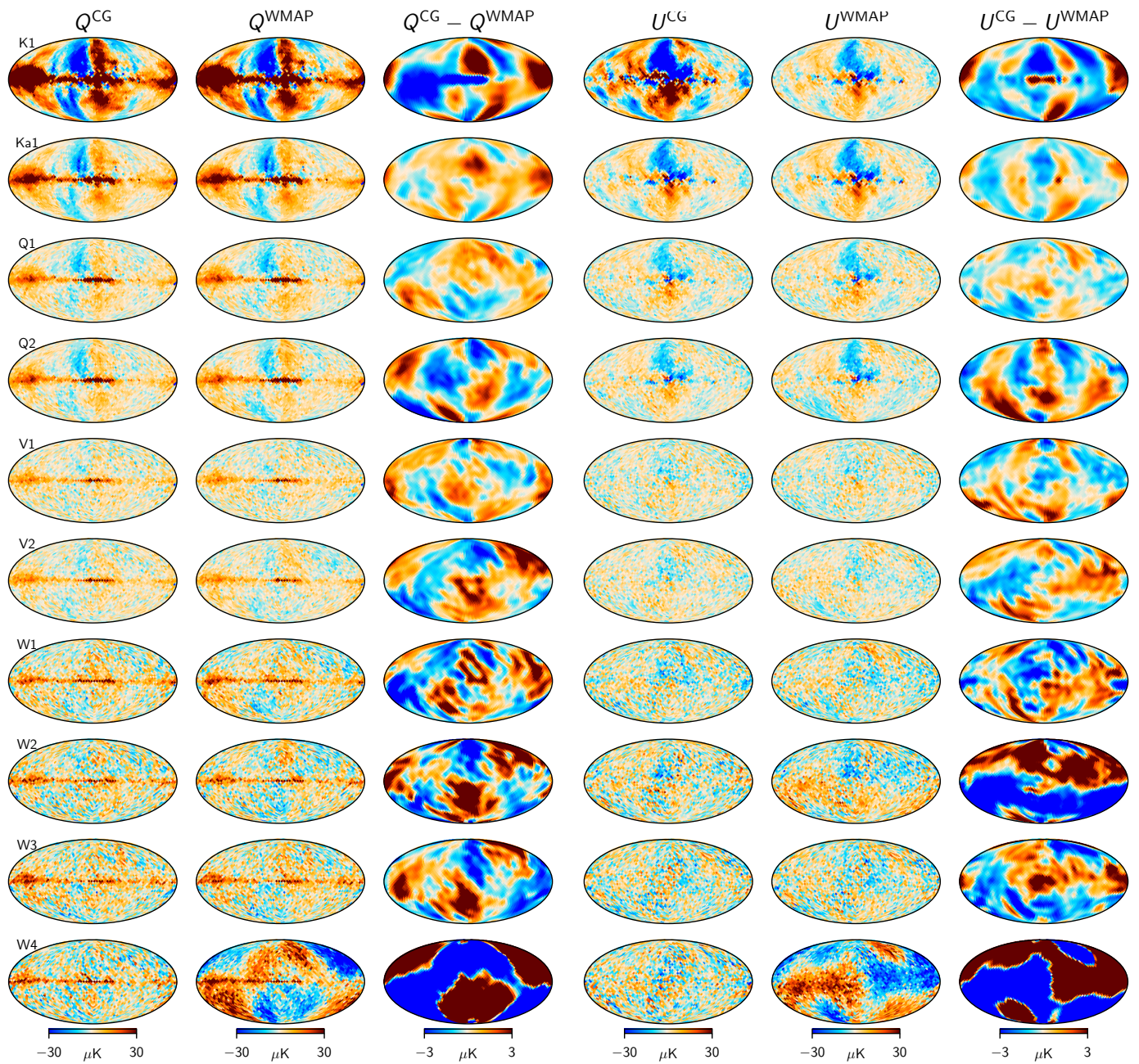
**Fig. A.4.** σ_0 .

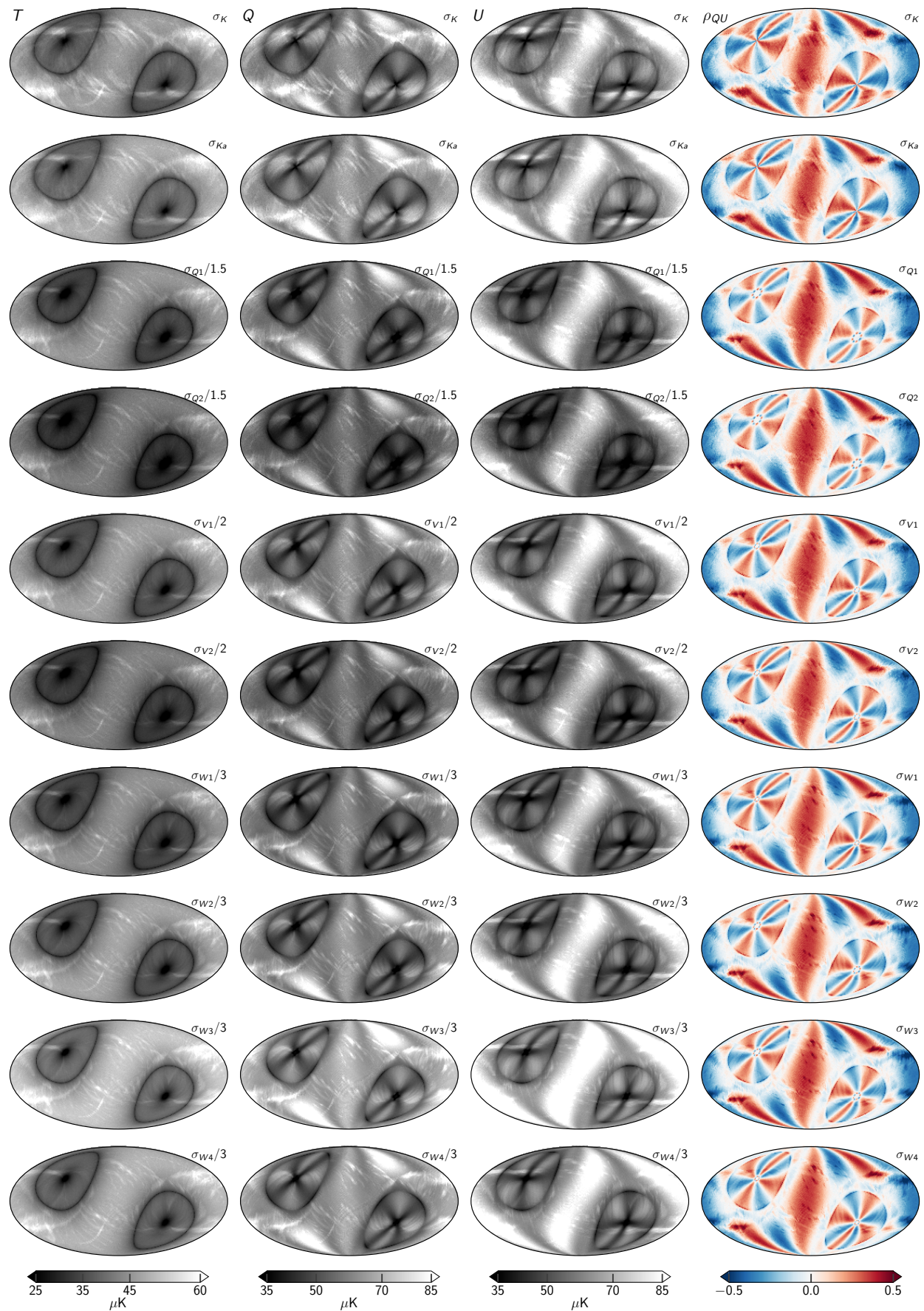
**Fig. A.5.** Fknee.

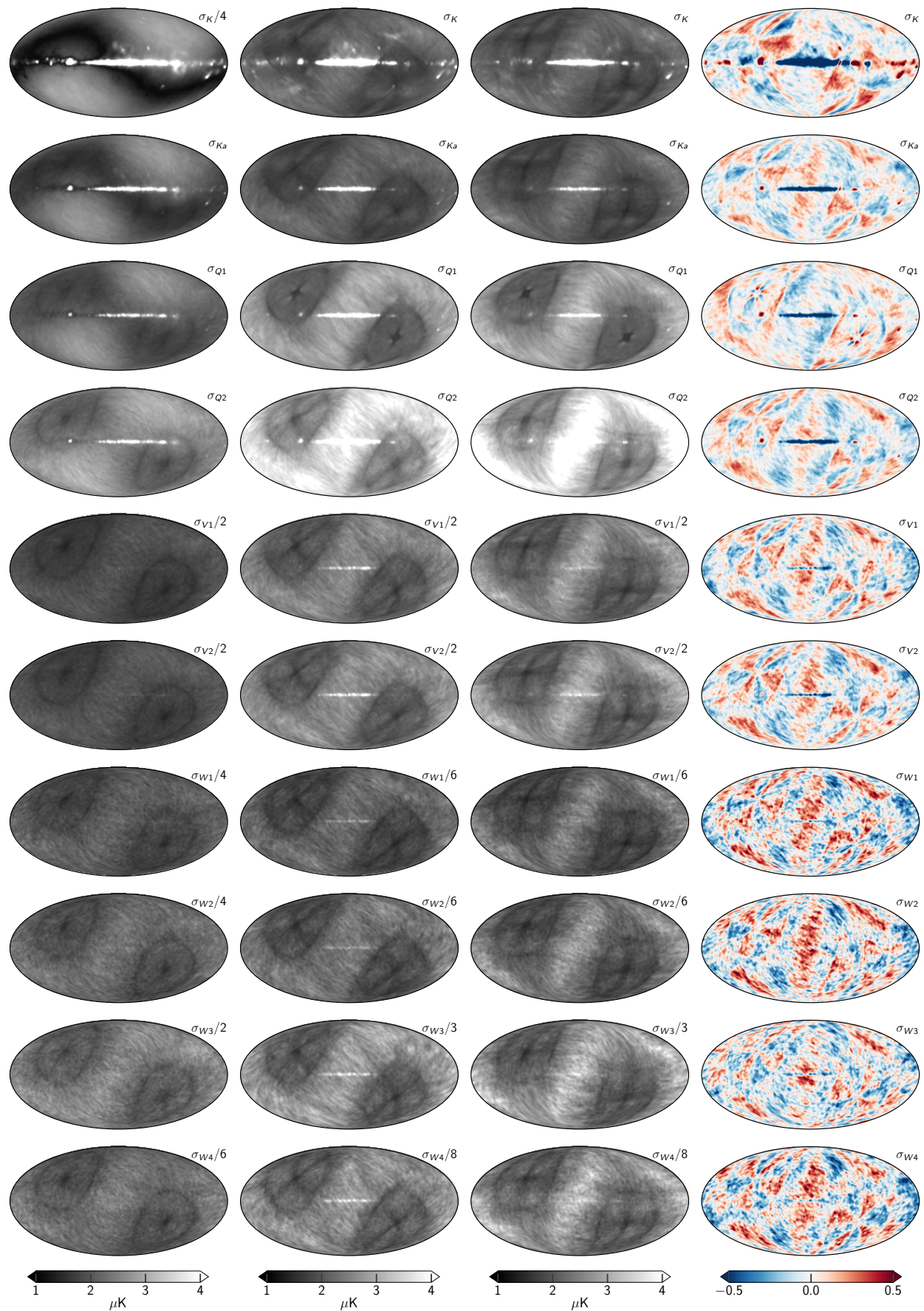
**Fig. A.6.** alpha.

**Fig. A.7.** chisq.

**Fig. A.8.** Transmission imbalance templates

**Fig. B.1.** Sky maps

**Fig. B.2.** RMS maps

**Fig. B.3.** STD std

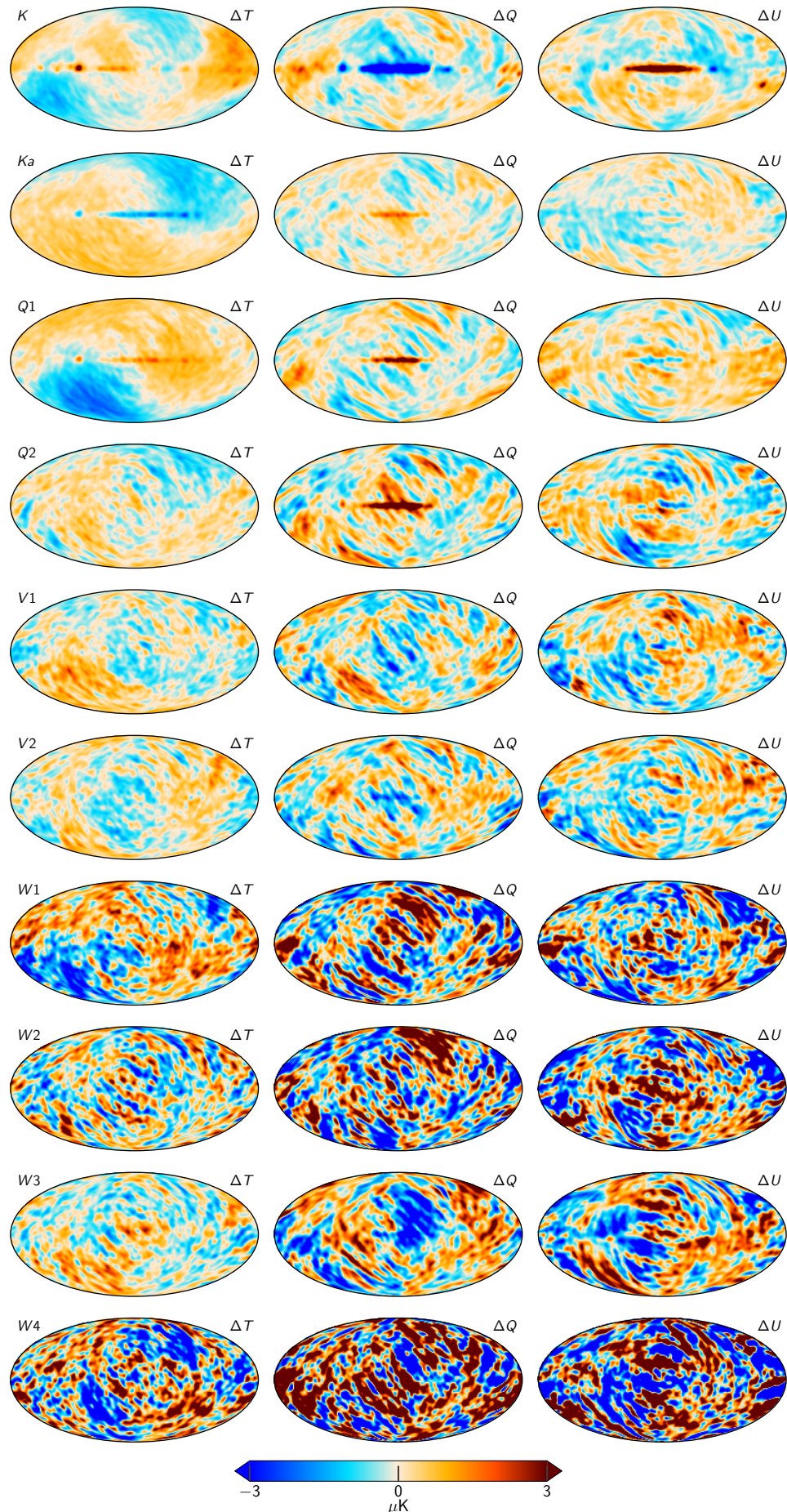
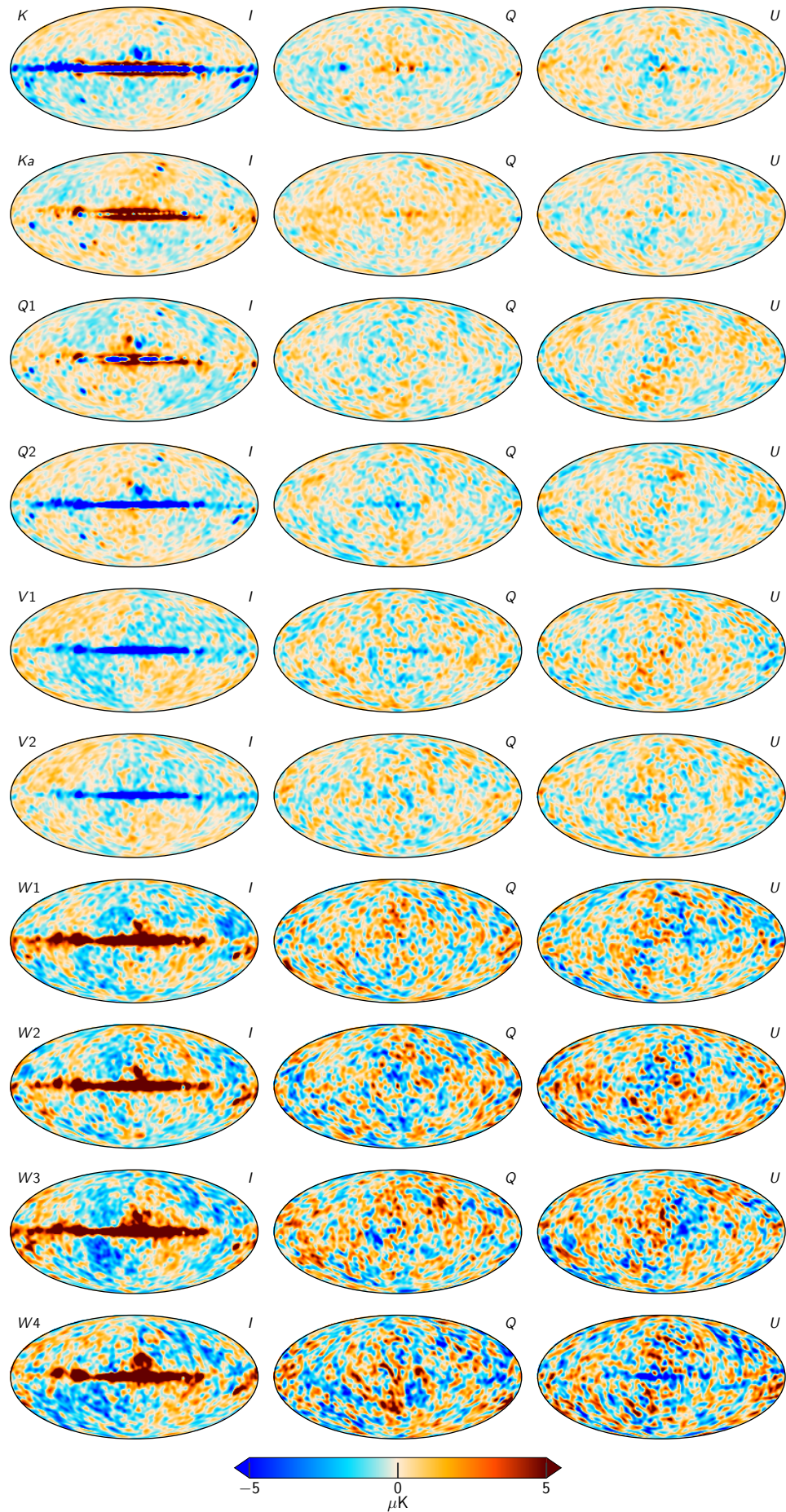


Fig. B.4. Differences between two samples
Article number, page 50 of 51

**Fig. B.5.** TOD Residuals for each of the WMAP channels, smoothed by 5° .